
UNIVERSITY OF OXFORD

DEPARTMENT OF PHYSICS

Quasi Phase Matching Techniques For High Harmonic Generation

Matthew Joseph Landreman

Saint John's College, Oxford

Thesis Submitted for the Degree of Master of Science by Research

26th September 2006

Quasi Phase Matching Techniques For High Harmonic Generation

Matthew Joseph Landreman

Saint John's College, Oxford

Thesis Submitted for the Degree of Master of Science by Research

26th September 2006

Abstract

This thesis examines the possibility of quasi phase matching (QPM) for high harmonic generation in gases. In the primary scheme considered, a counter-propagating laser beam (CPB) suppresses harmonic generation in controlled regions.

With hollow capillary targets, high harmonic light was masked by bright line radiation, created from CPB light which hit the capillary wall. No effect of the CPB was seen with these targets. The use of very long (~ 10 cm) capillaries was attempted to spatially filter the driving beam, but fractional transmission was prohibitively low, likely a result of the method for machining the capillaries.

With gas cell targets the CPB was effective at extinguishing harmonic generation in controlled locations, and a factor of ~ 2 enhancement was observed. Greater enhancement was likely not seen due to a low number of dephasing lengths within the region of harmonic generation. For sufficient driver energy, harmonics were generated in three distinct regions. Several techniques are suggested for inferring the ionisation fraction and dephasing length from scans of the timing delay between the CPB and driving beam.

Extinction was produced with both a CPB polarised parallel to and perpendicular to the driving beam. Experiments showed good agreement with certain models of the CPB energy required for each scheme, but agreement was poor for predictions based on intensity-dependent phase.

This thesis also examines a second method of QPM in which beating between capillary modes creates an intensity modulation. It is found that this scheme is complicated by sensitivity to the transverse spatial profile of the input light. The results have implications for the many reports of high harmonic generation in capillaries, for the intensity fluctuations due to mode beating are likely to be present in any such experiment.

Contents

Contents	i
Acknowledgements	iv
1 Introduction	1
1.1 The need for a bright coherent XUV/SXR source	1
1.2 Scope of this thesis	4
1.3 Role of the author	5
2 Laser-matter interactions	6
2.1 High harmonic generation	6
2.1.1 Intensity-dependent phase	10
2.2 Ionisation	11
2.3 Defocusing	13
2.4 Blueshifting	14
2.4.1 Ionisation blueshifting	14
2.4.2 Nonadiabatic blueshifting	17
2.4.3 Harmonic peak splitting	18
3 Grazing-incidence waveguides	20
3.1 Modes of the step-index waveguide	20
3.2 Coupling into a capillary	23
3.3 Mode beating	24
3.4 Previous experiments	26
4 Phase matching of harmonics	28
4.1 Harmonic wave growth	28
4.2 Nonuniform dispersion	31
4.3 Sources of dispersion	33
4.4 Phase matching of high harmonics: Previous work	37
4.5 Limits to phase matching	38
4.6 Harmonic peak splitting revisited	39
4.7 Quasi phase matching	41
4.8 QPM of high harmonics: Previous work	43
5 Theory of Quasi Phase Matching with Counter-Propagating Light	45
5.1 HHG suppression	45
5.1.1 Parallel polarisations	45
5.1.2 Previous experiments	48

5.1.3	Perpendicular polarisations	49
5.2	Methods for creating pulse trains	54
5.2.1	1-crystal method	54
5.2.2	N-crystal method	57
6	Experimental systems	58
6.1	Laser machining	58
6.2	Mounting of capillaries	58
6.3	Astra laser	60
6.4	Oxford terawatt laboratory	64
6.4.1	Original configuration	64
6.4.2	Modifications	64
6.4.3	Spectrograph calibration	68
7	Measurements of Pulse Trains	72
7.1	Auto-correlation versus cross-correlation	72
7.2	Satellite fringes	77
7.3	Pulse train gallery	79
7.4	Sensitivity to crystal alignment	80
7.5	Summary of findings	81
8	Astra experiments	83
8.1	Alignment sensitivity	83
8.2	Energy scans	84
8.3	Dependence on timing	86
8.4	Discussion	87
8.5	Low- q enhancement	88
8.6	High- q enhancement	91
8.6.1	Mode beating	92
8.7	Summary of findings	95
9	Oxford experiments	97
9.1	Harmonic generation in capillaries	97
9.1.1	Capillary design	97
9.1.2	Guiding	100
9.1.3	Harmonic spectra from capillaries	102
9.1.4	Estimation of dephasing length	102
9.2	Harmonic Generation in gas cells	106
9.2.1	Parameter scans	107
9.2.2	Selecting a QPM parameter regime	108
9.2.3	Energy dependence	112
9.2.4	Experimental comparison of extinction by parallel and perpendicular polarised light	113
9.2.5	Analysis of extinction and enhancement regions	116
9.2.6	Determination of intensity and ionisation from blueshift	122
9.2.7	Studies of enhancement phenomenon	123
9.2.8	Dependence on focus position	124
9.2.9	Dependence on pulse compression	128
9.2.10	Peak broadening and splitting	129

9.2.11	Trains of distinct pulses	132
9.2.12	Summary of findings	133
10	Conclusions and Future Directions	135
10.1	Summary of experiments	135
10.2	Future directions	137
10.2.1	QPM by selective capillary mode excitation	137
10.2.2	Waveguide improvements	138
10.2.3	Other issues	139
	Bibliography	141

Acknowledgements

Through the work described in this thesis, two fine physicists have taught me a great deal about how to manage a large enterprise and how to think with greater quantitative rigour. Simon Hooker has been always reasonable, always available with an insightful and kind suggestion, and always available when help was needed. Matt Zepf's energy, wide experience, and imagination were key in initiating the project, executing it, and trying to make sense of the results. Both deserve particular thanks for their help in editing this thesis. Additional support from Justin Wark and Keith Burnett is also gratefully acknowledged. Additionally, this thesis owes much to Brendan Dromey's long hours at Astra and tireless crunching of the numbers afterwards. Tom Robinson and Kevin O'Keeffe were indispensable co-pilots during the Oxford experiments. The rest of the Hooker Group – Dave Spence, Claire McKenna, Tony Gonsalves, Nic David, Tom Rowlands-Rees, and Clive Woolley – have been capable colleagues and peerless teatime companions. The Ewart group deserve special thanks for all the equipment and advice they have lent during the project. The Astra experiment would have been impossible without much assistance from the staff at the Rutherford Appleton Laboratory. And finally, thanks are owed to the other staff and students at Oxford Physics, all of whom have made the Clarendon a very warm place to work these past years.

M.J.L., Oxford, August 2006

CHAPTER 1

Introduction

1.1 The need for a bright coherent XUV/SXR source

When the first lasers were constructed in the 1960s, the eventual uses of these devices could hardly have been foreseen: reshaping corneas, sending data through optical fibres, gauging environmental toxins in the smoke from factories, and innumerable other applications. A great fraction of our knowledge in chemistry, biology, and physics has been obtained with experiments that make use of coherent light. However, it is hard to obtain lasing at frequencies above the near-ultraviolet, leaving the potential of several intervals of the EM spectrum untapped. A bright coherent x-ray source, if developed, could allow new nanoscale manufacturing techniques and *in vivo* observations of sub-cellular structures in three dimensions [1, 2]. Numerous applications in atomic physics may also be possible.

Achieving lasing at x-ray frequencies is difficult because the necessary population inversions are much harder to achieve, as they are depleted by spontaneous emission, which scales (for a given oscillator strength) as the *square* of the laser frequency. Furthermore, it is hard to find suitable materials for use as cavity mirrors at XUV or x-ray frequencies. Consequently, great effort is being expended to find another method to produce coherent XUV and x-ray light of high spectral brightness.

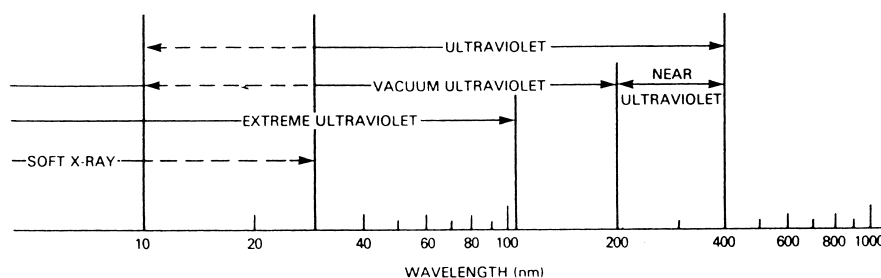


FIGURE 1.1: The spectrum beyond violet. Figure from [3].

Several schemes for coherent x-ray generation are under consideration. Unfortunately, none can match the convenience and flexibility of the visible wavelength laser. Figure 1.2 compares some of the options. X-rays can be produced with relatively little apparatus or cost by running an electron beam into a metal target, or by focusing a laser onto a solid [1, 2]. These sources are of quite limited spectral brightness ($< 10^{13}$ photons sec^{-1} mrad^{-2} mm^{-2} per 0.1% bandwidth). Synchrotron sources are much brighter, especially those that employ undulators. Most recently, free electron lasers have been developed that create very coherent radiation using stimulated emission from the electrons in a synchrotron [4, 5]. However, all of these synchrotron-based sources are extremely expensive; experiments must be conducted in huge user facilities that cost hundreds of millions of pounds.

Lasing can be achieved at XUV/SXR wavelengths, albeit with very low efficiency compared to visible-wavelength lasers. A plasma is used as the gain medium, and no cavity is used, since highly reflective materials are unavailable [6, 7]. These “x-ray lasers” can provide reasonable x-ray brightness at much reduced space and cost compared to synchrotron sources.

Yet another scheme for generating bright coherent x-rays, the one which the rest of this thesis will examine, is the generation of harmonics from a longer-wavelength laser. Harmonics can be generated when intense light passes through matter, and it is common to obtain the second or third harmonic using a crystal as the medium; many commercial lasers are doubled with crystals such as potassium dihydrogen phosphate (KDP). With gas as the target, harmonic orders well into the hundreds have been produced. Using this high harmonic generation (HHG) technique, x-rays have been produced at a spectral brightness competitive with some undulator sources [8]. HHG has also already been used as a photon source for other scientific applications [9].

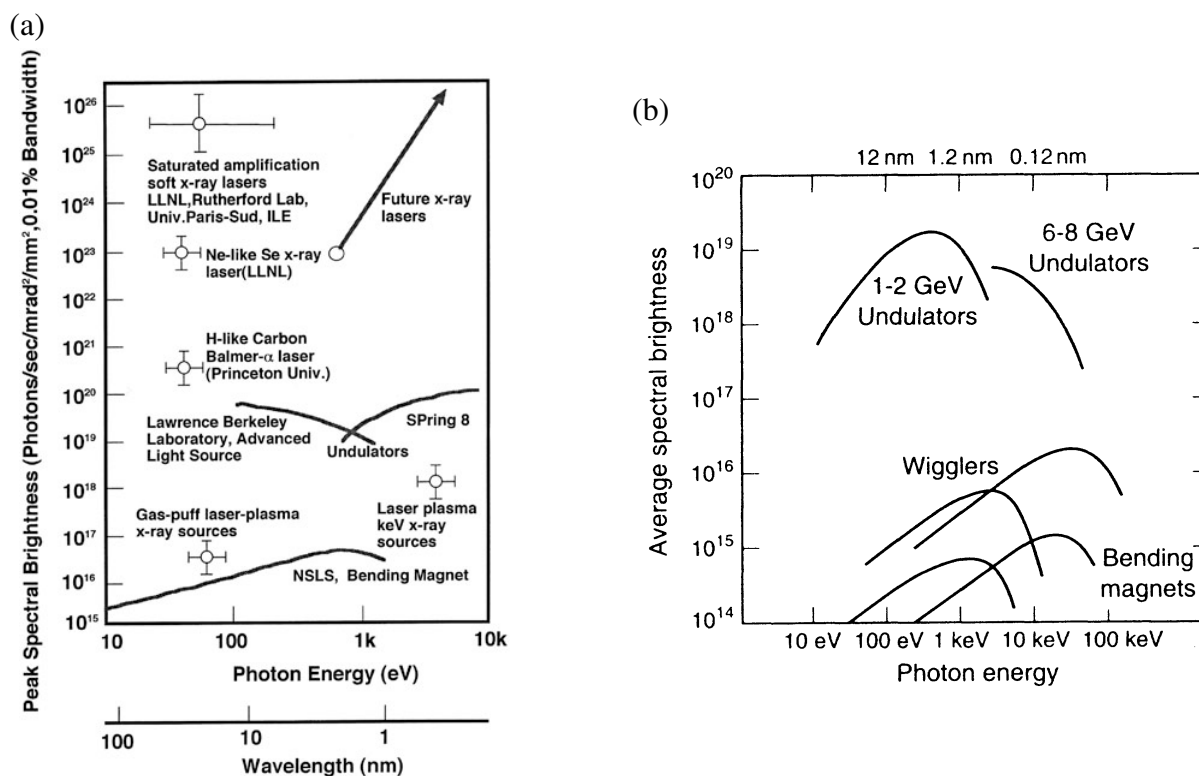


FIGURE 1.2: Two authors' comparisons of spectral brightness (sometimes called spectral brilliance) between different X-ray sources. For comparison, the largest reported peak spectral brightness in the water window (2-5 nm) from a high-harmonic source is 10^{20} in the units of (a) [8]. The vertical axis in (b) is in units of photons $\text{sec}^{-1} \text{mrad}^{-2} \text{mm}^{-2}$ per 0.1% bandwidth. Figures taken from [6] and [1].

A hurdle in any sort of nonlinear wave generation, and the principal barrier to achieving higher intensities of XUV and SXR light with harmonic generation, is a result of the different phase velocities between the fundamental and harmonic radiation. Ionisation is an unavoidable companion of harmonic generation, and the free electrons which are produced result in a large dispersion. The fundamental light creates a wave of polarisation in the atoms, and the phase fronts of this polarisation wave necessarily move at the phase speed of the driving light. The XUV radiated by this polarisation wave however moves at a different phase speed. The XUV radiated from one location, after it travels a certain *dephasing length*, will be π out of phase with the radiation from the new location. Destructive interference occurs between harmonics generated at different points in the medium, limiting the growth of the XUV wave. It turns out that the harmonic intensity is limited by a factor Δk^{-2} , where $\Delta k = k(q\omega) - qk(\omega)$ describes the degree of phase velocity mismatch between the fundamental frequency ω and the q -th harmonic. When generating second or third harmonics in crystals, the birefringence of the crystal can

be used to achieve “phase matching,” $\Delta k = 0$. To do so, the phase velocity of the driver in one polarisation state is matched to the phase velocity of the harmonic wave in the orthogonal polarisation state. However, for higher-order harmonics, gases rather than crystals must be used as the nonlinear medium; solids absorb strongly beyond 100 nm, and they would be damaged by the high laser intensities required. Phase matching by birefringence is therefore not an option. For harmonics of moderate order, those made with less than 2-5% ionisation of the target medium, phase matching may be possible by balancing several sources of dispersion. For the highest order harmonics, however, the high level of ionisation precludes these schemes as well.

Another way to circumvent the velocity mismatch is known as “quasi phase matching” (QPM). In QPM, the phase velocities remain unequal, but the interaction region is patterned in a way such that only constructive interference occurs. Harmonic generation is suppressed in a periodic set of zones, those zones which otherwise would contribute negatively rather than positively to the final harmonic wave.

1.2 Scope of this thesis

The chapters that follow report on experiments to enhance the efficiency of high harmonic generation using quasi-phase matching. The experiments were carried out in two campaigns, the first at the Astra laser at the Rutherford Appleton Laboratory during January - March 2005, and the second at the University of Oxford’s Clarendon Laboratory from January - April 2006. In the chapter that follows this Introduction, the laser-matter interactions which are relevant for these experiments are discussed. Much of the experimental work involved grazing-incidence waveguides, so Chapter 3 explored the theoretical background to this technique. Chapter 4 presents the theory of phase matching and quasi-phase matching in more detail, and also discusses previous experiments related to QPM of HHG. The principal QPM scheme considered in this thesis involves the use of a counter-propagating train of pulses, so Chapter 5 discusses methods for producing such pulse trains. The interaction between counter-propagating light and the primary “driver” beam will be discussed here as well. Chapter 6 describes the experimental

layout at RAL and Oxford, and observations of pulse trains from the two laboratories are presented in Chapter 7. Chapters 8 and 9 describe the other HHG results from the two experiments. Finally, in Chapter 10, the prospects of these QPM schemes are evaluated and future directions for research are discussed.

1.3 Role of the author

The Astra experiment was conducted as part of a team with Brendan Dromey and Matt Zepf, both of Queen's University Belfast, and Simon Hooker. Astra staff assisted with laser operation and other infrastructure. Dr. Zepf and the Astra staff were largely responsible for planning of the optical layout, with construction mostly executed by Mr. Dromey and the author. In preparation for this experiment, earlier tests of pulse train creation and diagnosis were conducted by the author at Oxford, with some assistance from Mr. Dromey. The assistance of Mr. Dromey and Dr. Zepf was also key in analysis of data from the experiment, discussed in Chapter 8.

The modifications to the Oxford laser system, discussed in Chapter 6, were designed by the author. Kevin O'Keeffe, Tom Robinson, and Dr. Hooker assisted with construction and operation of the experiments there. The author was also responsible for all analysis of Oxford data presented in this thesis.

Other activities of the author outside of these experiments included the design of glass capillary mounting hardware, modification of the Oxford laser-machining system for grazing-incidence capillaries, automation of gas pressure control, and support for experiments by other group members.

CHAPTER 2

Laser-matter interactions

A large variety of physical processes can occur when intense lasers interact with matter. Here, a review is given of those that are most relevant for the parameter regime of the experiments discussed later.

2.1 High harmonic generation

Harmonics can be generated from strongly driven atoms because each atom acts as a nonlinear oscillator. Classical driven oscillations in any symmetric non-quadratic potential will typically have Fourier components at odd multiples of the fundamental frequency[10], as figure 2.1 shows. Atoms near the focus of a high-power laser experience a quantum-mechanical version of this situation, as the laser electric field is sufficient to drive bound electrons well beyond the perturbative regime. Each atom in the laser field therefore has a dipole moment with frequency components at the odd harmonics. Together these dipoles create an oscillating polarisation density, which acts as a source term in Maxwell's equations and generates electromagnetic wave components at the odd harmonic frequencies. To create harmonics of even order, the electron potential must lack inversion symmetry; hence, even-order harmonic generation is possible in certain crystals but not in monoatomic gases.

Typical HHG spectra look much like the classical spectrum of figure 2.1. There is a large peak at the fundamental, and the next few harmonics are of progressively decreasing magnitude.

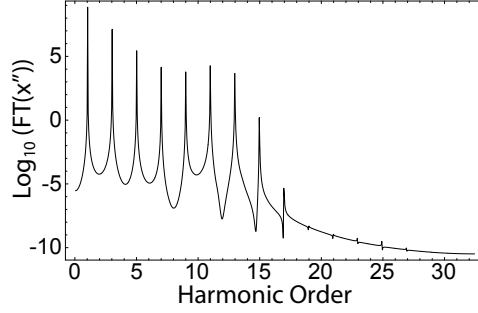


FIGURE 2.1: The acceleration spectrum $\text{FT}(x''(t))$ for a classical damped and driven oscillator ($x''(t) = -\Gamma x'(t) + F \cos \omega t + \frac{dV}{dx}$) oscillating in a potential $V(x) = \frac{\omega_0^2}{2}x^2 + \beta x^4$ with $\omega = 2.5$, $\omega_0 = 25$, $\Gamma = 1$, $\beta = 75$, and $F = 500$.

Then, there is relatively little decrease in energy over the next harmonic orders. This energy band is referred to as the “plateau.” Finally, there are no harmonics at all above a certain *cutoff frequency*.

The existence and location of the cutoff frequency are explained well by an oft-cited quasi-classical model [11, 12]. In this model, one can think of HHG as occurring through the following three steps:

- An atomic electron is in its unperturbed state until some point in the laser pulse, when the atom is ionised.
- The electron, now a free particle in the continuum, follows a classical trajectory determined by the sinusoidal electric force of the laser field.
- Harmonics are generated if the electron returns to the nucleus and recombines. The kinetic energy gained while in the continuum, as well as the ionisation energy, are converted into radiation.

Figure 2.2 shows some of the possible classical electron trajectories. It should be noted that the electron may return to the location of the parent ion any number of times. The greatest possible kinetic energy at the time of recombination works out to $3.17U_p$, where U_p is known as the “ponderomotive energy”:

$$U_p = \frac{e^2 E^2}{4m_e \omega^2} \quad (2.1)$$

ω is the angular frequency of the driving laser, and E is the peak electric field. Thus, the cutoff

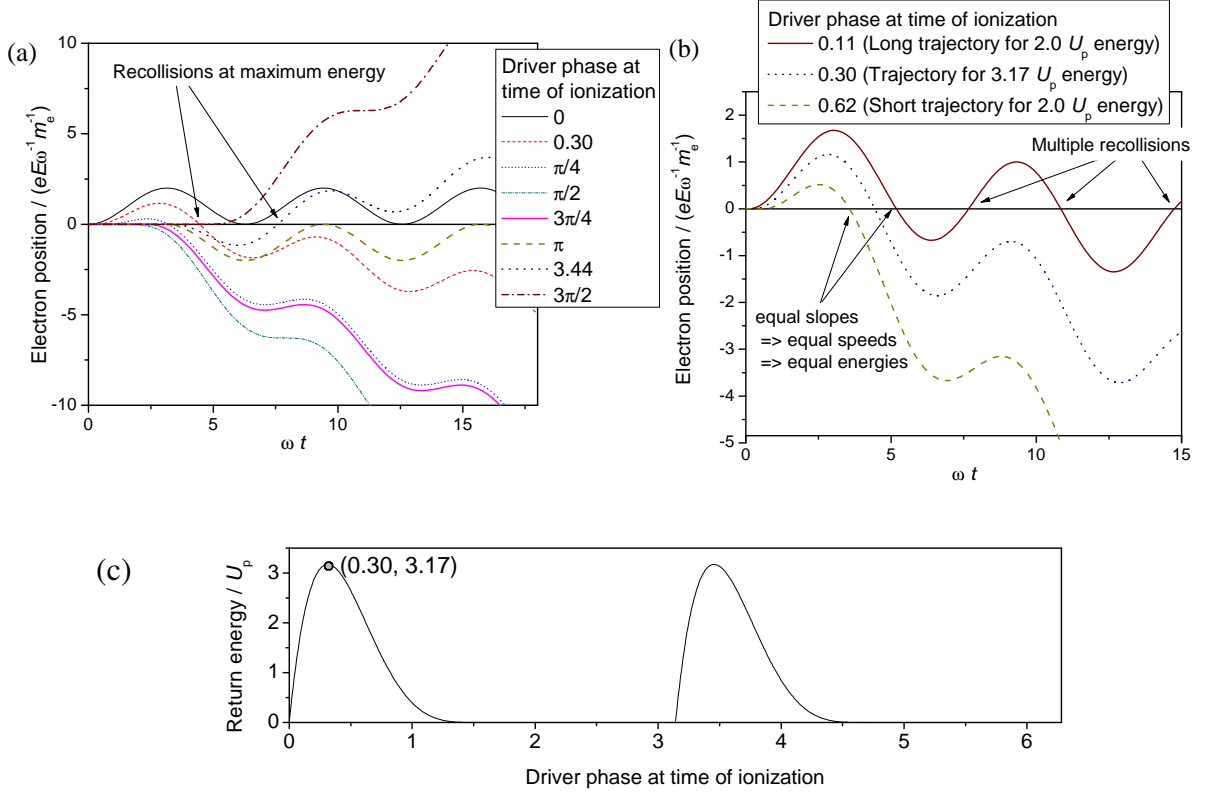


FIGURE 2.2: (a-b) Quasi-classical electron trajectories, and the kinetic energy at the time of the electron's first return to the parent ion (c). (b) At return energies less than the maximum possible $3.17 U_p$, two trajectories are possible that give rise to that energy. Note in (b) that multiple returns to the ion are possible for some trajectories. (b) is adapted from [13].

frequency corresponds to an energy of:

$$U_{\text{cutoff}} = U_i + 3.17U_p \quad (2.2)$$

where U_i is the ionisation energy of the atoms. The cutoffs in experimental spectra show reasonable agreement with this theoretical value [14]. For harmonics of energy $U < U_{\text{cutoff}}$, there will be two trajectories (“long” and “short”) that give rise to the proper energy $U - U_i$ on the first return to the atom. There are other trajectories which bring the electron back to the parent ion with the proper energy on later passes.

HHG can be treated more rigorously by considering the time-dependent Schrodinger equation for the dynamics of an atom in the laser field. By calculating \ddot{p} for the electron wavefunction, where $p = ex$ is the dipole moment, one can compute the contribution to the overall

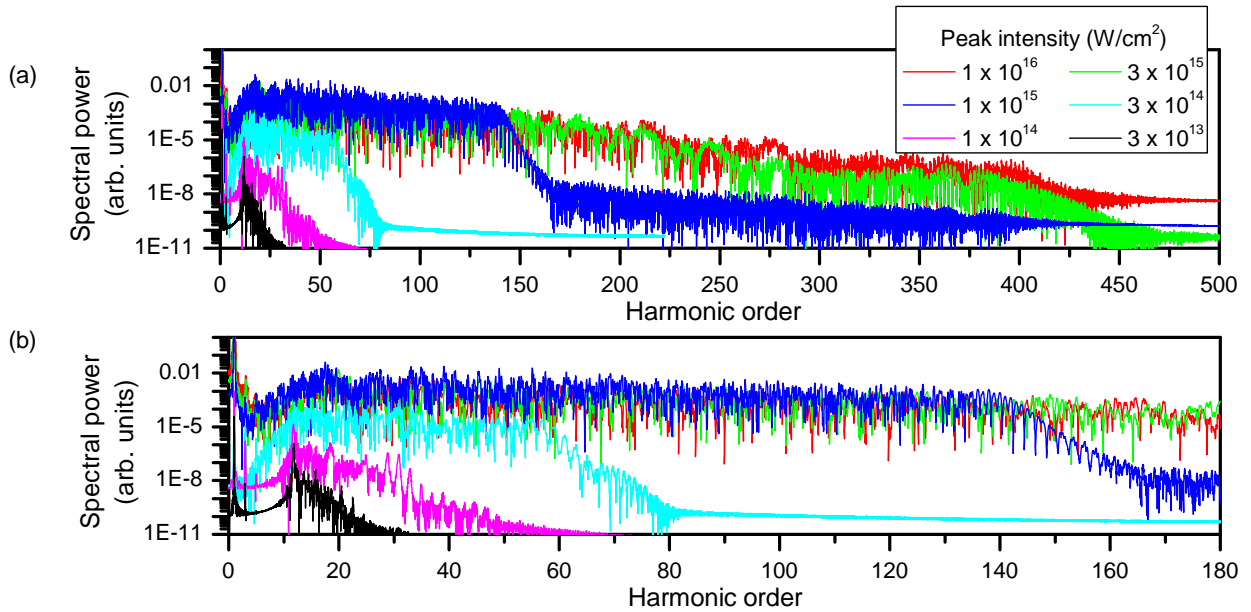


FIGURE 2.3: Single-atom HHG spectra for various driving intensities are computed by numerically integrating the Schrodinger equation for 1D helium[15]. A 30 fs, 800 nm Gaussian pulse is used. The cutoff energy does not change significantly between the highest two plotted intensities because ionisation depletes the atoms before the pulse peak. (b) is the same as (a) but plotted over a different horizontal range.

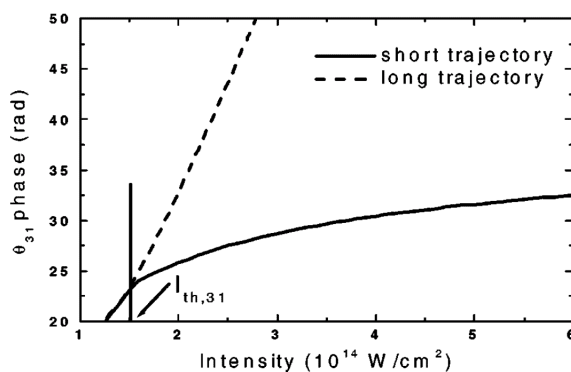


FIGURE 2.4: Phase of harmonic emission for the two shortest semi-classical trajectories that lead to the $q = 31$ harmonic in Ar. The calculation, based on an analytical quantum mechanical treatment of HHG, is for a 30 fs driving pulse. Note the stronger dependence on intensity for the longer trajectory. Figure taken from [16], in which the opposite sign convention for phase is used (i.e., quantities vary as $e^{+i\omega t}$).

harmonic radiation from a single atom. Both numerical and analytical quantum treatments have been useful for understanding HHG.

Numerical simulation of the Schrodinger equation has also been extensively used to calculate single-atom high-harmonic spectra; see e.g. [17–22]. Figure 2.3 shows typical single-atom spectra, simulated by the author [15]. The peaks in the plateau are highly structured, so much so that they merge with adjacent peaks. The spectra recorded from an HHG experiment may look quite different from single-atom spectra, and typically exhibit much less structure. These points will be discussed further in section 2.4.2.

2.1.1 Intensity-dependent phase

Analytical methods [23, 24] help explain the success of the quasi-classical model, as the fully quantum mechanical treatments result in expressions that effectively sum over the possible quasi-classical electron trajectories. One key quantity which can be computed with analytical quantum treatments – but not with the quasi-classical model – is the phase of the harmonic emission relative to the driving electric field. For an atom in a driving electric field $\text{Re}(E_0 e^{-i\omega t})$, the q -th harmonic component of the atom's induced dipole moment will be

$$p(I, t) = \text{Re} \left\{ \sqrt{f_q(I)} E_0 e^{i[\phi_q(I) - q\omega t]} \right\} \quad (2.3)$$

where $I = c \epsilon_0 |E_0|^2 / 2$ is the driving intensity, $f_q(I) \in \mathbb{R}$ is proportional to the intensity-dependent efficiency, and $\phi_q(I)$ is the intensity-dependent phase. Strong experimental evidence for a significant intensity dependence to ϕ_q has been observed [25, 26].

In the analytical treatments of HHG, the total atomic dipole moment turns out to be a sum of terms corresponding to the various quasi-classical trajectories. The phase for each term is approximately an affine (i.e., linear plus offset) function of intensity. The slope of this function is given by

$$\frac{\partial \phi_q}{\partial I} = -\frac{K e^2}{2 \epsilon_0 c m_e \hbar \omega^3} \quad (2.4)$$

where the dimensionless constant K differs for each trajectory [26–30]. K is roughly $1/\omega$ times the time between ionisation and recombination; e.g., about 2π for the long trajectory. The phase

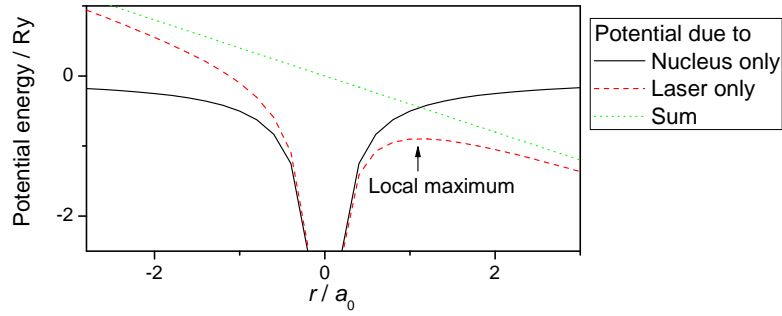


FIGURE 2.5: Distortion of the potential seen by a bound electron due to an intense laser field.

is thus more sensitive to intensity for longer trajectories than for short ones. A typical $\phi_q(I)$ is shown in figure 2.4.

Note that ϕ_q is independent of the harmonic order. Also, note that the sign of equation 2.4 would be reversed if we had chosen the alternate convention for time variation, in which quantities varied as $e^{+i\omega t}$ rather than $e^{-i\omega t}$.

The phase of the *total* dipole moment from each atom (the sum of the components for each trajectory) is almost exactly that of the *second-shortest* trajectory. In general, longer trajectories contribute less to the total due to quantum diffusion – spreading of the electron wave packet once it is no longer bound – which reduces the probability of recombination. However, the shortest trajectory does not dominate because it results from ionisation when the laser electric field is nearly at its minimum. The second-shortest trajectory instead results from ionisation near the field maximum, when ionisation is much more rapid. Thus, harmonics are most likely to originate from the second-shortest trajectory [29]. The overall phase of harmonic emission therefore varies with intensity approximately according to 2.4 with $K \approx K_{\text{long}} \approx 2\pi$.

2.2 Ionisation

In the three-step model of HHG, ionisation plays an essential role, and so ionisation is necessarily significant whenever HHG is. Depending on the parameter regime, one of several models for ionisation may be appropriate. To define these regimes, it is useful to consider figure 2.5, which shows the potential seen by a bound electron as the sum of the nuclear and laser electric

fields. The net potential has a local maximum, the height of which decreases with increasing laser intensity. At a critical intensity, this maximum value of the potential equals the binding energy of the unperturbed atom, and the electron is no longer bound. In hydrogen one can calculate the critical intensity for this “over-the-barrier ionisation” process to be

$$I_{\text{otb}} = \frac{\pi^2 c \epsilon_0^3 U_{\text{H}}^4}{2e^6} = 1.4 \times 10^{14} \text{ W/cm}^2 \quad (2.5)$$

where U_{H} is the ionisation energy of hydrogen. At intensities below the critical value for the over-the-barrier process, electrons can still move past the local potential maximum by tunneling. This picture of ionisation by distortion of the binding potential – either by tunneling or over-the-barrier – is termed “optical field ionisation” (OFI). Since laser electric fields are oscillatory rather than static, the OFI picture is only valid if the electron wave packet has time to move significantly before the laser field reverses. It turns out that this condition is equivalent to

$$\gamma = \sqrt{U_{\text{i}}/2U_{\text{p}}} < 1 \quad (2.6)$$

where U_{i} is the ionisation energy and γ is known as the Keldysh parameter. In the regime of HHG experiments, intensities are sufficiently high (10^{13} - 10^{15} W/cm²) and laser frequencies sufficiently low that γ is indeed small.

In this typical HHG regime, the ionisation rate can be approximated by the Ammosov-Delone-Krainov (ADK) model: [31, 32]

$$W_{\text{OFI}}(t) = \frac{\omega_0}{2} C_{n^*l}^2 \frac{U_{\text{i}}}{U_{\text{H}}} \chi \left[2 \left(\frac{U_{\text{i}}}{U_{\text{H}}} \right)^{3/2} \frac{E_{\text{H}}}{E(t)} \right]^{2n^* - |m_l| - 1} \exp \left[-\frac{2}{3} \left(\frac{U_{\text{i}}}{U_{\text{H}}} \right)^{3/2} \frac{E_{\text{H}}}{E(t)} \right] \quad (2.7)$$

where

$$\chi = \frac{(2l+1)(l+|m_l|)!}{2^{|m_l|} |m_l|! (l-|m_l|)!} \quad (2.8)$$

$E(t)$ is the laser electric field, $E_{\text{H}} = e/4\pi\epsilon_0 a_0^2$ is the electric field in hydrogen at the Bohr radius a_0 , C_{n^*l} is a constant of order 2, l and m_l are quantum numbers of the outermost electron, $n^* = Z\sqrt{U_{\text{H}}/U_{\text{i}}}$ is the effective principal quantum number, and $\omega_0 = m_e e^4 / (4\pi\epsilon_0)^2 \hbar^3$ is the atomic unit of frequency. As before, U_{H} is the hydrogen binding energy and U_{i} is the ionisation

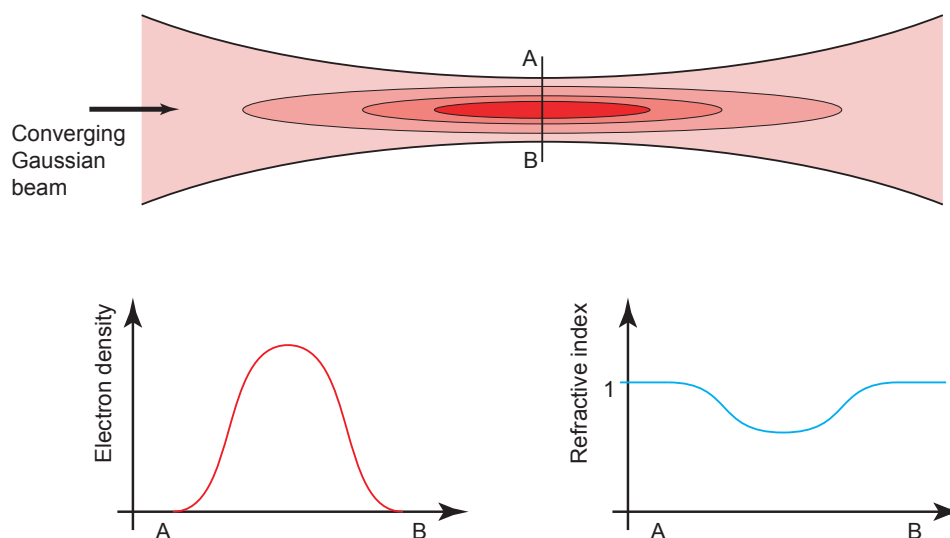


FIGURE 2.6: Ionisation produced by a focusing beam acts as a diverging lens, causing the focused intensity to be less than in vacuum. Figure adapted from [34].

energy of the species in question.

For conditions where $I \ll I_{\text{otb}}$ or $\gamma > 1$, other “multi-photon ionisation” mechanisms may be relevant. The multi-photon rates are more complicated to calculate, typically depending on the details of the atomic energy level spectrum. Further ionisation can be caused by collisions between neutrals and the quivering electrons. Unlike direct ionisation by the laser field, this collisional ionisation increases with density. While significant for high-density laser-ablation plasmas [33], collisional ionisation is typically insignificant in the low density gases used for HHG [34]. Since OFI is the dominant ionisation mechanism in the regime of HHG experiments, estimation of ionisation rates for the rest of this thesis will be made using the ADK model (eq. 2.7).

2.3 Defocusing

One limitation of HHG is that it is hard to maintain the requisite high intensity over a long length. The beam will rapidly diverge after the focus, unless a waveguide is used as will be discussed in chapter 3. For an ideal Gaussian beam, the longitudinal distance past the focus for which the intensity has dropped to half its peak value is known as the Rayleigh range b . $b \approx 1$ mm for realistic experimental conditions.

However, when gas is present, the interaction length and peak intensity may be less than their vacuum values due to the following mechanism. If the peak intensity is sufficient for ionisation to occur, the higher intensity on axis produces an axially peaked density of free electrons. The index of refraction due to free electrons is given by

$$\eta_e = \sqrt{1 - \left(\frac{\omega_p}{\omega}\right)^2}, \quad \omega_p = \sqrt{\frac{n_e e^2}{\epsilon_0 m_e}} \quad (2.9)$$

where n_e is the density of free electrons and ω_p is the plasma frequency. Thus, the index of refraction is diminished on axis, and so the gas becomes a diverging lens (figure 2.6). Thus, significant ionisation leads to distortion of the beam. In particular, the peak intensity is reduced, as is the length over which the beam is tightly focused [35]. Ionisation-induced defocusing limits the achievable intensity and interaction length for the high-pressure and high-intensity range of HHG parameters.

2.4 Blueshifting

If a beam of wavelength λ_0 is used to produce high-order harmonics, order q ideally appears at wavelength λ_0/q . However, shifting of both the fundamental and harmonic light towards bluer frequencies has been observed in both simulations [16, 33, 37–42] and experiments [36, 43, 44]. For high-order harmonics, the deviation from the nominal λ_0/q wavelength may approach or exceed the spacing between adjacent harmonics (see Figure 2.7). An understanding of blueshifting will be useful in interpreting experimental data later in this thesis. Two mechanisms which produce blueshifting are relevant to the experiments discussed in this thesis.

2.4.1 Ionisation blueshifting

One cause of blueshifting is ionisation. Since the dispersion due to free electrons (equation 2.9) depends on the free electron density, an increasing degree of ionisation gives rise to a

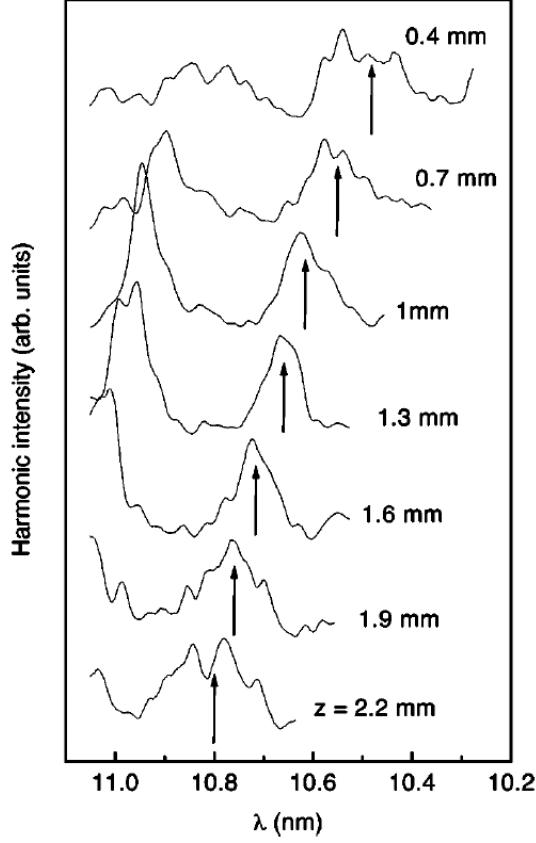


FIGURE 2.7: Shift in wavelength of the $q = 73$ harmonic as the laser focus is moved longitudinally by z relative to a Ne gas jet, which therefore varies the degree of blueshift. The unshifted position for $q = 73$ is 10.9 nm. Figure taken from [36].

time-dependent index of refraction:

$$\frac{d\eta}{dt} = \frac{d\eta}{d\omega_p} \frac{d\omega_p}{dn_e} \frac{dn_e}{dt} = \frac{\omega_p^2 \lambda^2}{8\pi^2 c^2 \eta} \frac{dZ}{dt} \quad (2.10)$$

where $Z(t)$ is the degree of ionisation, given by $n_e(t)$ divided by the original gas density at $t = -\infty$. Consider two phase fronts in the wave that pass a particular location z separated by a time δt . While the first front is traveling at speed $v_1 = c/\eta$, the later phase front sees more free electrons and so moves at the slightly different speed $v_2 = c/[\eta + \delta t (d\eta/dt)]$. Thus, in time δt , the $\delta t c/\eta \lambda$ cycles between the two phase fronts are compressed by a distance $(v_2 - v_1)\delta t$:

$$\delta\lambda = -\frac{(v_2 - v_1)\delta t}{\frac{\delta t c}{\eta \lambda}} = -\frac{\frac{c}{\eta} - \frac{c}{\eta + \delta t (d\eta/dt)}}{\frac{c}{\eta \lambda}} \approx -\delta t \frac{\lambda}{\eta} \frac{d\eta}{dt} = -\delta L \frac{\lambda}{c} \frac{d\eta}{dt} \quad (2.11)$$

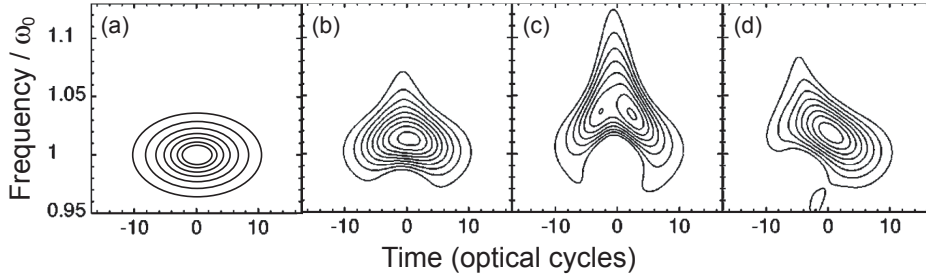


FIGURE 2.8: Ionisation-blueshifting of a laser pulse. Variation of the pulse frequency with time is shown using the Wigner distribution $W(t, \omega) = \int E^*(t + \tau)E(t - \tau)e^{i\omega\tau}d\tau$. (a) Qualitative illustration by the author of initial pulse before interaction with gas. (b)-(d) Simulation results taken from Kim *et al.* [42] for a 30 fs FWHM 800 nm pulse after propagating through 700 μm of Ne. In (b) and (c) the peak intensity is $1 \times 10^{15} \text{ W/cm}^2$, low enough that Z remains less than 1. Thus, the $t = 0$ peak is shifted more than the wings, and the wings are roughly symmetric about $t = 0$. In (c) the density (121 mbar) is higher than in (b) (40 mbar), so the blueshifting is more severe. In (d), also 40 mbar, the higher intensity ($3 \times 10^{15} \text{ W/cm}^2$) causes significant depletion of neutral atoms. Thus, the trailing edge of the pulse ($t > 0$) causes little ionisation, and so it is shifted less than the $t < 0$ leading edge.

where δL is the distance traveled by the leading wave front. Hence,

$$\frac{\delta\lambda}{\delta L} = -\frac{\omega_p^2 \lambda^3}{8\pi^2 c^3} \frac{dZ}{dt} \quad (2.12)$$

and so the ionisation rate leads to a proportional blueshift. Through the ω_p^2 factor, the shift is linearly proportional to density so long as the ionisation rate dZ/dt has no significant contribution from collisions.

Since the ionisation rate changes during the pulse, different parts of the pulse are blueshifted differently, as shown in figure 2.8. The high-intensity peak of the pulse is shifted more than the leading and trailing wings. If the total degree of ionisation caused by the pulse $Z(\infty)$ is less than 1, the trailing wing of the pulse will be blueshifted by roughly the same amount as the leading wing. However, if Z approaches or exceeds 1, the trailing wing can cause less ionisation than the leading wing because the relevant ionisation energy is higher. Consequently, the latter half of the pulse is not blueshifted.

Ionisation blueshifting can affect harmonics in two ways: by directly shifting the harmonic radiation, and by shifting the fundamental light from which the harmonics derive. Because the fractional blueshift $\delta\lambda/\lambda$ is proportional to λ^2 , the direct shifting is a factor q^2 smaller than the

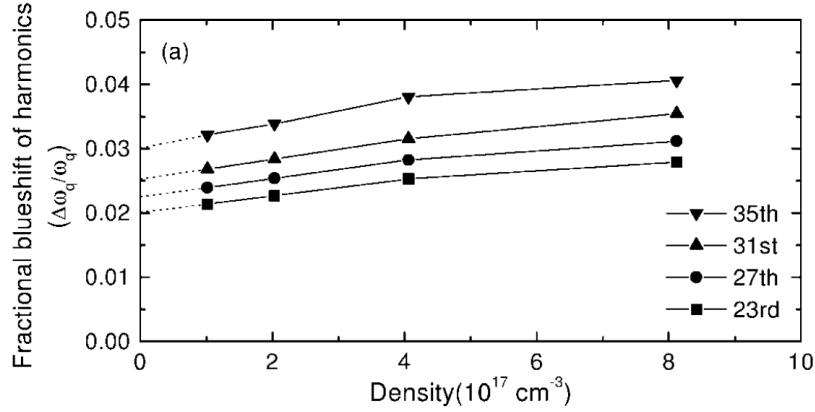


FIGURE 2.9: Variation in fractional blueshift of Ar harmonics with density for a 30 fs laser pulse. The effect at zero density is purely due to the nonadiabatic blueshift mechanism. The additional blueshift for pressure > 0 is due purely to the ionisation mechanism. Figure taken from [40].

indirect effect. The direct shifting of high-order harmonics is therefore neglected.

2.4.2 Nonadiabatic blueshifting

A second mechanism for blueshifting involves the dependence of the harmonic phase on the driving laser intensity. From equation 2.4, the phase ϕ of the harmonic emission is a decreasing function of driving intensity. In the first half of the pulse, the rising intensity means $d\phi/dt < 0$. Since the time variation of the total harmonic phase is given by $-q\omega_0 t + \phi(t)$, then in the first half of the pulse the frequency effectively increases and so harmonics will be blueshifted. The harmonics are redshifted in the second half of the pulse as the intensity decreases. If harmonic generation occurs equally before and after the pulse peak, then the redshift and blueshift effects are roughly equal in magnitude, and so the harmonic pulse grows wider but not bluer overall. However, in some situations, harmonic generation occurs primarily before the pulse peak. This could be due to either depletion of the neutral atom species¹ or worsening phase matching conditions (discussed in Chapter 4). Through either of these effects the HHG from the leading half of the pulse may exceed that from the trailing half, causing the blueshift to exceed the redshift in the resulting harmonic radiation.

This second “nonadiabatic” blueshift mechanism differs from the ionisation-blueshifting mechanism in how it scales with several experimental parameters. One noteworthy difference is

¹Ions, having much more tightly bound electrons, have a lower single-atom efficiency for harmonic generation.

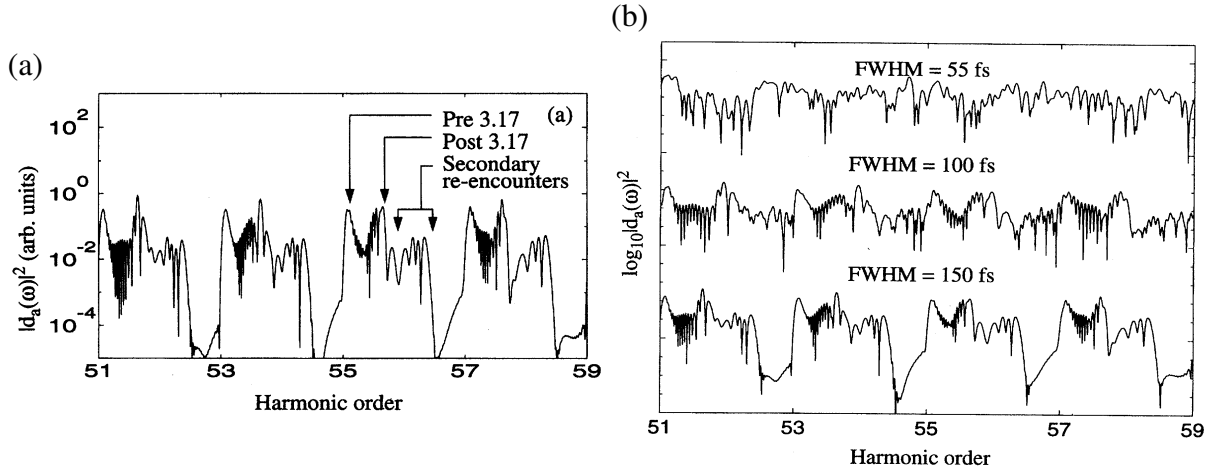


FIGURE 2.10: (a) Kan *et al.* find that the various peaks in the single-atom HHG spectrum correspond to different quasi-classical trajectories, which are nonadiabatically blueshifted by different amounts. (b) For shorter driving pulses, the increased $|dI/dt|$ causes greater frequency shifts, causing the harmonics to merge with adjacent orders. Figure taken from [39].

that the nonadiabatic mechanism is independent of gas density whereas the ionisation mechanism is proportional to density. Therefore the relative contributions of the two processes can be deduced from a scan of pressure. Figure 2.9 shows such a scan for experimental conditions in which both mechanisms are observed.

2.4.3 Harmonic peak splitting

Earlier, figure 2.3 showed that simulated single-atom HHG spectra exhibit very structured harmonic peaks. This structure can be interpreted as the result of nonadiabatic blueshifting, as follows. Recall that equation 2.4 for the phase of harmonic emission can be applied separately to each quasi-classical trajectory, as in figure 2.4. The sensitivity of the phase to intensity ($|d\phi/dI|$) is proportional to a constant K that is larger for longer trajectories. The nonadiabatic blueshift is in turn proportional to $|d\phi/dI|$, so longer trajectories experience more of this frequency shift. Kan *et al.* have used a single-atom simulation to identify particular harmonic peaks with particular electron trajectories (figure 2.10). Indeed, they find that the trajectories of greater duration are blueshifted the most. As the pulse length is shortened, the increased $|dI/dt|$ strengthens the shifting and widens the peaks. Only one trajectory is possible for harmonics at the cutoff, so in this region the peaks are not similarly split (e.g., see figure 2.3).

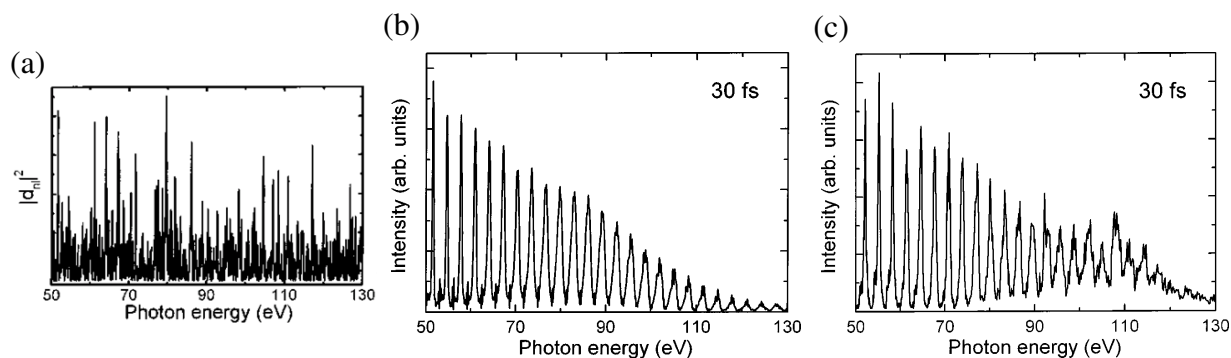


FIGURE 2.11: The modification of the single-atom response due to propagation effects. (a) The original single atom spectrum. In (b), the single-atom responses are combined using a propagation code that considers a realistic Gaussian focus. (c) shows experimental measurements from a pulse and focus geometry matched to the parameters simulated in (b). Figures from [45].

There is another important consequence of the increased $|d\phi/dI|$ for longer trajectories: in a macroscopic experiment it is likely that the contributions of the longer trajectories will not add in phase. HHG-emitting atoms in slightly different locations will see slightly different intensities, but because of the high $|d\phi/dI|$, the atoms will be vastly out of phase. Thus, contributions from long trajectories are suppressed in the macroscopic emission relative to their levels in the single-atom spectrum. This effect is shown dramatically by Priori *et al.*[45]. Simulated spectra reproduced in figure 2.11 show the disappearance of the structured lineshapes when single-atom contributions are aggregated.

After the discussion of phase matching in Chapter 4, additional peak-splitting processes will be described. These mechanisms involve the combined effects of many atomic harmonic emitters, in contrast with the single-atom mechanism discussed above.

CHAPTER 3

Grazing-incidence waveguides

As discussed previously, diffraction and ionisation place an upper limit on the length over which a high laser intensity can be maintained. To overcome these problems, waveguides can be used to confine a beam to a small diameter over a longer distance. This thesis considers only cylindrical step-index waveguides, formed by a dielectric “core” material of refractive index η_i surrounded by a coaxial cylindrical dielectric “cladding” of refractive index η_o . Waveguides can also be formed using a plasma of radially varying refractive index [46]. Experiments with HHG in these devices were not conducted by the author due in part to their added experimental complexity, though these plasma waveguides may be useful for future studies [47].

3.1 Modes of the step-index waveguide

For the case $\eta_i > \eta_o$, light in the core experiences total internal reflection at the core-cladding interface, and the modes are therefore lossless. However, if high-order harmonics are to be made in the interior region, the index of refraction there will be that of a low-density gas: $|\eta_i - 1| \ll 1$. Aside from the case of a plasma waveguide, which has already been discounted, all reasonable cladding materials will have $\eta_o \geq 1.4$. In this regime of $\eta_i < \eta_o$, light in the core cannot be totally internally reflected by the core-cladding boundary, so the modes will be lossy.

A detailed derivation of the modes of a step-index waveguide can be found in many sources [48–50]; results will only be summarised here. The most mathematically direct derivation of

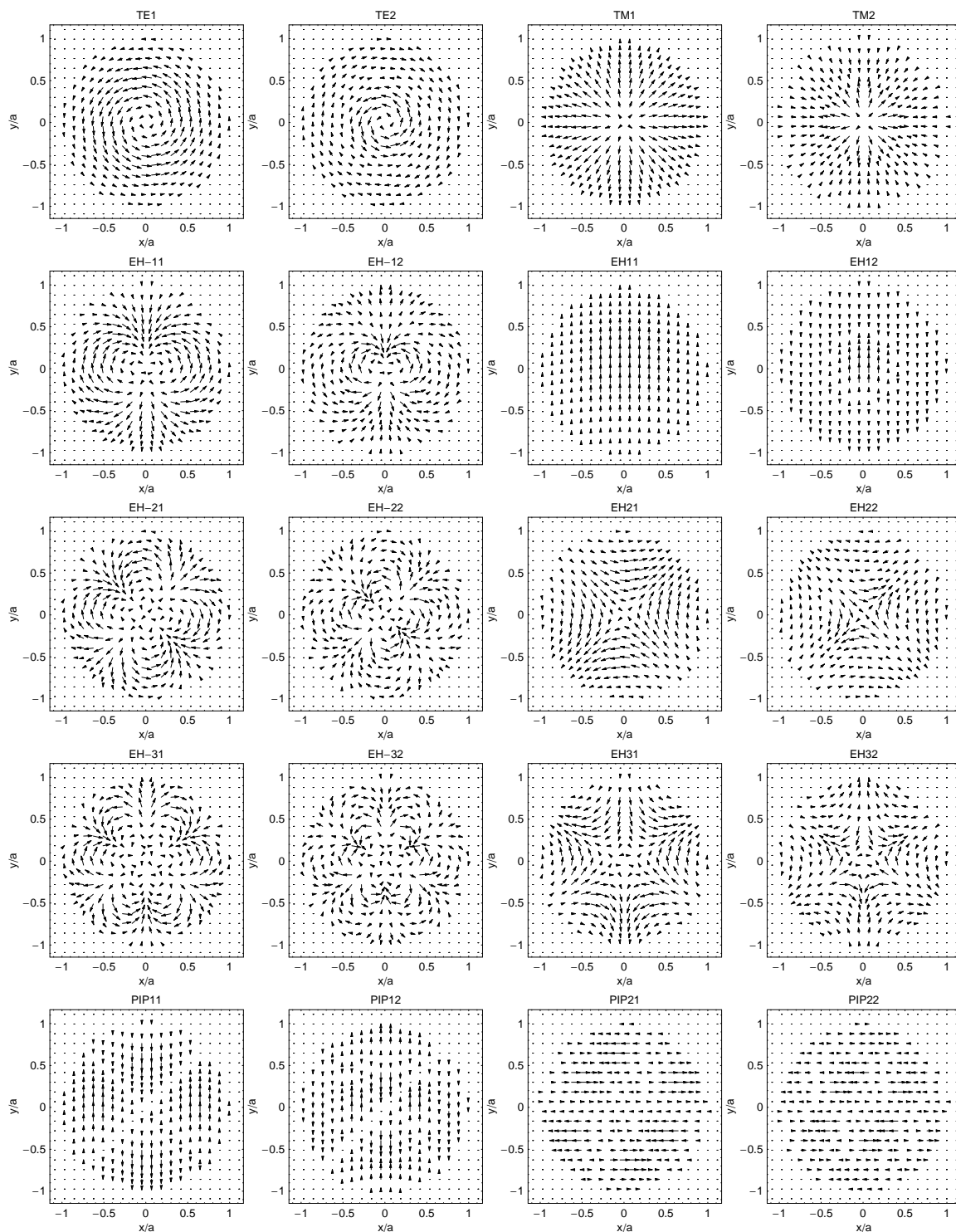


FIGURE 3.1: The electric field vectors for several of the step-index capillary modes.

the guided modes results in the following three categories:

- Transverse electric modes, denoted $TE_{0,p}$, where $p \in \{1, 2, 3, \dots\}$. There is no longitudinal electric field. There is a longitudinal magnetic field, which is smaller than the transverse magnetic field by a factor of order λ_0/a , where a denotes the radius of the core, and λ_0 is the vacuum wavelength of the light.
- Transverse magnetic modes, denoted $TM_{0,p}$, where $p \in \{1, 2, 3, \dots\}$. There is no longitudinal magnetic field. The longitudinal electric field is smaller than the transverse electric field by a factor of order λ_0/a .
- Hybrid modes, denoted $EH_{j,p}$, where $j \in \{\dots, -3, -2, -1, 1, 2, 3, \dots\}$ and $p \in \{1, 2, 3, \dots\}$. There is both a longitudinal electric field and a longitudinal magnetic field, both smaller than their respective transverse components by factors of order λ_0/a .

Several of these modes are shown in figure 3.1. For all of the above cases, an evanescent wave extends into the cladding, and its fields are smaller than the fields in the core by a factor of order λ_0/a . All of these modes except for the $EH_{1,p}$ series have a spatially dependent polarisation (i.e., vertically polarised in some regions, horizontally in others). Since the light entering the waveguide has a position-independent polarisation (PIP), it is convenient to form linear combinations of the EH modes that share this property. The $PIP_{j,p}$ modes are constructed as follows:

$$PIP_{j,p} = \begin{cases} EH_{1,p} & \text{if } j = 0 \\ EH_{-j,p} + EH_{j+2,p} & \text{if } j > 0 \end{cases} \quad (3.1)$$

for $j \in \{0, 1, 2, \dots\}$, $p \in \{1, 2, 3, \dots\}$.

Note that the PIP modes include no linear combinations of the $EH_{2,p}$ series, so this series is still needed to form a complete set. The modes most relevant for this thesis are the $PIP_{j,p}$ family. The propagation constants of these PIP modes are given by $k_{j,p}(\omega) = \beta_{j,p}(\omega) + i\alpha_{j,p}(\omega)$ where

$$\beta_{j,p}(\omega) = \frac{\omega}{c} - \frac{u_{j,p}^2 c}{2\omega a^2} \quad (3.2)$$

$$\alpha_{j,p}(\omega) = \frac{u_{j,p}^2 c (1 + \eta_0^2)}{2a^2 \omega^2 \sqrt{\eta_0^2 - 1}} \quad (3.3)$$

where $u_{j,p}$ is the p -th root of the Bessel function $J_j(x)$, and η_i has been taken to be ≈ 1 . The nonzero imaginary part α gives the inverse scale length for decay of the mode due to reflection losses. Due to the $u_{j,p}^2$ dependence, the loss length grows smaller as either j or p increase. The waveguide therefore has a spatial filtering effect, with high order modes being suppressed relative to the PIP_{0,1} mode. This “lowest order” mode – equivalent to EH_{1,1} – has the simplest spatial pattern, and as shall be apparent in the next section, it is also the mode which can be most efficiently excited.

3.2 Coupling into a capillary

When a distribution of light with electric field $\text{Re}[\mathbf{E}_{\text{in}}(r, \theta) e^{-i\omega t}]$ is created at the entrance of a grazing-incidence waveguide, some mixture of TE_{0,p}, TM_{0,p}, PIP_{j,p}, and EH_{2,p} modes will be excited. These modes form a basis of orthogonal functions over the space of possible fields in the $z = 0$ plane, and so any input field can be decomposed by taking an inner product. A mode with electric field $\text{Re}[\mathbf{E}_{\text{m}}(r, \theta, z) e^{i(kz - \omega t)}]$ and normalised such that $\iint |\mathbf{E}_{\text{m}}(r, \theta, 0)|^2 2\pi r dr d\theta = 1$ will be excited by an amplitude

$$C = \iint \mathbf{E}_{\text{m}}(r, \theta, 0) \cdot \mathbf{E}_{\text{in}}^*(r, \theta) 2\pi r dr d\theta. \quad (3.4)$$

The fraction of the input power which is coupled to the mode is given by C^2/P , where $P = \iint |\mathbf{E}_{\text{in}}(r, \theta)|^2 2\pi r dr d\theta$ is the norm-squared of the input.

The only axisymmetric modes are the PIP_{0,p} series, so for an axisymmetric laser focus pointed properly into a capillary, only these modes will be active. Figure 3.2 shows the fractional power coupling C^2/P into these modes for the case where the capillary input is a Gaussian spot with a $1/e^2$ intensity radius of w_0 . For this situation, the coupling amplitudes are given by

$$C_p = \frac{2\sqrt{2Pa}}{w_0 J_1(u_{0,p})} \int_0^1 J_0(\rho u_{0,p}) \exp\left[-\left(\frac{\rho a}{w_0}\right)^2\right] \rho d\rho \quad (3.5)$$

The most selective coupling occurs when $w_0 = 0.645a$, in which case 98% of the power goes into the lowest order mode.

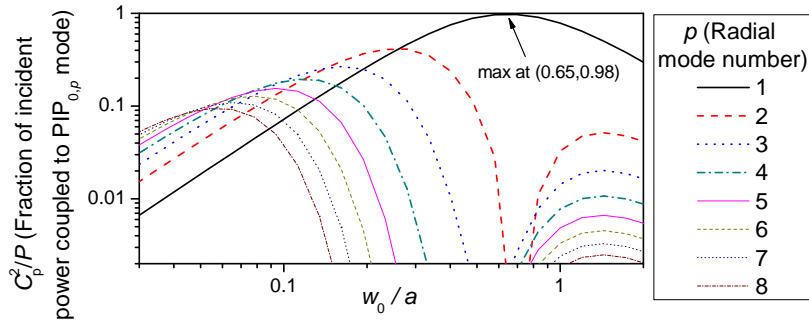


FIGURE 3.2: The fraction of power coupled into various capillary modes when a Gaussian beam is focused to a spot of $1/e^2$ intensity radius w_0 at the entrance of a hollow capillary with radius a . The figure is obtained by plotting C_p^2/P where C_p is given by equation 3.5.

3.3 Mode beating

As the propagation constants differ for the different modes (equation 3.2), the modes will beat with each other as they propagate. The intensity on axis can be computed as

$$I(z) = \frac{\epsilon_0 c}{2} \left| \sum_p A_p e^{ik_{0,p}(\omega)z} \right|^2 \quad (3.6)$$

where the coefficients A_p are obtained by multiplying the C_p coefficients by the value of the normalised mode on axis:

$$A_p = C_p \frac{1}{a\sqrt{\pi}J_1(u_{0,p})} \quad (3.7)$$

The resulting axial intensity for various realistic situations is illustrated in figure 3.3. The variations in intensity can be severe even for a well-matched input spot. Because the higher order modes decay over a shorter length, the intensity stabilises after a distance on the order of the absorption distance for the lowest-order mode.

Since the modes experience different group velocities, the beating pattern will depend on the pulse length. As long as the spread of the modes in time is small compared to the pulse duration, the beating pattern will change little from the CW pattern. However, if the spread between modes is large compared to the pulse duration (i.e., the original pulse has broken up into a series of separated pulses) then the interference effects disappear. The mode separation will be linearly proportional to propagation distance. After propagation through 100 mm of a

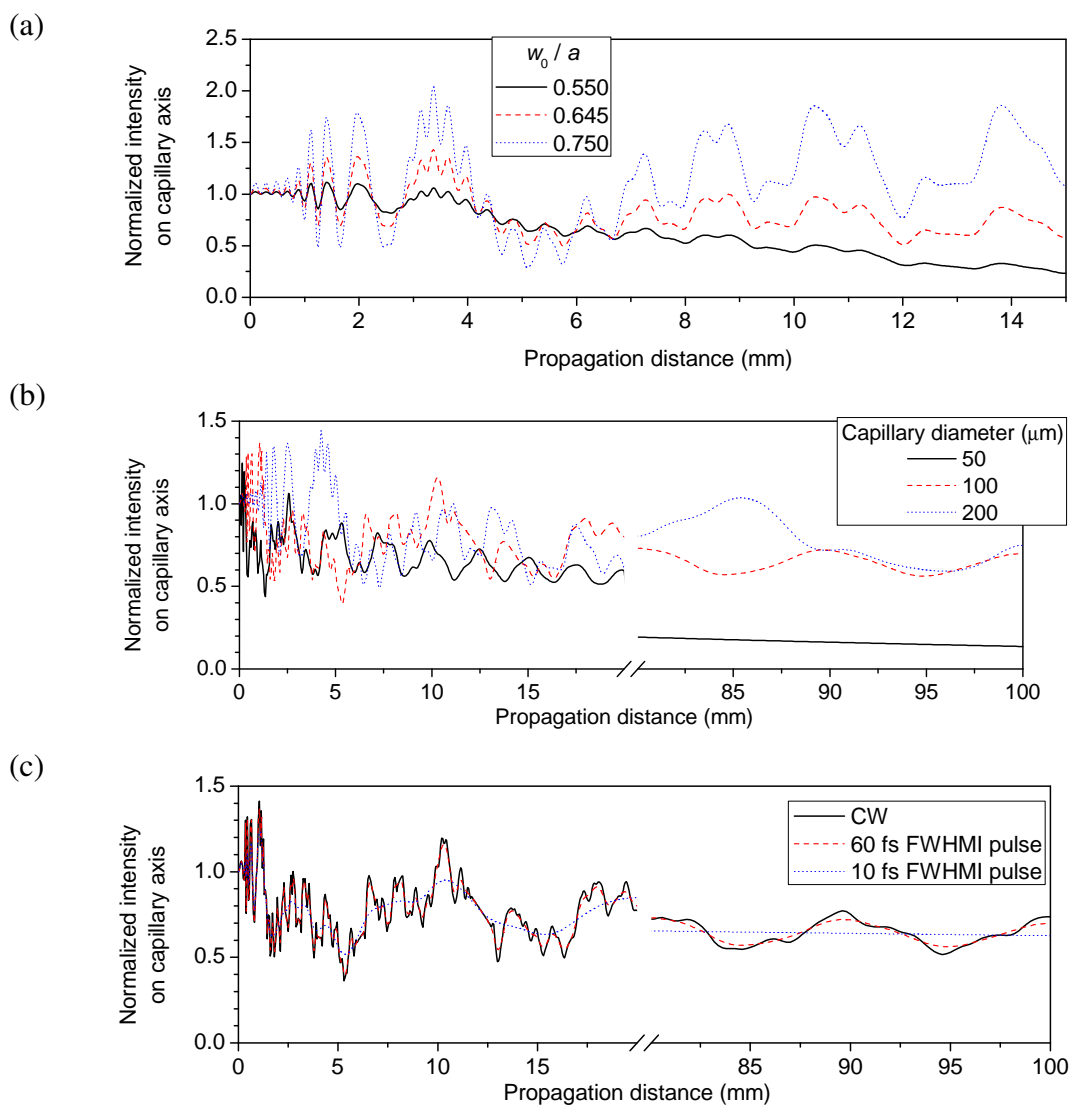


FIGURE 3.3: Beating between capillary modes for several realistic situations. (a) Gaussian spots of varying radius guided in a 178 μm diameter capillary. (b) Ideally matched ($w_0/a = 0.645$) Gaussian beams guided in capillaries of various diameters. After 100 mm, the beating is completely gone in the 50 μm capillary, though much of the intensity has been lost as well. (c) Beating is reduced for short pulses because the modes separate from each other as they propagate. In all plots, intensities are normalised by the $z = 0$ intensity.

100 μm diameter capillary, the fundamental mode pulls ahead of the next $\text{PIP}_{0,p}$ modes by 27, 75, and 144 fs respectively. Thus, for pulses in these capillaries with duration on the order of 100 fs or shorter, both the driver and harmonics will emerge stretched in time, and the mode beating will be reduced from the pattern for CW light. Figure 3.3.c shows a comparison between the time-independent CW beating pattern and the intensity pattern for 60 fs and 10 fs pulses. For the pulsed case the intensity varies with time, so the intensity plotted is $I(z, z/v_{g1})$ where $I(z, t)$ is the intensity at a given position and time and v_{g1} is the group velocity of the lowest-order mode. That is, at each z , the intensity is plotted for the time of the peak in the lowest order mode; this is roughly the maximum intensity experienced at any time for this z . Parts a and b of the figure show the beat pattern as a function of capillary and input spot diameter, again plotting $I(z, z/v_{g1})$ for a 60 fs pulse.

3.4 Previous experiments

The first experiments to use grazing incidence waveguides at the requisite laser intensities for HHG were conducted in the 1990s at the Naval Research Laboratory [51] and at the Rutherford Appleton Laboratory's Vulcan laser [52]. Both groups studied only evacuated capillaries. Neither group attempted to achieve the ideal $w_0 = 0.645a$ matching criterion, nor did either group mention this idea in their analysis.

The Vulcan experiment used only 10 mm or shorter capillaries, measuring $\sim 50\%$ transmission through a 10 mm long, 100 μm diameter waveguide. Though the diffraction-limited spot size for their setup was roughly 6 μms , the measured spot size was over 50 μms , indicating a poor spot quality.

The NRL group observed $\sim 20\%$ transmission through 126 mm long, 266 μm diameter capillaries for a 4 mJ laser pulse. The transmission dropped to $\sim 7\%$ when the laser energy was raised to 1 J. X-ray emission was detected for the 1 J shots, indicating that the capillary walls had ionised, and so the laser was guided by reflection from the wall plasma. No wall ionisation was detected for the 4 mJ shots. As the focal spot size was $\sim 19 \mu\text{ms}$, the 266 μm diameter capillaries were much larger than the matched size.

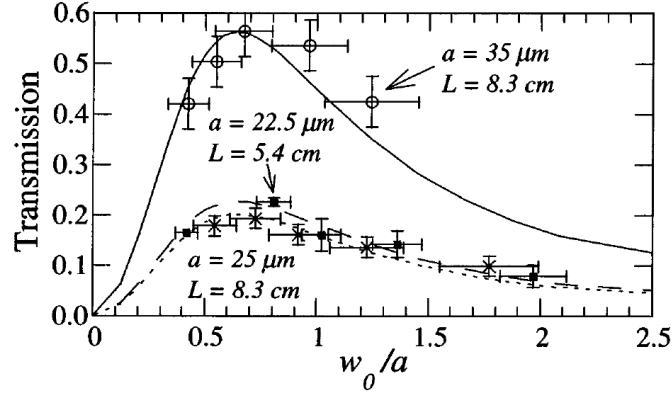


FIGURE 3.4: Points show the transmission measured by Dorchie *et al* for evacuated capillaries with various values of capillary radius a , length L , and input spot size w_0 . Curves plot equation 3.8, where α is given by equation 3.3 for the lowest-order mode, and C is given by the measured fraction of input laser energy within the capillary radius. Figure from [53].

More recent experiments by Cros *et al*[53, 54] have shown that guiding is indeed optimised when the capillary and spot sizes satisfy the matching condition, as shown in figure 3.4. Guiding was studied for a wide range of capillary diameters (40-70 μms) and spot sizes (14-46 μms) such that $w_0/0.645a$ varied between 0.6 and 4. Experiments were also conducted for a wide range of capillary lengths (1-10 cm). Over these parameters, and for gas pressures from 40 mbar down to an unspecified vacuum, the output of the capillary was observed to closely resemble the lowest-order mode. The variation in transmission T with capillary length L was found to follow obey the empirical rule

$$T = Ce^{-2\alpha L} \quad (3.8)$$

For evacuated capillaries, the decay constant α was accurately predicted by the formula 3.3 for the lowest-order mode. Filling the capillary with gas was found to both decrease C and increase α . The authors hypothesise that the decreased coupling was due to ionisation-induced defocusing before the capillary entrance. The surmised explanation for the increased α was that ionisation-induced defocusing caused transfer of energy to higher-order (and hence rapidly decaying) modes inside the bore. In the experiments, the entire chamber was brought to the desired pressure, not just the capillary bore. This technique could not be used for HHG experiments, because such a density of gas would absorb the XUV light over a short propagation distance.

CHAPTER 4

Phase matching of harmonics

This chapter discusses the aggregation of the high-harmonic emission from single atoms into the macroscopic wave. In the Introduction it was discussed qualitatively how this macroscopic emission was limited if dispersion were present; this effect is now calculated rigorously. Then, considering the various sources of dispersion, it is shown how dispersive effects can be balanced for moderate harmonic orders. For the highest harmonic orders, however, phase matching cannot be achieved. Quasi phase matching is a potential alternative, and it is described here more precisely. Finally, previous experiments regarding the phase matching and quasi phase matching of HHG are discussed.

4.1 Harmonic wave growth

Many nonlinear optics texts give derivations of harmonic wave growth that are ill-suited for discussing high harmonic generation, some assuming that effects are perturbative, others using lengthy notation in order to encompass other processes like difference frequency mixing. Thus, a modified derivation is given here which is tailored for HHG.

Though the driving radiation in any real HHG experiment will vary with time and space, it is instructive to consider first the case in which the driving radiation (and hence the harmonics) are CW plane waves. Consider an intense plane wave traveling in the $+z$ direction, passing through a nonlinear medium that occupies the volume $z \in [0, L]$. Let x be the direction of the

electric field (and hence of the induced polarisation). The driving electric field has the form

$$E^{(\omega)}(z, t) = \frac{E_0^{(\omega)}}{2} e^{i[k(\omega)z - \omega t]} + \text{c.c.} \quad (4.1)$$

If the efficiency of energy conversion into the harmonics were high, depletion of this driving wave would need to be considered. In practice, conversion efficiencies are $\ll 1$, so this detail will be ignored. Consider the atoms in the nonlinear medium at $z = 0$. They experience a driving field of

$$E^{(\omega)}(0, t) = \frac{E_0^{(\omega)}}{2} e^{-i\omega t} + \text{c.c.} \quad (4.2)$$

and, due to their nonlinear response, there is an oscillating polarisation at higher frequencies.

At the frequency $q\omega$, for example, there is a polarisation

$$P_{\text{NL}}^{(q\omega)}(0, t) = \frac{P_{\text{NL},0}^{(q\omega)}}{2} e^{-iq\omega t} + \text{c.c.} \quad (4.3)$$

The subscript NL is used to distinguish this nonlinearly-driven polarisation from any linear response $P_{\text{L}}^{(q\omega)}(z, t) \propto E^{(q\omega)}(z, t)$ that may also be present. The coefficient $P_{\text{NL},0}^{(q\omega)}$ is in general complex, and its phase is identical to ϕ of equation 2.4. $P_{\text{NL},0}^{(q\omega)}$ is a function of the atom species and the electric field magnitude, and its value could be computed from simulations of the Schrodinger equation. At other z values, the electric field looks identical to the time-delayed electric field at $z = 0$:

$$E^{(\omega)}(z, t) = E^{(\omega)}(0, t - k(\omega)z/\omega) \quad (4.4)$$

Since the atoms know nothing of their z coordinate, and since the system is invariant under time translation, the polarisation wave for $z > 0$ must obey the same time-delay relation as the electric field:

$$P_{\text{NL}}^{(q\omega)}(z, t) = P_{\text{NL}}^{(q\omega)}(0, t - k(\omega)z/\omega) \quad (4.5)$$

$$= \frac{P_{\text{NL},0}^{(q\omega)}}{2} e^{i[qk(\omega)z - q\omega t]} + \text{c.c.} \quad (4.6)$$

This polarisation wave will drive an electric field oscillation at this same frequency. To exam-

ine in detail how this electromagnetic wave grows, consider the $q\omega$ -frequency component of Maxwell's wave equation:

$$\nabla^2 E^{(q\omega)} + k(q\omega)^2 E^{(q\omega)} = -\mu_0 q^2 \omega^2 P_{\text{NL}}^{(q\omega)} \quad (4.7)$$

where the linear part of the polarisation has been accounted for in writing $k(q\omega)$. The electric field solution can be written as a wave times an envelope function $\mathcal{E}^{(q\omega)}(z)$:

$$E^{(q\omega)}(z, t) = \frac{\mathcal{E}^{(q\omega)}(z)}{2} e^{i[k(q\omega)z - q\omega t]} + \text{c.c.} \quad (4.8)$$

Plugging this and the polarisation expression 4.6 into the wave equation 4.7 gives

$$\begin{aligned} \left(\frac{d\mathcal{E}^{(q\omega)}}{dz} \right) [ik(q\omega)] e^{i[k(q\omega)z - q\omega t]} + \frac{1}{2} \left(\frac{d^2\mathcal{E}^{(q\omega)}}{dz^2} \right) e^{i[k(q\omega)z - q\omega t]} + \text{c.c.} \\ = -\frac{\mu_0 q^2 \omega^2}{2} P_{\text{NL},0}^{(q\omega)} e^{i[k(q\omega)z - q\omega t]} + \text{c.c.} \end{aligned} \quad (4.9)$$

The second term can be dropped because $\mathcal{E}^{(q\omega)}$ is assumed to vary on a length scale much longer than $k(q\omega)^{-1}$:

$$\left(\frac{d\mathcal{E}^{(q\omega)}}{dz} \right) [ik(q\omega)] e^{i[k(q\omega)z - q\omega t]} + \text{c.c.} = -\frac{\mu_0 q^2 \omega^2}{2} P_{\text{NL},0}^{(q\omega)} e^{i[k(q\omega)z - q\omega t]} + \text{c.c.} \quad (4.10)$$

Since this last equation holds for any t , the equation is equally valid without the complex conjugate terms. Rearranging,

$$\frac{d\mathcal{E}^{(q\omega)}}{dz} = \frac{i\mu_0 q^2 \omega^2 P_{\text{NL},0}^{(q\omega)}}{2k(q\omega)} e^{iz[qk(\omega) - k(q\omega)]} \quad (4.11)$$

It is useful here to introduce the wave vector difference $\Delta k = qk(\omega) - k(q\omega)$, and many of the other factors can be collected into a new quantity $A^{(q\omega)} = i\mu_0 q^2 \omega^2 P_{\text{NL},0}^{(q\omega)} / [2k(q\omega)]$:

$$\frac{d\mathcal{E}^{(q\omega)}}{dz} = A^{(q\omega)} e^{i\Delta k z} \quad (4.12)$$

$$\mathcal{E}^{(q\omega)}(z) = \int_0^z A^{(q\omega)} e^{i\Delta k z'} dz' = \frac{A^{(q\omega)}}{i\Delta k} (e^{i\Delta k z} - 1) \quad (4.13)$$

Finally, the intensity of the harmonic wave is obtained from the absolute square of the electric field:

$$I^{(q\omega)}(z) = \frac{\epsilon_0 c}{2} |E^{(q\omega)}(z, t)|^2 = \frac{\epsilon_0 c}{2} |E^{(q\omega)}(z)|^2 = \frac{4\epsilon_0 c [A^{(q\omega)}]^2}{\Delta k^2} \sin^2\left(\frac{\Delta k z}{2}\right) \quad (4.14)$$

Hiding several factors in the quantity $B^{(q\omega)} = 4\epsilon_0 c [A^{(q\omega)}]^2$, an expression for the growth of the harmonic wave is:

$$I^{(q\omega)}(z) = B^{(q\omega)} \Delta k^{-2} \sin^2\left(\frac{\Delta k z}{2}\right) \quad (4.15)$$

In the phase-matched limit $\Delta k \rightarrow 0$, the growth becomes quadratic:

$$I^{(q\omega)}(z) = \frac{B^{(q\omega)} z^2}{4} \quad (4.16)$$

The growth of the harmonic wave is compared in figure 4.1.a for both $\Delta k \neq 0$ and $\Delta k = 0$ (dashed and thick-solid curves respectively - the other curves will be explained later). If $\Delta k = 0$ there is no upper bound to the harmonic intensity (aside from the finite energy of the driving wave, which has been ignored in this derivation). In contrast, for $\Delta k \neq 0$, the harmonic intensity is limited to $B^{(q\omega)}/\Delta k^2$, varying between zero and this ceiling. In this situation the dephasing length can be defined as $L_d = \pi/\Delta k$. L_d can be thought of as the propagation distance necessary for a π phase difference to accumulate between the growing harmonic wave and the local phase of harmonic generation.

4.2 Nonuniform dispersion

The model of the previous section can be generalised to include z -dependence in the dispersions $k(\omega)$ and $k(q\omega)$. Such dependencies will often be significant in realistic HHG experiments. Rather than starting with the plane driving wave of equation 4.1, the WKB solution of the wave equation is used:

$$E^{(\omega)}(z, t) \approx \frac{E_0^{(\omega)}}{2\sqrt{k(\omega, z)}} e^{i[\phi(z) - \omega t]} + \text{c.c.} \quad \text{where} \quad \phi(z) = \int_0^z k(\omega, z') dz' \quad (4.17)$$

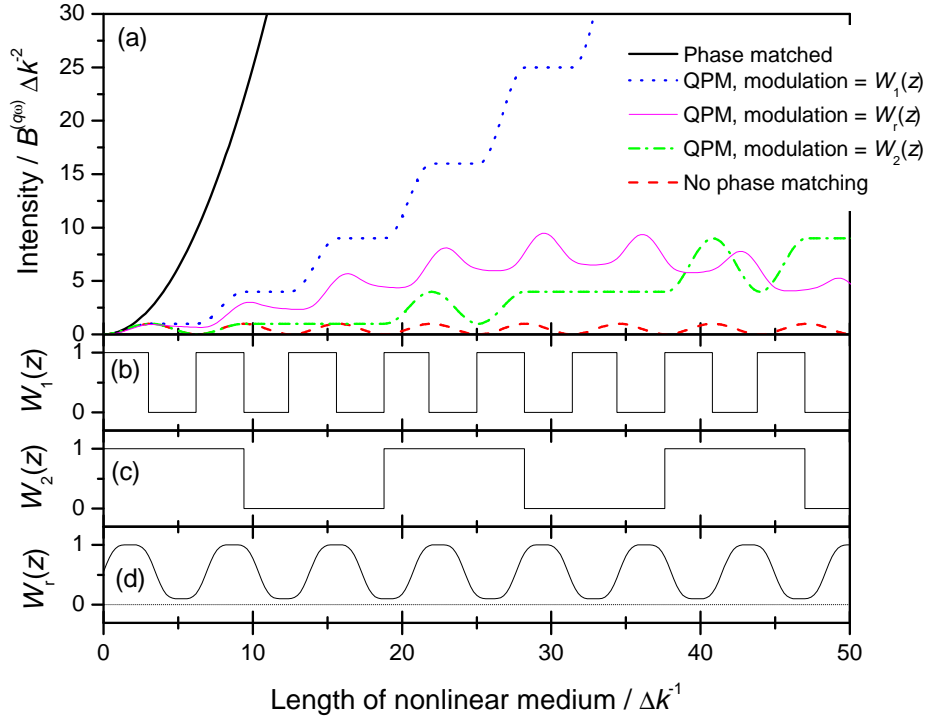


FIGURE 4.1: (a) Phase matching and QPM result in significantly greater harmonic intensity than non-phase-matched conditions. (b)-(d) show the modulation functions for the three QPM cases shown in (a).

and where the start of the integral $z = 0$ is somewhere before the nonlinear material begins. Since the variation in amplitude from $\sqrt{k(\omega, z)}$ in the denominator is small, this factor will be dropped. The time delay relation for the electric field becomes

$$E^{(\omega)}(z, t) = E^{(\omega)}(0, t - \frac{1}{\omega} \int_0^z k(\omega, z') dz') \quad (4.18)$$

As before, the oscillating polarisation at z will be delayed due to this effective time delay in E :

$$P_{\text{NL}}^{(q\omega)}(z, t) = \frac{P_{\text{NL},0}^{(q\omega)}}{2} e^{-i[q\omega t - \int_0^z k(q\omega, z') dz']} + \text{c.c.} \quad (4.19)$$

Again, this polarisation acts as the source term of the inhomogeneous wave equation 4.7. As a trial solution, rather than equation 4.8, this time the WKB solution is used:

$$E^{(q\omega)}(z, t) = \frac{\mathcal{E}^{(q\omega)}(z)}{2} e^{-i[q\omega t - \int_0^z k(q\omega, z') dz']} + \text{c.c.} \quad (4.20)$$

Again, a $\sqrt{k(q\omega, z)}$ factor has been dropped from the denominator. The next steps proceed as before. The final answer differs from the earlier expression 4.15 principally in that it involves integration over a z -dependent Δk :

$$I^{(q\omega)}(z) = \frac{B^{(q\omega)}}{4} \left| \int_0^z e^{i \int_0^{z'} \Delta k(z') dz'} dz' \right|^2 \quad (4.21)$$

where $\Delta k(z') = qk(\omega, z') - k(q\omega, z')$.

4.3 Sources of dispersion

Let us now find Δk for the q -th harmonic of a laser with fundamental vacuum wavelength λ_0 . There are several sources of dispersion in HHG experiments to include in Δk . One source, seen in Chapter 2, is the response of free electrons:

$$\eta_e = \sqrt{1 - \left(\frac{\omega_p}{\omega}\right)^2} \quad (4.22)$$

Rearranging this expression to find k for the q -th harmonic,

$$k = \frac{\omega}{c} \sqrt{1 - \left(\frac{\omega_p}{\omega}\right)^2} \approx \frac{\omega}{c} \left(1 - \frac{\omega_p^2}{2\omega^2}\right) = \frac{2\pi q}{\lambda_0} - \frac{n_e r_e \lambda_0}{q} \quad (4.23)$$

where $r_e = e^2/4\pi\epsilon_0 m_e c^2$ is the classical electron radius. In the second step the plasma frequency has been taken to be much below the frequency of the IR or XUV light. For even the highest possible plasma frequencies, say that of $n_e = 10\%$ of atmospheric density (at 298 K), $\omega = 2\pi c q/\lambda_0 \approx 26q \omega_p$, so this approximation is sound.

Another source of dispersion is the neutral or ionised atoms used for the nonlinear medium. For ionisation fractions of more than a few percent, the free electron dispersion will dominate over this second dispersive effect. This fact, plus the difficulty in determining the index of refraction of ions, means that this ionic index of refraction is never considered. For neutrals, the index of refraction η is most commonly tabulated at the density n_{atm} corresponding to 1 atm at 298 K. At this density, $\eta - 1$ is on the order of $+10^{-4}$ for $q = 1$ (the fundamental wavelength)

[55], and on the order of -10^{-5} to -10^{-4} for the $q > 20$ harmonics [56]. The tabulated index of refraction η_{atm} corresponds to a polarisability $\alpha = \epsilon_0(\eta_{\text{atm}}^2 - 1)$. As the polarisability is linearly proportional to the gas density, then at another density n the polarisability will be

$$\alpha = \epsilon_0(\eta_{\text{atm}}^2 - 1) \frac{n}{n_{\text{atm}}} \quad (4.24)$$

and the k for arbitrary density can now be computed:

$$k = \frac{2\pi q \eta}{\lambda_0} = \frac{2\pi q}{\lambda_0} \sqrt{1 + \frac{\alpha}{\epsilon_0}} = \frac{2\pi q}{\lambda_0} \sqrt{1 + (\eta_{\text{atm}}^2 - 1) \frac{n}{n_{\text{atm}}}} \approx \frac{2\pi q}{\lambda_0} + \frac{2\pi q n}{\lambda_0 n_{\text{atm}}} (\eta_{\text{atm}}^2 - 1) \quad (4.25)$$

where in the last step the approximation $|\eta_{\text{atm}}^2 - 1| \ll 1$ is applied.

Another significant source of dispersion appears in those experiments that use a gas jet or cell rather than a waveguide. Dispersion then appears because the focusing laser beam is not a plane wave. The electric field of a focused Gaussian beam, propagating in the z direction in cylindrical coordinates, is:

$$E(\rho, \theta, z, t) = \quad (4.26)$$

$$A \times \underbrace{\exp(i\omega[z/c - t])}_{\text{propagating plane wave}} \times \underbrace{\frac{1}{\sqrt{1 + z^2/b^2}}}_{\text{intensity variation with } z} \times \underbrace{\exp\left(-\frac{\rho^2}{w_0^2(1 + z^2/b^2)}\right)}_{\text{intensity variation with } \rho} \dots$$

$$\times \underbrace{\exp\left(\frac{i\omega\rho^2}{2cz(1 + b^2/z^2)}\right)}_{\text{curvature of wavefronts}} \times \underbrace{\exp(-i \arctan(z/b))}_{\text{Gouy phase}}$$

where w_0 is the $1/e^2$ intensity radius at the beam waist, and $b = \omega w_0^2/2c$ is the Rayleigh range. The Gouy term contributes an additional z -dependent phase that makes the propagation constant differ from its vacuum value. Near the focus, the Gouy term is approximately $e^{-iz/b}$. Comparing this term with the plane wave term in equation 4.26, it can be seen that near the focus the wave is approximately

$$E(z, t) \approx \exp\left[i\left(\left[\frac{\omega}{c} - \frac{1}{b}\right]z - \omega t\right)\right] \quad (4.27)$$

Hence, the apparent propagation constant is

$$k = \frac{\omega}{c} - \frac{1}{b} = \frac{2\pi q}{\lambda_0} - \frac{\lambda_0}{\pi q w_0^2}. \quad (4.28)$$

Next, for HHG experiments in which a waveguide is used, it was noted in Chapter 3 that the waveguide introduces dispersion:

$$\text{Re}(k) = \frac{\omega}{c} \sqrt{1 - \left(\frac{u_{j,p} c}{\omega a}\right)^2} = \frac{2\pi q}{\lambda_0} \sqrt{1 - \left(\frac{u_{j,p} \lambda_0}{2\pi q a}\right)^2} \approx \frac{2\pi q}{\lambda_0} - \frac{u_{j,p}^2 \lambda_0}{4\pi a^2 q} \quad (4.29)$$

The approximation in the last step is sound since typically $a > 60 \lambda_0$ for any realistic experiment.

Finally, intensity-dependent phase $\phi(I)$ (equation 2.4) is known to have a significant effect on the phase matching of HHG, at least in experiments with a focused rather than waveguide geometry¹ [26, 27]. As figure 2.4 showed, for intensity variations that are modest on the scale of HHG experiments, intensity-dependent phase can vary by many tens of radians. Since the intensity will vary with position, $\nabla\phi \neq 0$, and so just as in the above analysis of Gouy shift, the apparent wave vector is altered. The spatial variation of intensity-dependent phase, free-electron dispersion, and Gouy phase mean that phase matching may exist in some regions but not others. For the rest of this section the discussion will be restricted to phase matching strictly at the focus. $\nabla I = 0$ here, so intensity-dependent phase will be ignored. However, it should be remembered that the situation could be markedly different at other nearby locations.

Each of the four remaining dispersive effects (free electrons, neutrals, Gouy, and waveguide) causes the propagation constant k to deviate slightly from its vacuum plane-wave value $2\pi q/\lambda_0$. To combine the various effects, it turns out that the deviations can be added. Doing so is valid, we shall see, because of the fortuitous circumstance that the corrections are all small. Consider for a moment the waveguide case (i.e., no Gouy shift), and let $s = 1/a$ be the reciprocal of the waveguide radius. The general expression for k will show a dependence on all three dispersive effects, e.g., $k(n_e, n, s)$. A Taylor expansion of k about $n_e = n = s = 0$ gives:

$$k(n_e, n, s) \approx k(0, 0, 0) + n_e \left(\frac{\partial k}{\partial n_e}\right)_{n,s} + n \left(\frac{\partial k}{\partial n}\right)_{n_e,s} + s \left(\frac{\partial k}{\partial s}\right)_{n_e,n} + \dots \quad (4.30)$$

¹There may also be effects for waveguide experiments, as will be shown in section 8.6.1.

Looking back at the free electron dispersion equation (4.23), it is none other than the $n = s = 0$ case of the general Taylor expansion, so

$$\left(\frac{\partial k}{\partial n_e} \right)_{n,s} = \frac{r_e \lambda_0}{q} \quad (4.31)$$

Similarly, equations 4.25 and 4.29 give us the other two partial derivatives. For each of the three dispersion effects we have already argued that a first-order Taylor expansion is a good approximation. Plugging these partial derivatives into equation 4.30, then, gives us a good approximation for the overall propagation constant:

$$k_{\text{waveguide}} = \underbrace{\frac{2\pi q}{\lambda_0}}_{\text{vacuum}} - \underbrace{\frac{n_e r_e \lambda_0}{q}}_{\substack{\text{free} \\ \text{electrons}}} + \underbrace{\frac{2\pi q n}{\lambda_0 n_{\text{atm}}} [\eta_{\text{atm}}(\lambda_0/q) - 1]}_{\text{neutrals}} - \underbrace{\frac{u_{j,p}^2 \lambda_0}{4\pi a^2 q}}_{\text{waveguide}} \quad (4.32)$$

For a focused beam, a similar analysis shows:

$$k_{\text{focus}} = \underbrace{\frac{2\pi q}{\lambda_0}}_{\text{vacuum}} - \underbrace{\frac{n_e r_e \lambda_0}{q}}_{\substack{\text{free} \\ \text{electrons}}} + \underbrace{\frac{2\pi q n}{\lambda_0 n_{\text{atm}}} [\eta_{\text{atm}}(\lambda_0/q) - 1]}_{\text{neutrals}} - \underbrace{\frac{\lambda_0}{\pi q w_0^2}}_{\text{Gouy}} \quad (4.33)$$

It is now possible to compute $\Delta k = qk(\omega) - k(q\omega)$. In $k(q\omega)$, the free-electron and waveguide terms can be discarded since they scale as q^{-1} , and so are q^2 times smaller than the equivalent terms for the fundamental wavelength:

$$\Delta k_{\text{waveguide}} = \underbrace{-\frac{n_e r_e \lambda_0 q}{q}}_{\substack{\text{free} \\ \text{electrons}}} + \underbrace{\frac{2\pi q n}{\lambda_0 n_{\text{atm}}} [\eta_{\text{atm}}(\lambda_0) - \eta_{\text{atm}}(\lambda_0/q)]}_{\text{neutrals}} - \underbrace{\frac{u_{j,p}^2 \lambda_0 q}{4\pi a^2}}_{\text{waveguide}} \quad (4.34)$$

In Δk_{focus} we can ignore the term corresponding to the Gouy shift of the harmonic, based on the following reasoning. The intensity of harmonic q can be modeled as being proportional to the fundamental intensity raised to some power p , where $5 \leq p \leq 13$ [57]. From this relation, it follows that the spot size for the harmonic $w_0(\lambda/q)$ is $\sqrt{p} w_0(\lambda)$. Thus, the Gouy term for the harmonic is p/q^2 times the Gouy term of the fundamental, and this ratio is small for the

harmonics of interest in this thesis. Thus,

$$\Delta k_{\text{focus}} = \underbrace{-n_e r_e \lambda_0 q}_{\text{free electrons}} + \underbrace{\frac{2\pi q n}{\lambda_0 n_{\text{atm}}} [\eta_{\text{atm}}(\lambda_0) - \eta_{\text{atm}}(\lambda_0/q)]}_{\text{neutrals}} - \underbrace{\frac{\lambda_0 q}{\pi [w_0(\lambda_0)]^2}}_{\text{Gouy}} \quad (4.35)$$

Note that in these last formulae for Δk_{focus} and $\Delta k_{\text{waveguide}}$, the various dispersive effects can be balanced against each other to achieve $\Delta k=0$.

It should not be forgotten that since intensity varies with time, the free electron dispersion and the intensity-dependent phase will do so as well. This improves the odds that phase matching will occur, since these sources of dispersion will sweep through a range of values. If phase matching occurs, it will likely not occur for much of the duration of the driving pulse; the length of the harmonic pulse may therefore be much shorter than the driver.

4.4 Phase matching of high harmonics: Previous work

Phase matching in the focused geometry has been discussed by several authors [58–62]. To produce higher harmonic orders, the higher intensities required result in more ionisation. This in turn increases the magnitude of the free electron term in equation 4.35. To balance this term with a larger term from neutral atoms, several experiments have arranged for the harmonics to lie near atomic resonances, where $|\eta - 1|$ is large [63] [64].

There are many advantages to using a waveguide. First, the interaction length is not limited to ~ 1 mm by diffraction or defocusing. Furthermore, the interaction conditions vary less with longitudinal position, so if phase matching conditions are good in one place, they are likely to be good over a large region.

Extensive experimental work on HHG in waveguides has been conducted by Margaret Murnane's groups at the University of Michigan and at JILA in Boulder, Colorado. The major results from this group for standard grazing-incidence waveguides have been reported in Rundquist *et al* [65] and Durfee *et al* [57]. For the work reported in these papers, 26 fs pulses

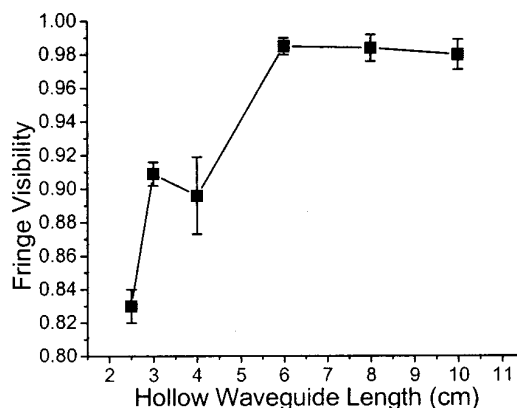


FIGURE 4.2: The Murnane group found that high harmonics possessed greater spatial coherence when the driver laser was guided over many Rayleigh lengths. Figure from [67].

from a Ti:Sapphire laser were focused to a spot size of $50 \mu\text{m}$, giving a peak intensity of $2 \times 10^{14} \text{ W/cm}^2$ at the entrance of $150 \mu\text{m}$ -diameter capillaries. For the 29th and 31st harmonics of the 800nm driver, energies of 0.2 nJ per harmonic peak per pulse were produced, a conversion efficiency of 10^{-5} to 10^{-6} .

It was found that the UV light produced by HHG has improved spatial coherence when produced in a waveguide compared with HHG produced in a gas jet. Spatial coherence experiments were conducted by producing holographic effects [66] and by examining interference fringes from a pinhole pair [67]. Figure 4.2 shows how the fringe visibility of the two-pinhole interference pattern, which is directly related to spatial coherence, approaches one (i.e., perfect coherence) for capillaries of 5 cm or longer.

In a theoretical paper, Milchberg *et al* have discussed phase-matching HHG in gradient-index plasma waveguides. As with the grazing-incidence waveguide modes, the modes in a gradient-index guide possess different phase velocities. Thus, phase matching can be achieved if the fundamental is in a different mode than the harmonics [68]. However, the overlap between the modes is poor, so little harmonic energy goes into the desired mode.

4.5 Limits to phase matching

If phase matching were not a consideration, harmonics would ideally be made with a high intensity driver (to create very high harmonic orders and to increase efficiency) and made in a

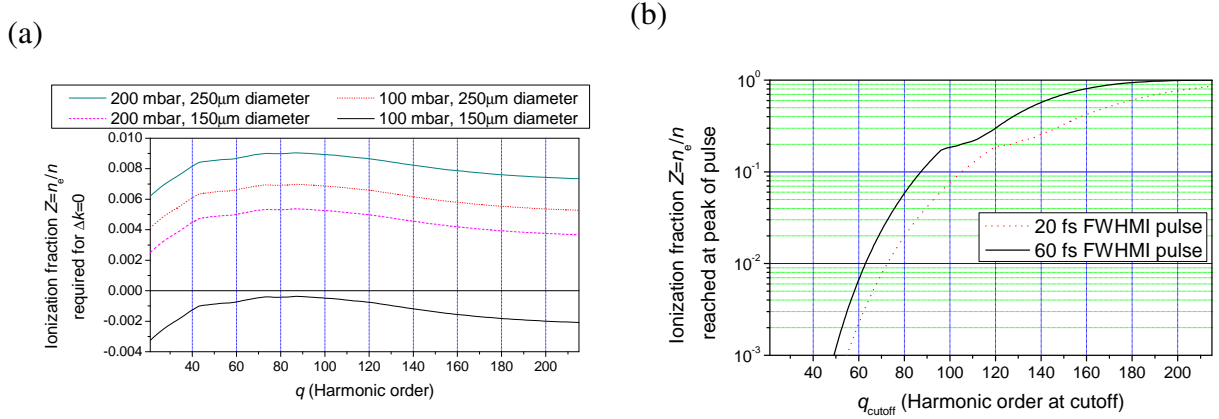


FIGURE 4.3: (a) Calculation of the ionisation fraction required for phase matching various harmonic orders of Ne. Results are shown for two gas pressures and two capillary diameters. The negative values for the lowest trace indicate that it cannot be phase matched. (b) The ADK ionisation rates are computed for pulses of different peak intensities, and the ionisation fraction produced is plotted against the cutoff harmonic order. This plot highlights the advantage of minimising pulse duration: for a given ionisation fraction at the pulse peak, shorter pulses allow for higher intensities, so the harmonic cutoff can be extended to shorter wavelengths.

capillary (to increase the interaction length). Unfortunately, phase matching is not possible in these conditions. With high intensity comes high ionisation, and the ionisation term in equation 4.34 overwhelms the waveguide and neutral terms. Figure 4.3.a shows the ionisation fraction required to phase match various harmonic orders in Ne. Several realistic values for pressure and capillary radius are used. It turns out that at the intensities required to produce harmonics of order >60 , however, the ionisation fraction is much higher than this, as shown in part (b) of the figure. Consequently, for efficient generation of SXR harmonics, true phase matching is not an option.

4.6 Harmonic peak splitting revisited

In section 2.4.3 one mechanism was described which can give rise to split harmonic spectral peaks. Several other such processes are now described which depend on the concepts introduced in this chapter.

Salières *et al* observe harmonic peak splitting in 2D simulations that ignore ionisation but do consider intensity-dependent phase [26]. Due to the spatial variation in Gouy and intensity-

dependent phase, $|\Delta k|$ is minimised in several non-connected regions near the focus [27]. Most of the overall harmonic output therefore comes from these areas. As different locations experience different intensities, the harmonics radiated from the different low- $|\Delta k|$ regions will be nonadiabatically blueshifted by different amounts. Hence, the final spectrum shows split peaks. Salières *et al* only consider the spatial variation in nonadiabatic blueshift. However, there is also spatial variation in ionisation-blueshift, since this shift increases with the length of gas traversed by the driver. Salières-style peak splitting should therefore also be possible through the different ionisation-blueshift between isolated low- $|\Delta k|$ regions.

Yet another method by which harmonic spectral peaks may split has been given by Xu *et al* [43, 69, 70]. The model of these authors differs in many respects from that of Salières: it is only 1D and therefore it ignores intensity-dependent phase, but it does include ionisation. Since the degree of ionisation Z increases as the laser pulse passes through the medium, then for a given location, Δk decreases with time. For an interaction length L , the harmonic intensity at the end of this interaction length is given approximately by a modified version of equation 4.15:

$$I^{(q\omega)}(t) = B^{(q\omega)} \Delta k^{-2}(t) \sin^2\left(\frac{\Delta k(t)L}{2}\right) \quad (4.36)$$

where $\Delta k(t)$ is the phase mismatch seen if co-moving with the driving pulse. If $\Delta k(t)$ varies sufficiently in the time over which the harmonic is generated, then $I^{(q\omega)}(t)$ will pass through 0 when $\Delta k = \pm 2\pi/L$. At this moment the dephasing length is such that all harmonic radiation perfectly cancels through destructive interference. Over the duration of the pulse, both ionisation and nonadiabatic blueshifting will cause the harmonic frequency to vary. Consequently, if $I^{(q\omega)}$ decreases at a certain *time*, then the spectrum will decrease at the associated *wavelength*, and this wavelength will be somewhere in the middle of the harmonic spectral peak.

For the Salières and Xu mechanisms, as with the microscopic peak-splitting mechanism discussed in section 2.4.3, the splitting is less pronounced for harmonics in the cutoff. These harmonics are made only in a single small region, not multiple distinct regions as required by the Salières scheme. Also, Xu-style splitting cannot occur for cutoff harmonics because they are made only for a brief subset of the pulse duration, too short for Δk to vary significantly during their emission.

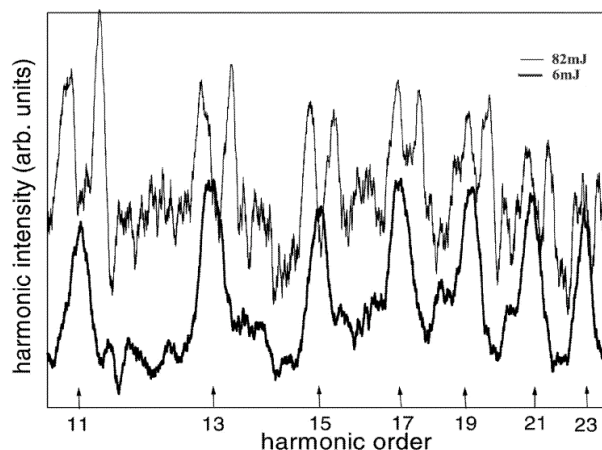


FIGURE 4.4: Experimental data from Xu *et al* showing the splitting of harmonic peaks above a threshold laser energy. Figure from [70].

Interestingly, although harmonic peak splitting is predicted numerically through the several mechanisms described in this thesis, almost no published *experimental* HHG spectra show splitting. Xu *et al* provide one experimental spectrum with split peaks, presuming without justification that the splitting is due to the mechanism they suggest and not to one of the other possibilities. This spectrum was obtained using a 46 fs, 790 nm laser in a 0.5 mm jet of 71 mbar Ar. Only one other paper with split experimental harmonic spectra was found in an extensive literature review: reference [71] by Sekikawa *et al*. In this paper, split peaks were seen using a 24 fs, 803 nm laser in a 7 mm gas cell of 23 mbar Ar. One possible explanation for the paucity of split-peak observations is that the laser energy employed in HHG experiments is typically less than 20-30 mJ, the values seen by both Sekikawa and Xu as the experimental threshold for splitting.

4.7 Quasi phase matching

An alternative to true phase matching is the suppression of harmonic generation in those regions that contribute negatively rather than positively to the harmonic wave growth. This scheme is known as quasi phase matching (QPM). In QPM, the efficiency or phase of harmonic generation or the density of the medium is somehow modulated by a periodic function. Ideally, this

function has a form resembling

$$W_j(z) = \begin{cases} 1 & \text{if } \sin\left(\frac{z\Delta k}{2j-1}\right) > 0 \\ 0 & \text{otherwise} \end{cases} \quad (4.37)$$

where $j \in \{1, 2, 3, \dots\}$. Consider the case in which the efficiency of HHG is proportional to $W_j(z)$. In this picture, harmonic generation is permitted for an odd-integer number of dephasing lengths, then suppressed for such a distance, and the pattern is repeated. The square wave function $W_j(z)$ is plotted in figure 4.1 for $j = 1$ and $j = 2$. Harmonic wave growth is less rapid for higher j . The modulation function need not be perfect. The more realistic window function $W_r(z)$ shown in figure 4.1.d only varies from 1 to 0.1 and has a period that is 10% too long; it nonetheless results in many times the harmonic intensity of the non-phase-matched case.

QPM was proposed in 1962 [72], only a year after the first nonlinear optical effect was observed [73]. The experimental achievement of QPM occurred within months [74], in a study of second-harmonic generation. This first experiment used a stack of 250 μm -thick quartz plates in which one of the crystal axes alternated in direction by 180° . Consequently, the relative phase between the fundamental and the harmonics generated in any of the even crystal plates differed by π from that of the odd plates. Consequently, only constructive interference occurred. Many QPM experiments have since been performed with “periodically poled” ferromagnetic crystals, in which the light passes through a series of magnetic domains. The magnetisation vector alternates by 180° from one domain to the next, and a similar pattern of phase shifts results. Crystals of this sort for QPM have been created through several different methods [75, 76]. An $\omega \rightarrow 2\omega$ conversion efficiency of 42% was achieved with periodically poled crystals by the group of Fejer *et al* [77, 78]. Efficiencies of almost 60% were seen when the material was configured into a waveguide [79]. By using more complicated poling patterns, more than two frequencies can be phase-matched, so frequency mixing is possible [80, 81]. Still other methods of QPM have been reported as well [82–84]. All of the references above involve only low-order nonlinear phenomena; only recently has QPM been discussed in the context of HHG, where the radiation cannot pass through solid materials due to absorption.

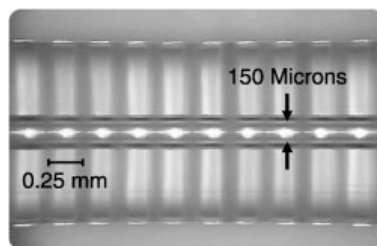


FIGURE 4.5: A patterned capillary used by Murnane *et al.* Figure from [8].

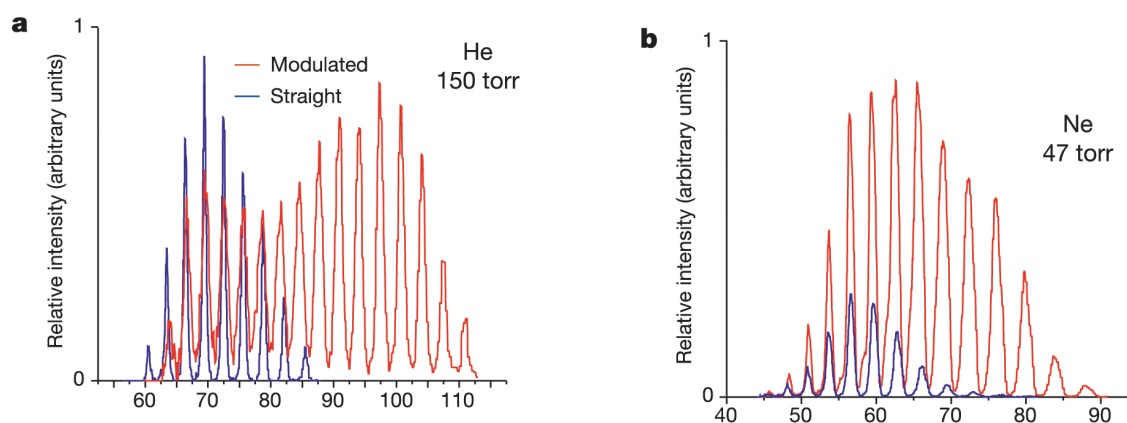


FIGURE 4.6: QPM results by Murnane *et al.* for modulated capillaries. Figure from [85].

4.8 QPM of high harmonics: Previous work

Shkolnikov *et al.* give a theoretical discussion of QPM for HHG, showing how the harmonic signal might increase if the gas density could be modulated by some unspecified mechanism [86]. To our knowledge, at this time there are no published reports of experimental QPM of HHG using density modulations.

One other QPM technique for HHG has been explored by the Murnane group [8, 85, 87]. The driving laser is guided through a hollow capillary with a periodically varying radius, as shown in figure 4.5. Consequently, the intensity is modulated with the same period. Since the Rayleigh length associated with the guided spot size (9 millimetres) is longer than the capillary modulations (0.25-1 mm), one might expect the amplitude of the intensity modulation ΔI to be less than $2\Delta r$, the ΔI predicted if the local intensity were proportional to the inverse-square of the local radius $r + \Delta r(z)$. Detailed simulations of the wave equation by the group suggest that in fact $\Delta I > 2\Delta r$; the authors of the paper do not explain the reason [87].

Experiments were also conducted, using glassblowing techniques to introduce ripples into

a standard straight glass fibre. The capillaries had an inner diameter of $150\ \mu\text{m}$, varying by $\pm 10\ \mu\text{m}$ with the modulation. The group experimented with different lengths of capillary (up to 2.5 cm) and different modulation periods (from 0.25 mm to 1.00 mm). The laser used was a Ti:Sapphire 760 nm, 2-5 kHz system with 1-3 mJ per pulse. Figure 4.6 shows some results from the experiments. For a given pressure and driver laser intensity, the total XUV flux is seen to be 2-5 times greater for a modulated capillary compared to a non-modulated capillary of otherwise identical dimensions. The enhancement of harmonics is most significant near the cutoff. Murnane and colleagues explain this by noting that small modulations in the intensity may have modest effects for the generation of plateau harmonics, but the effects are much larger for cutoff harmonics, since they are generated at intensity $I + \Delta I$ but not at $I - \Delta I$.

Higher harmonic orders are also seen in the modulated capillaries, than in straight capillaries, holding all other factors constant. Murnane and colleagues surmise that this extension in the observed cutoff does not indicate a rise in U_i or U_p , as equation 2.2 would suggest. Rather, it is thought that the highest harmonic orders are produced even in the non-modulated capillaries, but only at times when the ionisation is so great that phase matching is extremely poor, and so the harmonics are not detected.

Harmonics in the water window are seen when the modulated capillaries are used with neon as the target gas. The peak focusable spectral brightness within the water window is estimated to be 10^{20} in the units of figure 1.2.a.

CHAPTER 5

Theory of Quasi Phase Matching with Counter-Propagating Light

There are several processes by which counter-propagating light can modulate high harmonic generation. Although these processes diminish rather than increase the efficiency of harmonic generation locally, we have seen in chapter 4 that such extinction can be exploited to create enhancement. This chapter first describes the mechanisms by which counter-propagating light affects HHG. Then, since quasi phase matching requires an alternating series of extinction zones, two methods are discussed for making trains of pulses. Measurements of pulse trains created by these methods at Oxford and RAL will be reported in chapter 7.

5.1 HHG suppression

5.1.1 Parallel polarisations

First, consider the situation in which the counter-propagating light is linearly polarised along the same axis as the driving field. The electric field in the region where the two beams overlap is given by:

$$E(z, t) = \text{Re} \left[E_d e^{i(kz - \omega t)} + E_{cp} e^{i(-kz - \omega t)} \right] = \text{Re} \left[E_t(z) e^{i(kz - \omega t + \phi(z))} \right] \quad (5.1)$$

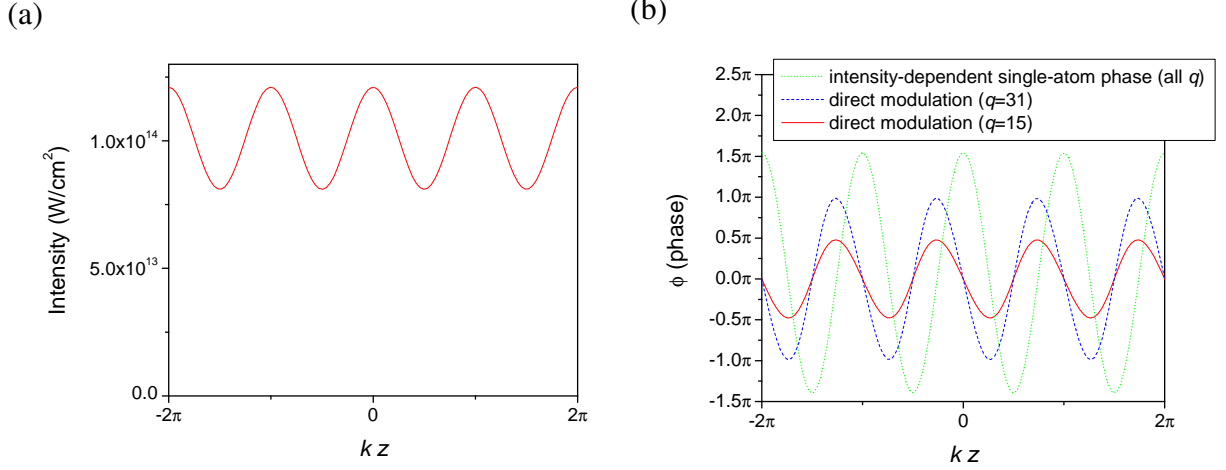


FIGURE 5.1: (a) Fundamental intensity and (b) harmonic phase shift variations that result when a 1×10^{14} W/cm² wave interacts with a counter-propagating wave of 1/100 the intensity.

where E_d is the electric field amplitude of the driving beam, E_{cp} is the amplitude of the counter-propagating beam, and

$$E_t(z) = E_d \sqrt{1 + \left(\frac{E_{cp}}{E_d}\right)^2 + 2\frac{E_{cp}}{E_d} \cos(2kz)} \quad (5.2)$$

$$\phi(z) = -\arctan\left(\frac{\frac{E_{cp}}{E_d} \sin(2kz)}{1 + \frac{E_{cp}}{E_d} \cos(2kz)}\right) \quad (5.3)$$

The variation in the intensity and phase shift is plotted in figure 5.1 for $E_{cp}/E_d = 0.1$, corresponding to an intensity ratio of 1:100. A shift in the phase of the fundamental by ϕ corresponds to a shift in the phase of the q th harmonic by $q\phi$. Hence, while the phase shift is a small fraction of π for the fundamental, it will be significant for harmonics of high enough order. For the intensity ratio in the figure, there is a phase variation of at least π for $q > 15$. Thus, harmonics from different points in space do not add in phase. The net emission of harmonics with $q > 15$ therefore is much reduced compared to the $E_{cp} = 0$ case.

One can estimate the intensity required in the counter-propagating beam to extinguish the harmonics of order q through this mechanism. From equation 5.3, the peak-to-peak phase variation caused by the counter-propagating beam is

$$\Delta\phi = 2 \arctan\left(\frac{E_{cp}/E_d}{\sqrt{1 - (E_{cp}/E_d)^2}}\right) \quad (5.4)$$

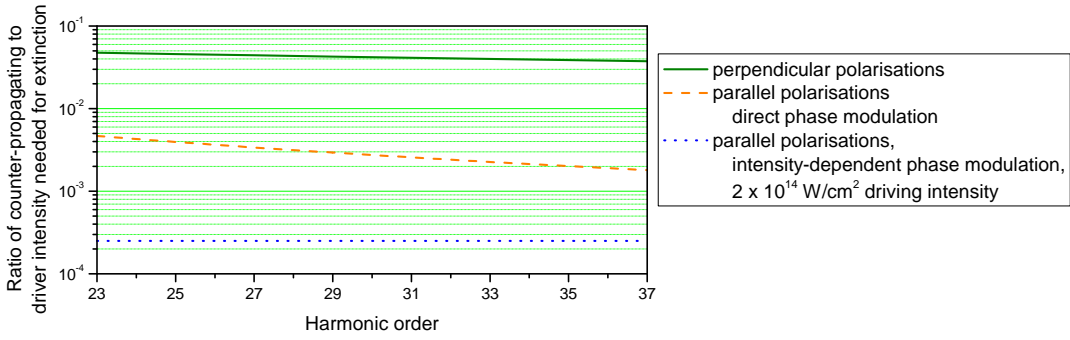


FIGURE 5.2: Comparison of the counter-propagating intensity needed for extinction by the two parallel polarisation mechanisms and that needed by the perpendicular polarisation method.

Harmonics of order q are extinguished when this phase variation is of order π/q . Rearranging this extinction condition in terms of the beam intensities,

$$\frac{I_{\text{cp}}}{I_{\text{d}}} = \left(\frac{E_{\text{cp}}}{E_{\text{d}}} \right)^2 = \left(\frac{\tan(\pi/2q)}{\sqrt{1 + \tan^2(\pi/2q)}} \right)^2 \quad (5.5)$$

Due to the intensity-dependent phase of harmonic emission (section 2.1.1), the harmonic phase is also modulated indirectly due to the intensity modulation. Peatross and colleagues do not quantitatively consider this effect. From equation 5.2 it can be derived that the peak-to-peak intensity variation due to the counter-propagating light is $4\sqrt{I_{\text{cp}}I_{\text{d}}}$. Combining this result with equation 2.4, the peak-to-peak phase variation is approximately

$$|\Delta\phi| \approx \frac{4\pi e^2}{\epsilon_0 c m_e \hbar \omega^3} \sqrt{I_{\text{cp}}I_{\text{d}}} \quad (5.6)$$

Therefore, a phase variation of π or more arises when

$$I_{\text{d}} I_{\text{cp}} > 1 \times 10^{25} \text{ (W/cm}^2\text{)}^2. \quad (5.7)$$

At 1×10^{14} W/cm², a typical low driving intensity for HHG, as little as 0.1% of the driving intensity is needed in the counter-propagating beam for $\Delta\phi \geq \pi$. Thus, intensity-dependent phase is likely to contribute significantly to harmonic suppression.

Figure 5.2 compares the required counter-propagating intensity for extinction for the two

mechanisms of phase modulation. The intensity-dependent phase mechanism, unlike the direct modulation, depends on the driving intensity, so a realistic experimental value of 2×10^{14} W/cm² is chosen. It appears from the figure that the intensity-dependent phase should be the dominant mechanism.

The above analysis has so far considered the interaction of two CW plane waves. However, one might expect the required I_{cp} to differ in a real experiment where the intensities vary with time and position. The applicability of the estimates above will likely differ for cutoff and plateau harmonics. Cutoff harmonics are generated only over a very small region of time and space – when the driver pulse peak passes through the focus. As the driver and counter-propagating intensities will not vary significantly over this small space-time volume, the CW plane-wave models above will not be unreasonable. Plateau harmonics, however, are generated over a range of intensities. The overlap between driver and counter-propagating pulses will be suboptimal in some harmonic-generating regions. Therefore, equations 5.5 and 5.7 probably underestimate the counter-propagating pulse intensity required to extinguish plateau harmonics.

5.1.2 Previous experiments

A group at Brigham Young University under Justin Peatross has explored the use of parallel-polarised counter-propagating light to control harmonic generation [88–93]. Figure 5.3 shows some of their principal results.

Extinction of HHG was demonstrated using a counter-propagating pulse (CPP) whose length, about 0.6 mm, was roughly twice the length of interaction with the gas. Figure 5.3.A shows the intensity of the 23rd harmonic as a function of the delay between the CPP and the main pulse. For a delay of zero, the main pulse interfered with the CPP for most of the interaction length. The HHG intensity was reduced by about two orders of magnitude compared with the case of no CPP. The group also demonstrated an enhancement of harmonic output. To do so, the gas interaction length was increased to 1 mm. The Gouy phase shift of the driver over this region times q was $\approx 3\pi$. If ionisation was low, as Peatross and colleagues believed it to be, then the interaction length was about three dephasing lengths. Peatross *et al* surmise that HHG in the central segment of these three was suppressed, and the first and third dephasing lengths con-

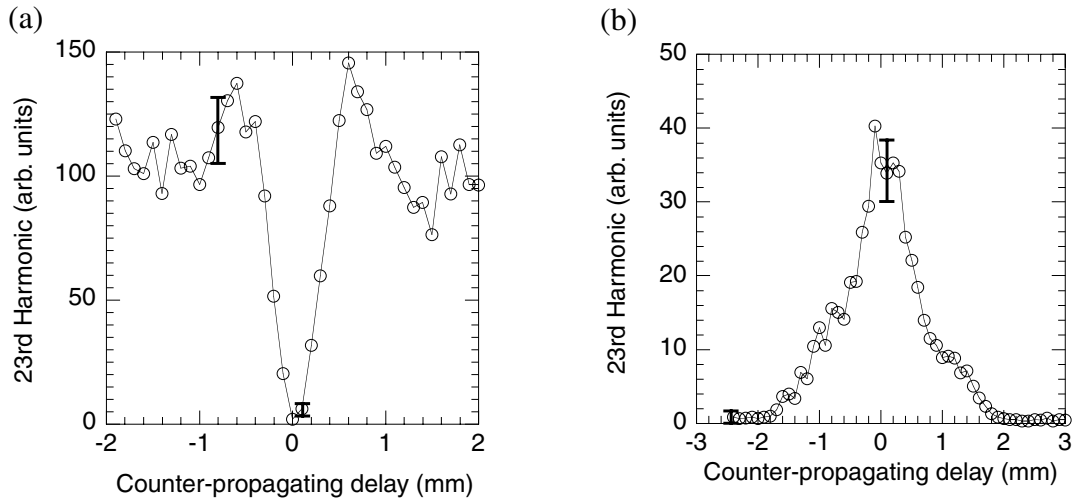


FIGURE 5.3: (a) Extinction of the 23rd harmonic in argon using the parallel-polarisation method. (b) Enhancement of the same harmonic in for a different position of the gas jet. Figures taken from Voronov *et al.*[88]

structively interfered. This enhancement, shown in figure 5.3.B, was achieved using the same 0.6 mm CPP.

5.1.3 Perpendicular polarisations

Extinction of HHG should also be possible using a counter-propagating beam whose polarisation is linear and *perpendicular* to that of the driver beam. Although Peatross and colleagues never mention this arrangement, it has one principal advantage over the use of parallel polarisations. With perpendicular polarisations, a polariser can be used to prevent the beams from propagating back into the laser after the crossing at the target. Light entering the laser in this manner could potentially damage the system. With a gas jet or gas cell the problem is not major, for the beams can be angled slightly off from each other. Peatross *et al* carried out experiments with both a co-axial counter-propagating beam and also with one that was 2° off-axis, finding that the latter was equally effective as the former [91]. However, it would be desirable to guide both beams in a waveguide to extend the interaction length. To ensure good guiding in this case, the beams would have to be entirely co-axial, and so without extra measures each beam would propagate back into the laser. Therefore, extinction by perpendicular polarisations would seem eventually preferable.

The physical mechanism for extinction in the perpendicular polarisation scheme is funda-

mentally different from that of the parallel polarisation case. In the perpendicular polarisation method, the counter-propagating beam gives rise to a varying ellipticity, and as we shall see, HHG efficiency drops off sharply with ellipticity.

First, to see in detail how the counter-propagating beam gives rise to ellipticity, consider again the case of colliding CW plane waves. The total electric field is the sum of the fields from each beam:

$$\mathbf{E}(z,t) = \text{Re} \left\{ E_d \exp(i[kz - \omega t]) \begin{pmatrix} 1 \\ 0 \end{pmatrix} + r E_d \exp(i[-kz - \omega t]) \begin{pmatrix} 0 \\ 1 \end{pmatrix} \right\} \quad (5.8)$$

where $r = E_{cp}/E_d$ is the ratio of the counter-propagating electric field amplitude to that of the driver, and the two-component vectors represent the 2D space of possible electric field directions in the transverse plane. It can be shown by construction that any two-component complex vector $\begin{pmatrix} a \\ b \end{pmatrix}$ can be represented in the form

$$e^{i\phi} \left[\begin{pmatrix} u \\ v \end{pmatrix} + i\varepsilon \begin{pmatrix} v \\ -u \end{pmatrix} \right] \quad (5.9)$$

where u, v, ε , and ϕ are real quantities¹. Thus, for each value of z , values $(u, v, \varepsilon, \phi)$ can be found to put $\mathbf{E}(z,t)$ into a form resembling the one above:

$$\mathbf{E}(z,t) = \text{Re} \left\{ E_d e^{-i\omega t} e^{i\phi(z)} \left[\begin{pmatrix} u(z) \\ v(z) \end{pmatrix} + i\varepsilon(z) \begin{pmatrix} v(z) \\ -u(z) \end{pmatrix} \right] \right\} \quad (5.10)$$

In this representation, it can be seen that the electric field will trace out an ellipse with time, where the ellipse may be different for different z . The major and minor axes of the ellipse are given by $\begin{pmatrix} u(z) \\ v(z) \end{pmatrix}$ and $\begin{pmatrix} v(z) \\ -u(z) \end{pmatrix}$ (not necessarily in that order). $\varepsilon(z)$ is the eccentricity (or its reciprocal), where ellipticity is defined as the ratio of the peak field along the minor axis to the peak field along the major axis. Setting the $\mathbf{E}(z,t)$ of equation 5.8 equal to that of equation 5.10, this system of four equations (two complex components) and four unknowns (u, v, ε , and ϕ) can

¹In other words, real orthogonal basis vectors can be found with a special property: that the projections p_1 and p_2 of the original vector onto these basis vectors differ in phase by $\pi/2$: $p_2 = i\varepsilon p_1$.

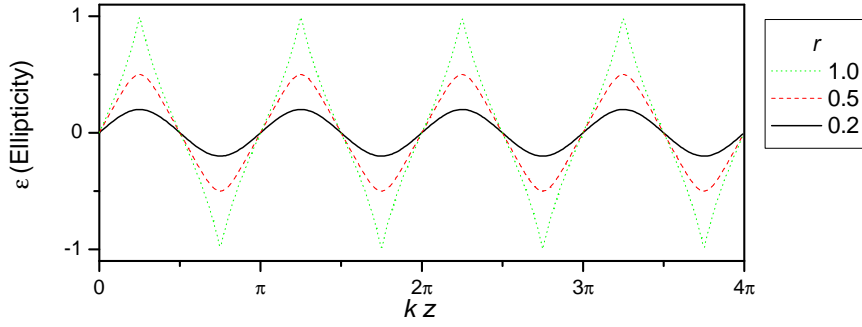


FIGURE 5.4: Ellipticity as a function of z for a perpendicularly polarised counter-propagating beam.

be solved² for ε :

$$\varepsilon(z) = \frac{\sqrt{1+r^4+2r^2\cos(4kz)}}{2r\sin(2kz)} \approx r\sin(2kz) \quad (5.11)$$

where the last step is valid if $|r| \ll 1$. Several possible $\varepsilon(z)$ functions are plotted in figure 5.4. A counter-propagating beam of perpendicular polarisation will thus cause there to be a position-dependent ellipticity. For $r \neq 0$, the polarisation is only linear at the discrete set of points $z = n\pi/2k$ for $n \in \mathbb{Z}$.

A counter-propagating and perpendicularly polarised beam can be used to extinguish harmonic generation, then, since the efficiency of HHG drops off sharply with eccentricity. This dependence can be understood in terms of the quasi-classical three-step model: for an elliptically polarised electric field, the trajectories of the electrons after ionisation in general do not return to the parent ion. Recombination is therefore precluded, and so harmonic generation is as well. For electrons which ionise at the phase required for maximum return energy ($> 3U_p$), the quasi-classical model shows the electrons will miss the ion [94] by roughly $5.7\varepsilon eE_0/m_e\omega^2$. For a driving intensity of $2 \times 10^{14} \text{ W/cm}^2$, then, the electron will miss the parent ion by at least the Bohr radius when $\varepsilon > 0.008$. The strong dependence of HHG on ellipticity is confirmed by more sophisticated theoretical models [24, 95] and many experiments [94, 96–101]. One group has already exploited the extinction effect of ellipticity, using time-varying ellipticity in a driving pulse to gate harmonic generation in time, shortening a train of XUV pulses to a single

²There are actually multiple ways to represent $E(z,t)$ in the form 5.9, but they are all physically equivalent. For example, given one representation, another can be obtained by swapping the axes of the ellipse $\begin{pmatrix} u \\ v \end{pmatrix} \rightarrow \begin{pmatrix} v \\ -u \end{pmatrix}$ and inverting the the eccentricity $\varepsilon \rightarrow 1/\varepsilon$.

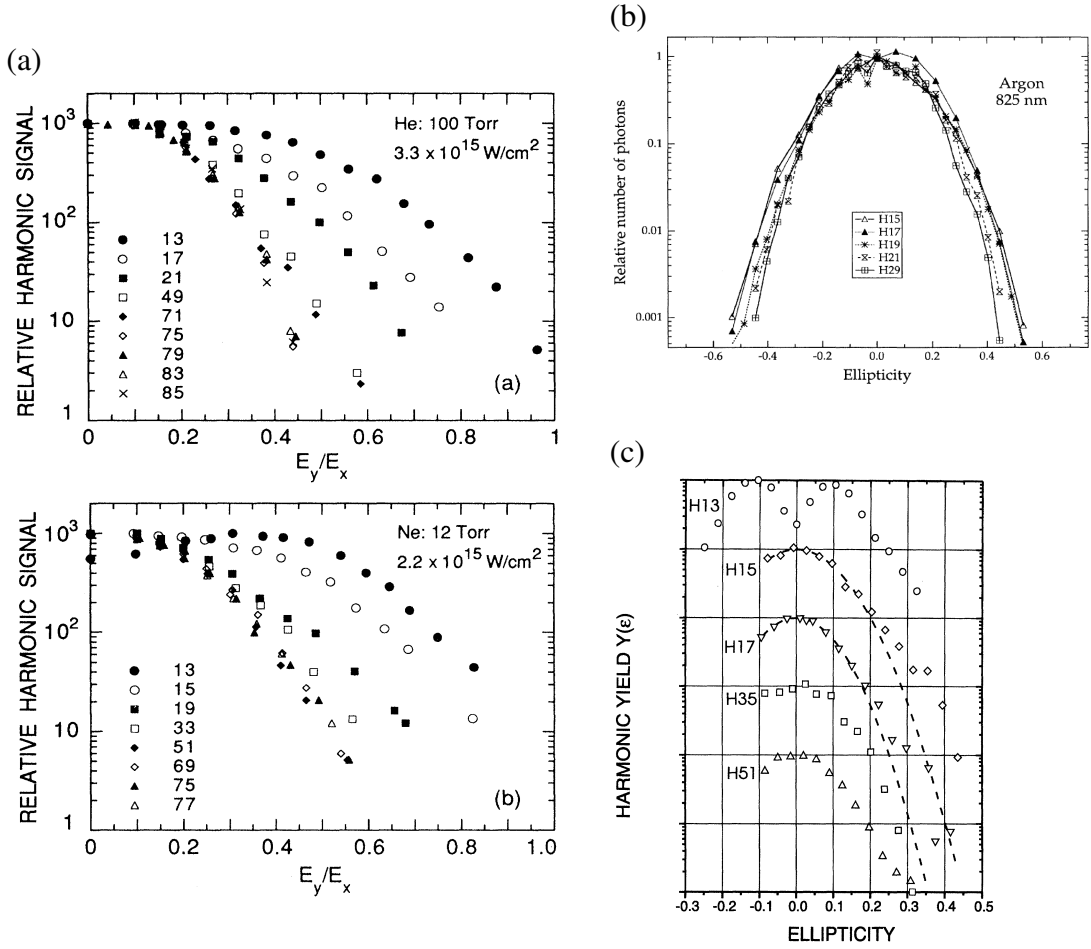


FIGURE 5.5: Effect of ellipticity on harmonic generation in argon. (a) Figure taken from Miyazaki *et al.* [99]. (b) Figure from Budil *et al.*[96]. (c) Figure from Burnett *et al.* [98].

pulse [102].

Figure 5.5 shows experimental results from three groups. All are consistent with the rule

$$I_q(\epsilon) = I_q(0)e^{-A(q)\epsilon^2} \quad (5.12)$$

The fit parameter $A(q)$ is seen to increase weakly with q .

These experimental results for single-beam HHG efficiency can be used to predict the efficacy of extinction using a perpendicularly polarised counter-propagating beam. To do so, $A(q)$ is first extracted from the experimental single-beam results. Figure 5.5.b suggests $A(21) \approx 32$ and $A(29) \approx 37$. Most experimental results in this thesis are for $q=23$ through 37, so a linear extrapolation is made to find A_q for $q > 29$. The precise values for $A(q)$ obtained in this manner are certainly suspect, but they at least provide a sense for the variation with q which can

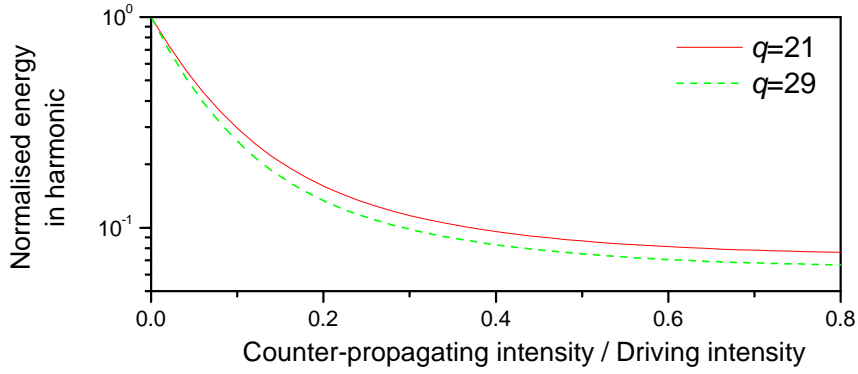


FIGURE 5.6: Suppression of harmonic signal due to counter-propagating and perpendicularly polarised light. The curves are calculated from equation 5.14 using empirical A_q values for argon.

be expected. Secondly, it must be taken into account that the ellipticity varies with z . At any particular z , the electric field contribution to the total output will be reduced according to the ellipticity at that location:

$$\frac{E_{q,\text{cp}}(z)}{E_{q,\text{no cp}}(z)} = \sqrt{\exp[-A(q)\varepsilon(z)^2]} = \exp\left(-\frac{A(q)\varepsilon(z)^2}{2}\right) \quad (5.13)$$

where $\varepsilon(z)$ is given by equation 5.11. An average is now taken over the relevant period ($\lambda/4$), and the result is squared to convert fields to intensities:

$$\frac{I_{q,\text{cp}}}{I_{q,\text{no cp}}} = \left[\frac{4}{\lambda} \int_0^{\lambda/4} \exp\left(-\frac{A(q)\varepsilon(z)^2}{2}\right) dz \right]^2 \quad (5.14)$$

The integral can be carried out analytically if $r \ll 1$ or numerically if $r \gtrsim 1$. Figure 5.6 plots the resulting function, showing how the harmonic signal may be expected to vary with the counter-propagating intensity.

The counter-propagating intensity required for half-extinction of various harmonic orders is plotted in figure 5.2, which also shows that a higher counter-propagating intensity is likely to be necessary for the perpendicular polarisation method than for the parallel polarisation scheme. The indirect-parallel effect is independent of q , while both the direct-parallel and perpendicular effects require less intensity for higher orders. This dependence is stronger for the parallel polarisation method. For all three mechanisms, the estimates apply best for cutoff harmonics. As

discussed on page 48, more counter-propagating intensity is likely to be necessary for harmonics in the plateau.

5.2 Methods for creating pulse trains

Peatross *et al* wrote back in 2001 that the next logical step in their work was to attempt quasi phase matching with a train of pulses [88]. However, their subsequent papers have not reported any results from such an experiment. We hoped to succeed in taking this next step. Peatross does not discuss possible schemes for creating a train of pulses, though he has apparently succeeded: in a 2004 paper he reports the use of a 10 ps counter-propagating pulse “consisting of five closely spaced chirped 1-2 ps pulses” [92]. We have explored two possible schemes for making trains of closely spaced pulses, shown in figure 5.7, which are likely different from his method.

5.2.1 1-crystal method

One scheme that was considered is shown in figure 5.7.a. A plane polarised and stretched pulse propagates through a thick birefringent crystal at 45° to the crystal’s ordinary and extraordinary axes. Due to the pulse’s chirp, the effect of the crystal will vary from one part of the pulse to another. The crystal will sometimes act as a $\lambda/2$ plate, sometimes as a $\lambda/4$ plate, etc. A plane polariser follows the crystal, oriented parallel to the original beam polarisation. For those frequencies at which the crystal corresponds to a $\lambda/2$ plate this second polariser will extinguish the beam. In contrast, the full power will be transmitted for frequencies at which the crystal provides no net polarisation rotation. The number of cycles between extinction and transmission is a function of the amount of chirp and the thickness and birefringence of the crystal. In principle, the pulse spacing could be tuned by adjusting the grating spacing in the stretcher. Figure 5.8 shows calculations of pulse trains created by this method.

This 1-crystal method of generating the pulse train is complicated by the fact that cubic dispersion in the original stretched pulse results in a non-uniform spacing between pulses in the train. This fact could be either an asset or liability, depending on the pattern of coherence zones in the gas target. The effect of cubic dispersion for this pulse train scheme was explored in an

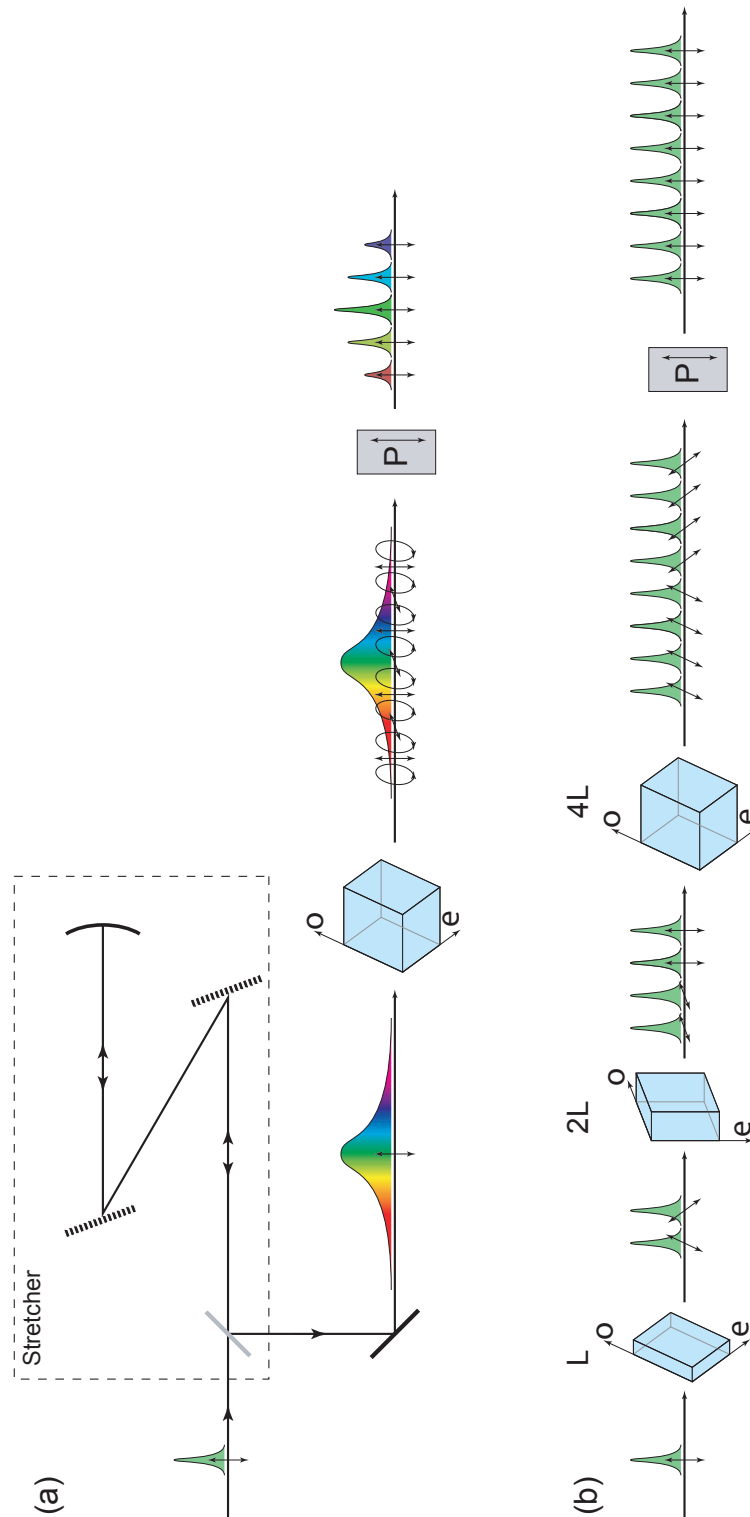


FIGURE 5.7: (a) The 1-crystal method for creating a pulse train. (b) The N-crystal method, for $N=3$. The polarisation state is indicated by the arrows under the pulses.

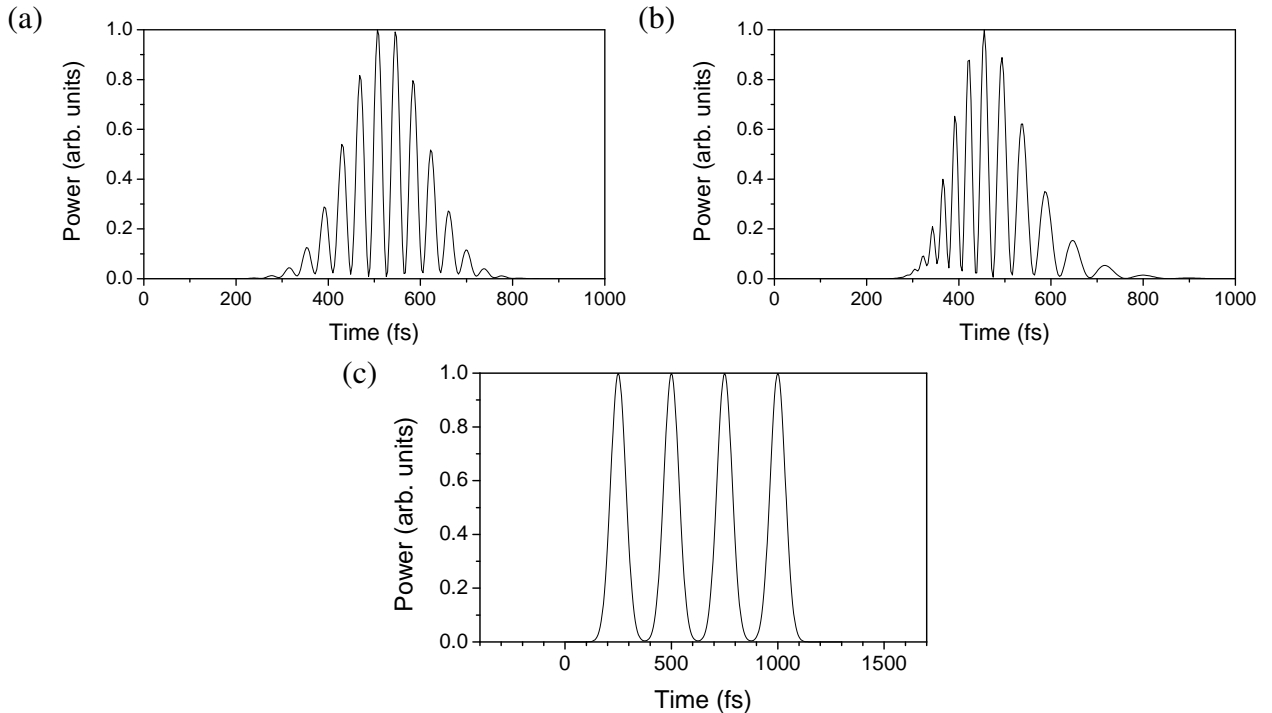


FIGURE 5.8: Calculated pulse trains produced by the two methods. (a) A pulse train created by the 1-crystal method assuming no cubic or higher-order dispersion in the initial pulse. (b) A pulse train for the same initial pulse length and stretcher parameters, but now including all orders of dispersion, and resulting in non-uniform pulse spacing. (c) A pulse train produced by the N-crystal method with $N=2$. (a) and (b) adapted from [103].

M.Phys. project by K. C. Lee[103], who found the effect to be highly significant in shaping the output when realistic stretcher parameters were considered.

A second complication of this 1-crystal scheme is that the group velocities are different in the crystal along the ordinary and extraordinary directions. Hence, the envelopes of the ordinary and extraordinary components of the pulse will not overlap completely, and consequently the contrast between peak extinction and peak transmission will be less than perfect. If the pulse train is sent through a second-harmonic crystal, the ratio of peak intensity to minimum intensity would be squared, and the contrast would consequently be improved. Using counter-propagating light of double the driver frequency in this manner would not fundamentally alter the physics of HHG extinction outlined earlier in this chapter, though the quantitative estimates of required energy would have to be revised.

5.2.2 N-crystal method

The second possible pulse train scheme makes use of multiple birefringent crystals rather than just one crystal. Consider a plane polarised pulse propagating through a birefringent crystal at 45° between its ordinary and extraordinary axes. As the group velocity is different for the two orthogonal components, two pulses of $\pm 45^\circ$ linear polarisation relative to the original will exit the crystal at slightly different times. The spacing between the two pulses is linearly related to the thickness of the crystal. With a sequence of crystals of length $L, 2L, 4L, \dots, 2^n L$, the number of pulses will be doubled at each crystal if the optical axes are 45° different from one to the next. In practice two different materials might be used, one of low birefringence for the small splittings and one of high birefringence for the large ones. As the number of crystals required is a logarithmic function of the number of pulses, this method scales reasonably well to long pulse trains. The separation between the pulses which emerge could be tuned somewhat by rotating the optic axes of the crystals towards or away from the propagation direction. If the optic axes are perpendicular to the propagation direction then the full birefringence of the crystals will be used, while the birefringence goes to zero when these two directions are parallel.

There are pros and cons to each method. The 1-crystal method produces pulses of varied amplitude, and with less contrast between the peaks and troughs. It also requires a stretched input pulse. The multiple-crystal method produces a perfectly even train with excellent contrast. However, the pulse spacing is difficult to adjust, and the cost could be high since multiple unique crystals must be purchased.

Though Peatross *et al* do not reveal how they create their train of five pulses, it is unlikely to be by either of the two methods discussed here, which produce either an ambiguous number of varied pulses, or a quantity which is a power of two. If Peatross's method relies on beamsplitters, as is likely, the number of optics required would scale linearly with the number of pulses, meaning it would be prohibitively unwieldy and expensive for long trains.

CHAPTER 6

Experimental systems

6.1 Laser machining

Glass capillaries can be purchased with a pre-formed smooth axial channel. However, in order to supply gas to a selected section of the capillary length, it was necessary to make additional *radial* holes in the capillaries. The best way to machine these radial holes is by laser ablation, so a pre-existing laser-machining apparatus in the Oxford laboratory was adapted for this purpose. A system, built by group member A. Gonsalves, used computer-controlled *xyz* translation stages to move the job relative to a focused 1 kHz, 400 mW, 50 fs laser. The light was derived from the same laser system used for the HHG experiments (described in section 6.4.1) before the final amplifier stage. Two modifications to the laser machining system were made by the author to adapt it for the new task: the hardware was modified in order to mount the capillaries on the computer-controlled stages, and software was developed to machine holes of the desired shape. Figure 6.1 shows a typical job.

6.2 Mounting of capillaries

To use capillaries in a HHG experiment, they must be mounted such that the ends of the bore are held at vacuum, and the target gas must be supplied from the sides. Also, the capillary's

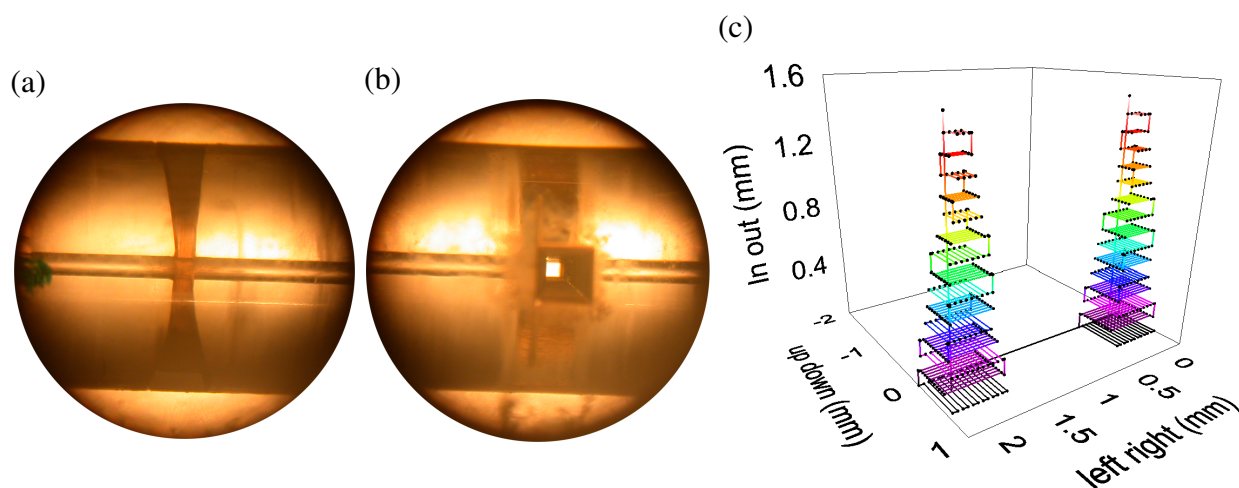


FIGURE 6.1: (a)-(b) Two views of a typical gas entry hole machined into a $178\ \mu\text{m}$ diameter capillary. (c) Typical path of the laser focus as it cuts a pair of such holes. Only one half of the diameter-length cut is plotted; to cut the second half, the capillary is manually rotated by 180° and the machining program run a second time.

position should be adjustable along five degrees of freedom: pitch and yaw rotation, and 3D translation. All of these requirements are met by mounting the capillaries rigidly within a larger ($10\ \text{cm} \times 10\ \text{cm} \times 16\ \text{cm}$) housing, and the housing in turn mounted by flexible bellows and to a five-axis rotation stage. A system of o-ring seals inside the housing connect the appropriate capillary orifices either to vacuum or to the gas supply.

The Astra experiments were conducted using a perspex housing which had been developed previously for experiments with capillary discharge waveguides. This housing, while well suited for these discharge experiments, had several drawbacks for HHG experiments. First, the perspex tended to crack. Perspex had been used because the discharge experiments required that the housing be made from an electrical insulator, and it was useful to be able to see the discharge; neither criterion applied to the HHG experiments. Secondly, to use a capillary of a new length, or with gas entry holes at a new position, several complicated components had to be machined to accommodate the new dimensions. This was a major drawback, as it was often decided at Astra to make unanticipated changes to the capillary length or gas hole design. Finally, the perspex housing could not mount capillaries of more than 70 mm in length.

Consequently, a new aluminum housing was designed by the author for mounting glass capillaries. The aluminium material was more durable and was more straightforward to machine. Capillaries of up to 120 mm could be accommodated. To mount a capillary of a new length, or

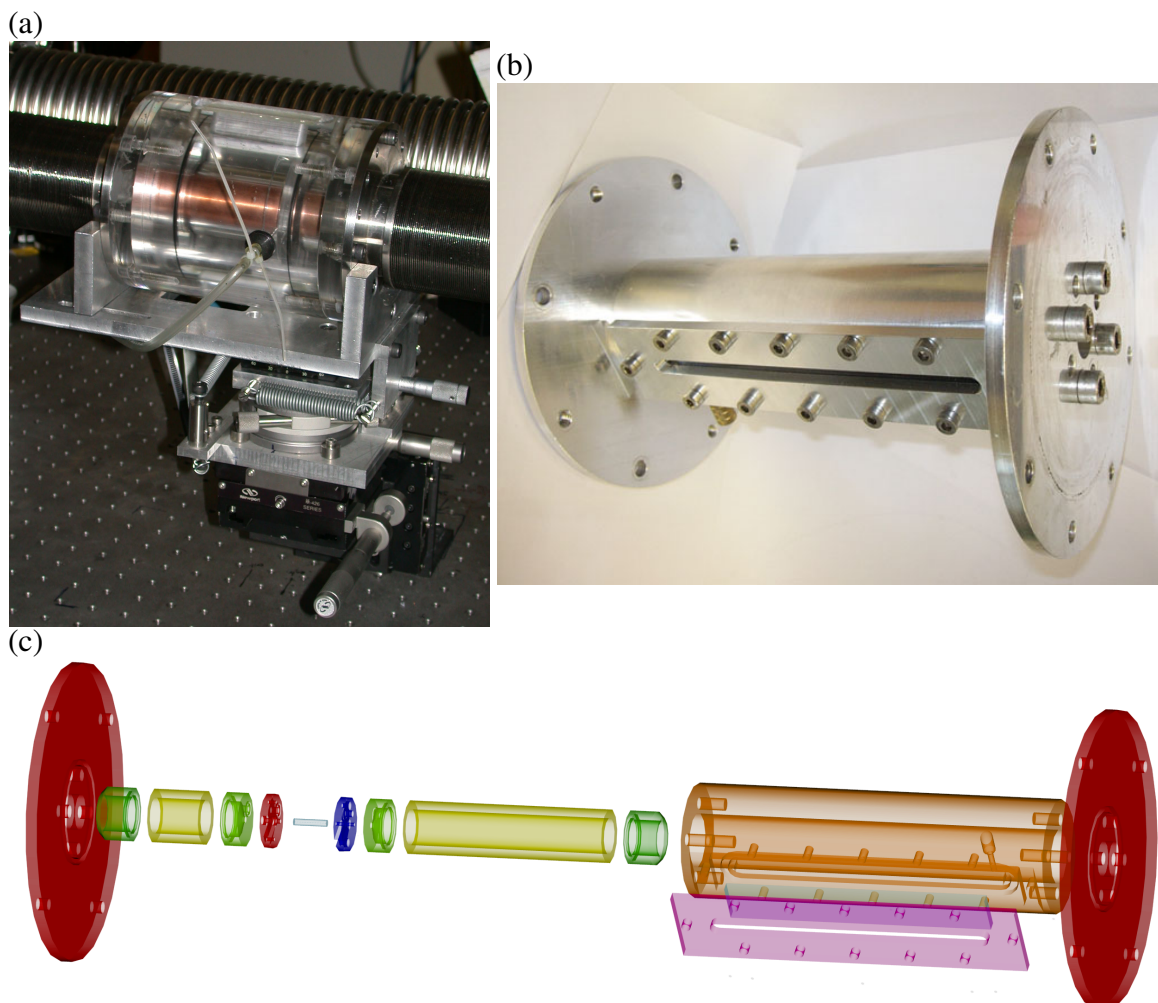


FIGURE 6.2: (a) The original perspex housing, mounted atop its five-axis stage. (b) Photo of the new aluminium housing. (c) CAD rendering by the author of the new housing showing the internal components.

with gas holes in a new position, the new parts required were much less complicated to manufacture, and could be made rapidly by a student without the help of a professional machinist.

6.3 Astra laser

The first of the two experimental campaigns was performed on the Astra Ti:Sapphire laser at the Rutherford Appleton Laboratory. In the target area used for these experiments (target area two), Astra is capable of delivering 500 mJ, 40 fs, 800 nm pulses on target at 2 Hz. The system uses chirped pulse amplification, with the pulses stretched to 500 ps during the three amplifier stages, and recompressed in a vacuum chamber connected to the target chamber.

The optics to split the beam into driver and counter-propagating beam (CPB) and to split

the CPB into a pulse train were placed between the final amplifier stage and the compressor. As both the compressor and pulse-splitting optics apply a linear transfer function to the input electric field $E(t)$, it makes no difference which system comes first. Placing the splitting optics after the compressor would have required that they be contained in vacuum, an undesirable complication. Also, due to the higher intensity, there would have been a greater possibility of nonlinear effects or of damage to the optics. The possibility of damage to the splitting optics could have been further reduced by placing them even earlier – before the final amplifier stage – but this would have created other problems. The amplifier would have to be realigned from scratch. Also, due to saturation in the final amplifier, the first pulse in the train would grow larger than later pulses.

Figure 6.3 shows the optics used at Astra before the compressor. The single Astra beam was split into a driver and CPB using a mask with two soft apertures (i.e., holes with a fine zig-zag edge to reduce diffraction effects). Roughly half of the laser energy was lost to the mask. As the beam before the mask had a roughly top-hat spatial intensity profile, the two beams afterwards were reasonably axisymmetric. Both beams had a diameter of roughly 22 mm. To split the CPB into a train, the N -crystal pulse splitting method was implemented. The driver arm contained a timing slide, so the longitudinal position of collision between the two pulses at the target could be controlled. Each arm contained an energy control, consisting of a half waveplate followed by a polariser. Both the timing slide and the energy-control waveplates were motorised and computer controlled. Using the leakage through a dielectric mirror, a pair of photodiodes measured the energy of each beam. The two beams were brought adjacent and parallel and then sent together into the compressor. Since both beams used the same compressor, the grating separation could not be tuned separately for each pulse. As the CPB arm had a high GVD due to the splitting crystals and extra polariser, a “GVD compensator,” a short segment of high-index glass, was placed in the driver arm. This brought the aggregate GVD of the driver and CPB arms close to the same value. To keep the duty cycle of the pulse train close to 1:1, the GVD compensator was designed to leave some difference in the GVD between the arms. The compressor grating separation was tuned to minimise the driver pulse length, leaving the duration of each CPB pulse at 80 fs (according to calculations.) The driver pulse length was

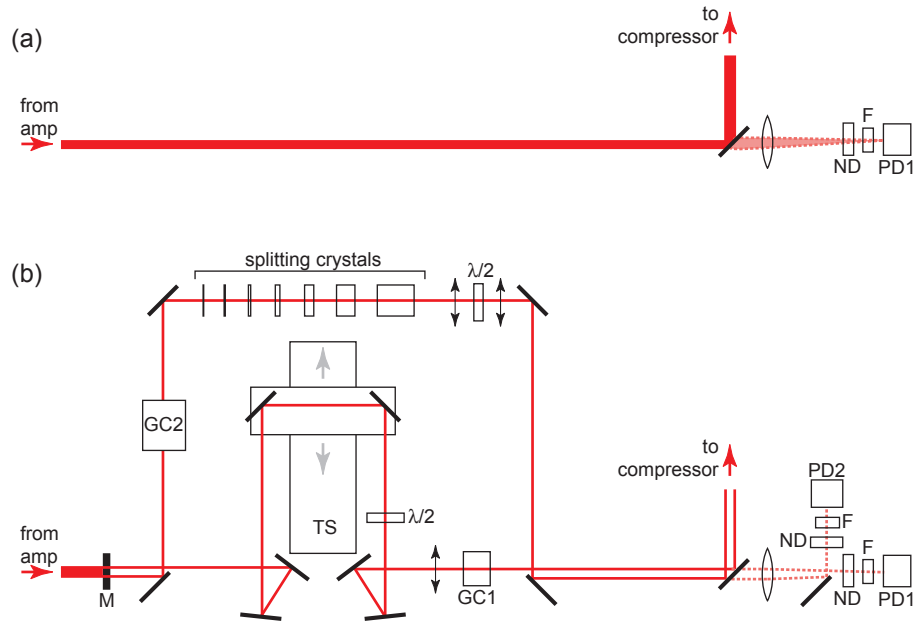


FIGURE 6.3: Optics inserted before the compressor for the Astra experiment. (b) shows the beamline as modified for the experiment discussed here, while (a) shows the standard Astra configuration for comparison. M: mask with two holes. GC: GVD compensator. TS: timing slide. \updownarrow : polariser. $\lambda/2$: half waveplate. ND: neutral density filter. F: 800 nm bandpass filter. PD: photodiode. Solid beams: > 1 mJ driver and CP beams. Dotted beams: low energy beams used for energy measurements.

measured with a SPIDER to be 41 fs. For some experiments the duration of the CPB pulses was increased by placing extra glass – and therefore extra GVD – in the CPB path (GC2 in the figure).

Following the compressor, the two beams were separated and focused on the target from opposite directions using $f=1$ m singlet lenses, as shown in figure 6.4. The lenses were mounted on motorised xyz stages so the focus position could be adjusted. A rotatable half-waveplate in the CPB arm was used to switch between the parallel-polarisation and perpendicular-polarisation schemes. For imaging the transmitted CPB mode and measuring its energy, light was collected using the same lens that focused the driver beam. The collimated beam, after leaking through a dielectric mirror, was focused using an achromatic doublet, then magnified and imaged onto a QImaging CCD camera using a microscope objective. The energy was measured using the same beam and a Molectron pyroelectric calorimeter. A second pair of these same diagnostics was configured for the transmitted driver beam. Rather than use leakage through a mirror, this pair of diagnostics used the 4% reflection from the uncoated side of a glass flat that was anti-reflection coated on one side only.

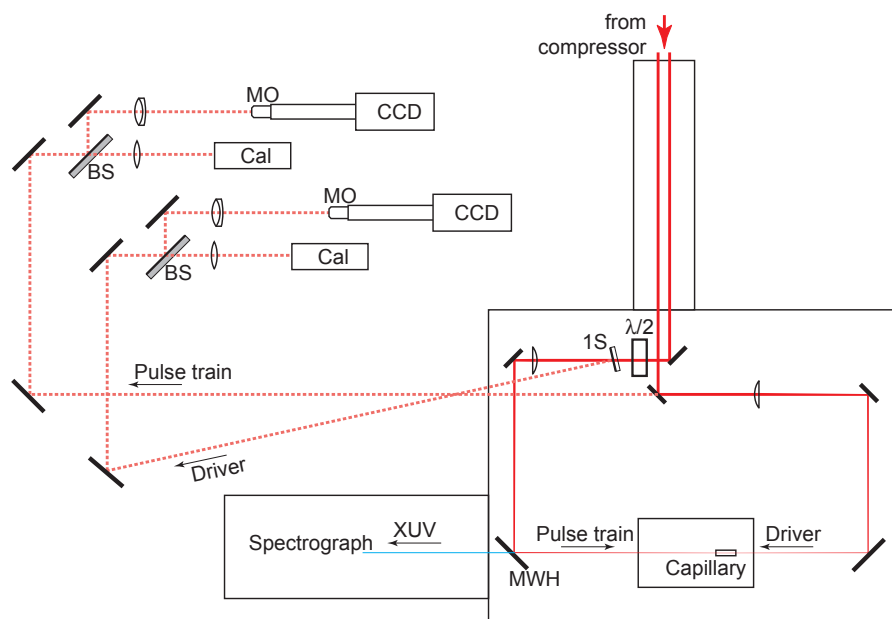


FIGURE 6.4: Optics that followed the compressor for the Astra experiment. $\lambda/2$: half waveplate. 1S: flat which is AR-coated on one side only. MWH: mirror with hole. BS: 50% beamsplitter. MO: microscope objective. Cal: pyroelectric calorimeter. Solid beams: > 1 mJ driver and CP beams. Dotted beams: low energy reflections used for energy measurements and focal spot imaging.

The maximum possible energy on target, measured by placing a Molelectron calorimeter after the focusing lenses, was 45 mJ for the driver and 14 mJ for the CPB. Though the beam energies were roughly equal following the mask, half of the CPB energy was lost at its first polariser, and additional energy was lost due to the large number of optical surfaces in the beamline.

The XUV emission passed through a 2 mm-diameter hole in one of the CPB turning mirrors. Unfortunately, there was not time to examine how much the hole affected the quality of the CPB focus or the imaging of the driver focus. The XUV light was analysed with a flat-field spectrograph, which consisted of a grazing-incidence Au focusing mirror, a 1200 l/mm grating, and a cooled Andor CCD. To prevent the 800 nm light from saturating the CCD, various filters of sub-micron thickness were placed before the grating. Typically 2-300 firings of the laser were integrated on each CCD exposure; in the following chapters the term “shot” will refer to a CCD exposure rather than to a single laser pulse.

6.4 Oxford terawatt laboratory

6.4.1 Original configuration

The Oxford laser, also a chirped pulse amplification Ti:Sapphire system, is much the same as Astra's "Target Area 1" beam. The Oxford system is capable of 10 Hz, 125 mJ, 50 fs pulses. After the compressor, the spectrum was measured to be centred about 808.8 nm. The repetition rate drops from 1 kHz to 10 Hz between the final two amplifier stages, and the discarded pulses are compressed and used for the laser machining system described earlier. The 10 Hz system is normally used for guiding and x-ray laser experiments, for which no CPB is needed. This configuration is illustrated in figure 6.5.a. The facility was used in this 1-beam configuration in an attempt to reproduce certain observations from the Astra campaign; these experiments will be discussed in section 8.5. In this original configuration, the beam was approximately Gaussian with a $1/e^2$ intensity radius of 14 mm, and an $f=914$ mm parabola was used for focusing. A flat-field spectrograph, virtually identical to the one used at Astra, measured the XUV emission.

6.4.2 Modifications

In January 2006, the system was modified to add a counter-propagating beam. Design of these modifications occupied the author for much of May through December 2005.

For the same reasons described earlier, the splitting optics were placed before the compressor. Great care was taken in the design to keep the fluence on the compressor gratings at or below previously used levels. A beam-expanding telescope was included both for this purpose and also to reduce the fluence on the other splitting optics. The lens separation in the telescope was adjustable so the divergence of the beam could be tuned.

As the energy of Oxford system was less than 10% of that of Astra, a less wasteful method of splitting the beams was needed. Consequently, an $R=25\%$ beamsplitter was used instead. This method had the added advantage that no hard edges were put on the beams.

The other pre-compressor components were all comparable to those used in the Astra experiment. However, except for the calcite splitting crystals, none of the Astra optics were re-used

at Oxford. As with the Astra system, the Oxford system included a computer-controlled timing slide, a GVD compensator, two independent energy controls, and two photodiodes to measure input energy. Because of the high cost of computerised motion-control equipment, some of the timing slide system and its control software was made in-house by the author. Unlike in the Astra design, the Oxford GVD compensator was designed to exactly equalise the GVD of the two arms, as computed by summing the calculated GVD for each optical component in the system. However, uncertainty remained regarding pulse compression; this will be discussed further in section 9.2.9.

The new layout made use of only pre-existing vacuum chambers. As at Astra, the Oxford system included a half waveplate for the perpendicular-polarisation method, a mirror-with-hole to let the XUV light escape, and singlet lenses for focusing. Both lenses were $f=679$ mm and both beams had a $1/e^2$ diameter of 13 mm, giving a theoretical minimum spot size of $27 \mu\text{m}$, and a matched grazing-incidence waveguide diameter of $84 \mu\text{m}$. Each beam had a photodiode to record the transmitted energy and an achromat-objective-CCD system for imaging the light as it exited the capillary. The photodiodes were covered with a filter that flattened their frequency response. The CPB focus could be moved longitudinally by up to 125 mm using a stage (ECS in the figure) to accommodate capillaries of different lengths. The energy-on-target was roughly the same for the two beams: 17 mJ for the driver and 19 mJ for the CPB.

Several alternative options were considered in the design process. For example, use of a variable-zoom telescope was considered to allow control over the focal spot size (without the energy loss that would accompany an iris). This option was rejected due to the unavailability of ready-made variable-zoom telescopes with sufficiently high damage threshold. Designs were also considered for which the driver and CPB had unequal diameters and energies. It was ultimately decided to go with the equal-energy, equal-diameter design to make the optics more interchangeable and the imaging systems more similar.

Because of the inability to move the lenses once under vacuum at Oxford, a different alignment protocol was devised. First, with the chambers vented and the two lenses removed, the two beams were aligned to a pair of cross-hairs that had been previously aligned to the spectrograph axis. The lenses were then put in place and the two beams again aligned to the crosshairs

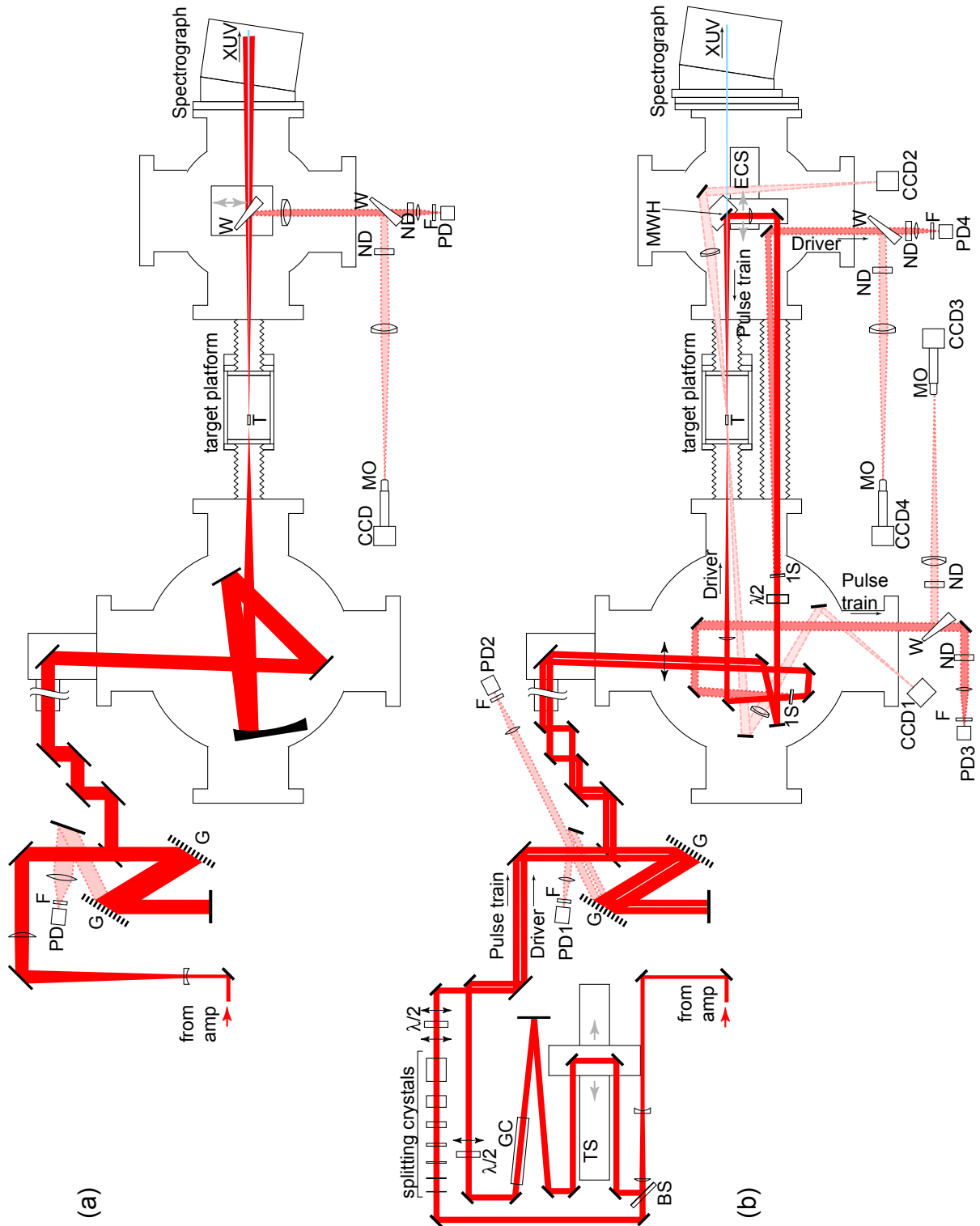


FIGURE 6.5: (a) Original configuration of the Oxford compressor and target chambers, the starting point from which the Oxford CPB experiment was designed. (b) The Oxford facility after modification for the CPB experiment. GC: GVD compensator. TS: timing slide. \uparrow : polariser. $\lambda/2$: half waveplate. G: compressor grating. 1S: flat which is AR-coated on one side only. MWH: mirror with hole. BS: R=25% beamsplitter. MO: microscope objective. F: photodiode response-flattening filter. T: capillary or gas cell target. ECS: Exit chamber stage. W: wedge. ND: neutral density filter. Solid beams: > 1 mJ driver and CP beams. Dotted beams: low energy reflections used for energy measurements and focal spot imaging. Dashed beams: diffuse reflections used for capillary alignment.

by transverse translation of the lenses. The beam pointing at this point was fairly exact, but it was fine-tuned using the following additional procedure. The driver was used to drill a hole in a sheet of metal. The resulting pinhole was then moved towards the spectrograph and precisely parallel to the driver axis by the length of the capillary. The CPB beam was then aligned through the pinhole by transverse translation of the CPB-side lens. The beam pointing was now quite precise. The capillary housing was mounted in place and the chambers were pumped down. Both beams were left untouched. The capillary was then aligned such that its axial holes lined up with the beams. This step was greatly aided by a pair of CCD cameras that imaged the (relatively dim) diffuse reflection from the capillary ends (CCDs 1 and 2 in the figure). The capillary rotation stages were designed to rotate about the driver-side capillary entrance. Thus, the driver entrance could be aligned to the driver beam by pure transverse translation, and the CPB entrance aligned to the CPB afterwards by pure rotation (pitch and yaw). This alignment procedure for the Oxford experiment required that neither beam move significantly during pump-down. It was determined that the chambers were stable in this regard by watching the position of the spots on CCDs 3 and 4 as the chambers were evacuated; neither spot moved significantly.

A polariser was included in the first vacuum chamber to prevent beam propagation back up the laser, but it only functioned in the perpendicular-polarisation scheme. For the parallel-polarisation scheme, which was only attempted using a gas cell target and not with a capillary target, an alternate method was needed to prevent backpropagation. For these experiments the CPB was steered off the driver line by the width of the beams, i.e., so that the beams only overlapped at the focus. This rotation amounted to roughly 2° . Each beam consequently missed the other's focusing lens, and so no backpropagation occurred. There are several downsides to this precautionary method. First, as the light is not collected after the focus, the imaging cameras (CCDs 3-4) cannot be used. Also, it would be impossible to guide both beams in a long capillary simultaneously because the beams are non-coaxial. It was found that simultaneous two-way guiding in 100 mm capillaries was impossible when the two beams were non-coaxial by amounts even much smaller than 2° . Thus, although the method works for a gas cell target, it cannot be used with capillaries. In gas cells the non-coaxial pointing slightly diminishes the

overlap between the two beams, but the change is small compared to the total overlap volume. Peatross *et al* saw no change in the efficacy of HHG extinction when the CPB was rotated 2° off the driver axis [91].

The Oxford experiment suffered from poor beam quality. The problem was particularly bad in the CPB due to the calcite splitting crystals. Two of the seven crystals left noticeable streaks on the near field of the transmitted beam. In one experiment to find the focus of each beam by burning pinholes in a piece of metal at different longitudinal positions, it was found that for equal beam energies, the CPB burned holes of twice the diameter of those burned by the driver. In addition, both beams possessed a ~ 1 mm-diameter hotspot. This spot burned the antireflection coating on the driver-side lens, and left dark streaks through the preceding 1-side-coated flat. The spot was limited to a roughly 20 cm longitudinal interval, the position of which could be adjusted by changing the divergence of the beam-expanding telescope. Despite a lengthy search, the origin of the hotspot was never found.

6.4.3 Spectrograph calibration

A calibration is needed in order to map wavelengths to pixels of the spectrograph CCD. Several calibration methods were considered and compared at Oxford. One relatively fast method for calibration is to use an aluminium light-rejecting filter and locate the first and second order positions of its absorption L-edge. The L-edge is at 17.1 nm, and in second order it creates an apparent absorption edge at 34.2 nm. These edges can be observed by creating quasi-continuum XUV radiation, obtained by focusing the CPB onto a solid piece of iron or copper. A linear fit can be made between these two wavelength-pixel pairs. High-harmonic spectra plotted according to this calibration are shown in figure 6.6.A-B, along with the theoretical positions at $808.8 \text{ nm}/q$. The observed harmonics line up poorly with their expected locations. Nonetheless, from the L-edge landmark at 34.2 nm (which lies between $q=23$ and $q=25$) the appropriate value of q for each spectral peak can be identified. To measure the small absolute blueshifts of harmonic lines, however, a more precise non-linear pixel-to-wavelength calibration is required.

A nonlinear calibration based on laser plasma emission lines was also considered. The plasma was created as before with the CPB, but using aluminium or polyethylene as a target.

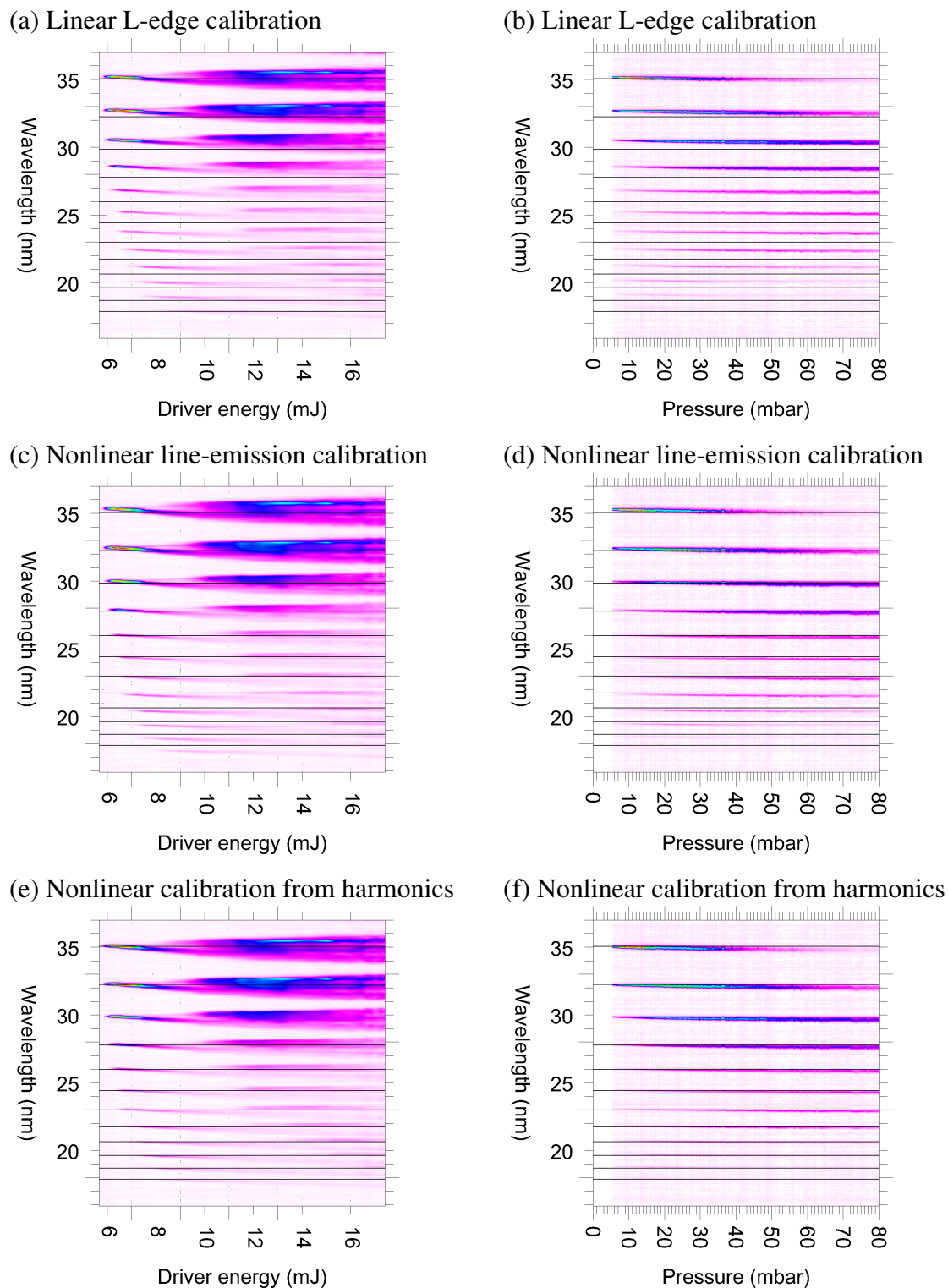


FIGURE 6.6: Scans showing harmonic spectra according to three methods of pixel-to-wavelength calibration. Horizontal lines mark the theoretical positions at $808.8 \text{ nm} / q$. Data are shown for scans of pressure and driver energy to highlight the effect of blueshifting on the harmonic locations.

The relevant atomic transitions were identified by group member C. Woolley. As figure 6.6 shows, the fit to the harmonic lines is much improved using this method. Unfortunately, there are many ways to pair known line wavelengths with observed lines, and therefore there is always some uncertainty in the calibration.

Blueshifting increases with both laser energy and pressure, and these trends are both visible in figure 6.6. In the limit of laser energy $\rightarrow 0$ no blueshifting is expected from either the ionisation or nonadiabatic blueshifting mechanisms (section 2.4). Consequently, at the left edge of the energy scan plots, the harmonics should align exactly with the $808.8 \text{ nm} / q$ lines, as long as the driving pulse is perfectly compressed and centred on that wavelength. If the driver has chirp or is otherwise imperfectly compressed, harmonic peaks may be shifted by different amounts depending on the driver wavelength at the moment those harmonics are generated [104].

According to the nonlinear line emission calibration, the harmonics do not align with their expected locations at low driver energy and pressure, appearing shifted to the red for low orders and to the blue for high orders. This discrepancy could be due to imperfect compression of the driving pulse. It is also possible that there is a slight error in the line emission calibration. While there were no recorded adjustments to the spectrograph between the times the line emission and harmonic spectra were taken, it is conceivable that the grating or focusing mirror were accidentally moved by a small amount during this interval. In addition, there is the aforementioned uncertainty in the line-wavelength pairings. Due to these uncertainties in the line emission calibration, all Oxford data presented in the rest of this thesis will use a calibration based on the locations of the harmonics for shots in which pressure $< 20 \text{ mbar}$ and laser energy $< 6.5 \text{ mJ}$, conditions for which blueshifting seems to be negligible. As this calibration presumes that there is no significant variation in wavelength during the driver pulse, it too is imperfect.

The calibrations performed for Astra data presented in this thesis were less precise. For the $17 \text{ nm} < \lambda < 20.4 \text{ nm}$ region of the spectrum, observed emission lines were paired to atomic transitions by B. Dromey. However, only a plasma formed from capillary material was considered. The observed lines could therefore have come from either of two elements (Si and O), making it harder to be certain of the line-wavelength pairings. Furthermore, the observed

emission lines were extremely broadened. For $\lambda > 20.4$ nm, harmonics were matched to the positions $800 \text{ nm} / q$. However, the precise central wavelength of the laser was not known. Also, blueshifting is likely to be large in the Astra data, as capillaries rather than thin targets were used, and so the calibration here could be wrong by up to 50% of the inter-harmonic spacing. For the $\lambda < 17$ nm region, emission lines cannot be seen through the filter. Here, then, a calculation by B. Dromey and D. Neely based on the grating equation and the spectrograph geometry was used instead. The uncertainty in this calibration has been estimated by M. Zepf to be ± 0.2 nm.

CHAPTER 7

Measurements of Pulse Trains

During the experimental campaigns at Astra (January - March 2005) and at Oxford (January - April 2006), pulse train optics for the N-crystal method were implemented. A cross-correlation scheme, described below, was used to diagnose the pulse trains. These measurements provide a useful foundation in understanding our later attempts at quasi-phase match harmonic radiation.

7.1 Auto-correlation versus cross-correlation

The system initially employed to diagnose pulse trains was a home-made standard autocorrelator (figure 7.1.a). This system suffered from several problems. Most fundamentally, many details of the pulse train were washed out because the pattern was being convolved with a complicated function (itself.) Figure 7.2.a shows an autocorrelation trace of a pulse train created using the 1-crystal method. Based on the optics used to create this pulse train, it was believed that there were several hundred pulses in the train. The signal shows a wide fringe-free peak punctuated by several fringes at the maximum. It is believed that this signal results from cubic dispersion from the stretcher which, as described in section 5.2.1, causes the pulse spacing to vary from short to long across the train. This variable pulse spacing would prevent individual pulses from being resolved in the autocorrelation when the two copies of the train were displaced by more than a fraction of the total train length, resulting in the observed fringe-free regions. A calculation by K. C. Lee (figure 7.2.b) which includes this effect of cubic dispersion

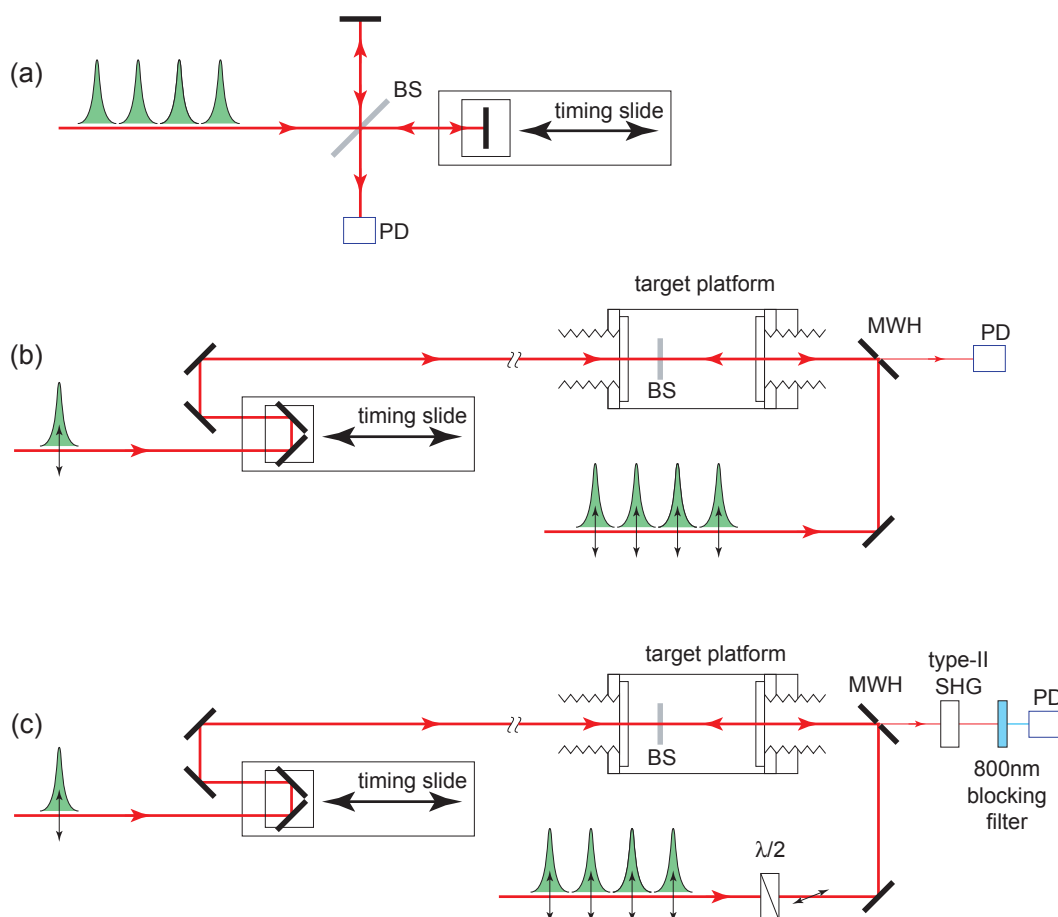


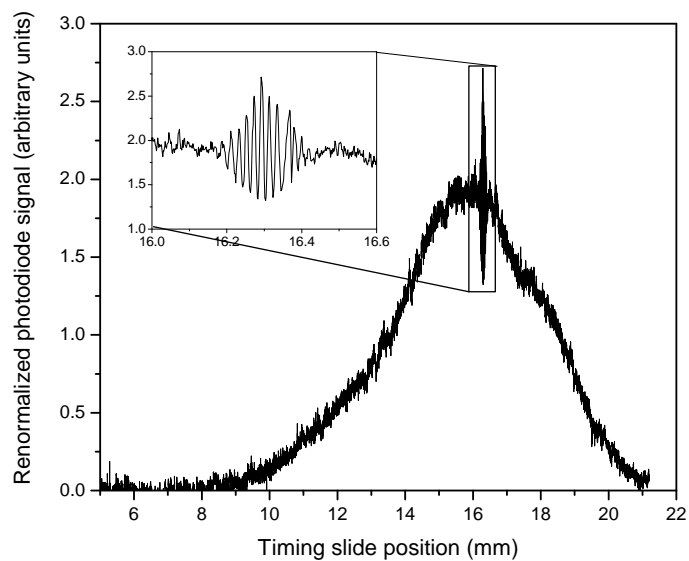
FIGURE 7.1: Evolution of the correlation techniques used to diagnose pulse trains. (a) Autocorrelator using two-photon diode. (b) Cross-correlator using two-photon diode. (c) Cross-correlator using type-II phase matching. BS: beamsplitter, PD: photodiode sensitive to 400nm but not 800nm, MWH: mirror with hole, $\lambda/2$: half waveplate.

is able to reproduce the measured signal with remarkable accuracy. This calculation is based on the exact geometric values from the stretcher and optics, and includes no free parameters aside from a scalar multiplier to the amplitude and an additive offset to the timing slide position.

Following this measurement, only pulse trains created using the N-crystal method were considered. This decision was largely due to the advantages of this method: uniform pulse amplitude, uniform pulse duration, higher contrast in intensity between peaks and valleys in the train, and less ambiguity in the pulse spacing and duration.

A change was also made to a less ambiguous diagnostic technique: cross-correlation of the pulse train with a single pulse (figures 7.1.b-c). Such cross-correlation produces a signal-versus-timing-slide plot that closely mirrors the intensity-versus-time function of the pulse train. The pulses are all convolved with the probe pulse, so the measured signal has wider pulses than the

(a)



(b)

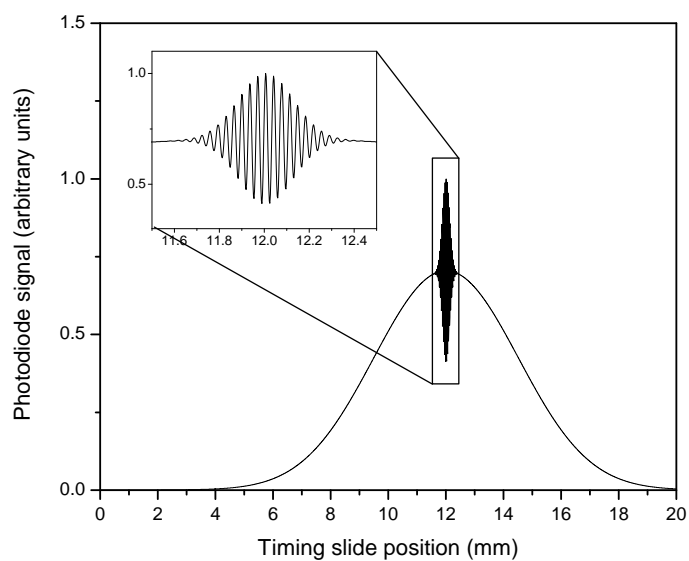


FIGURE 7.2: Autocorrelations of a pulse train created with the 1-crystal method. (a) Measurement from November 2004 in preparation for the Astra experiment. (b) Autocorrelation simulated by K. C. Lee for the experimental parameters used in (a) (Figure adapted from [103].) The vertical axes are not comparable between the plots, and there is an unknown additive offset relating the horizontal axes. The width of the broad fringe-free curve is directly related to the width of the envelope of the pulse train, and to the width of the chirped pulse from which the train is derived. The separation of the fringes at the peak is directly related to the spacing between pulses in the train.

actual train. Consider a probe pulse of full-width at half-maximum intensity (FWHMI) = τ_p , and an individual pulse in the train of FWHMI = τ_t . Since the probe beam traverses the length of the timing slide twice, a slide position of x corresponds to a time delay of $2x/c$ between the pulses when they arrive at the doubling medium. Assuming both pulses are Gaussian, the intensities of each beam at the doubling medium are:

$$I_p(t) = I_p \exp\left(-4 \ln 2 \left[\frac{t}{\tau_p}\right]^2\right) \quad (7.1)$$

$$I_t(t) = I_t \exp\left(-4 \ln 2 \left[\frac{t - 2x/c}{\tau_t}\right]^2\right) \quad (7.2)$$

The measured signal s is proportional to the fluence of the frequency-doubled light, which in turn is proportional to the integral of the instantaneous product of the probe and train intensities:

$$s(x) = \int_{-\infty}^{\infty} I_p(t) I_t(t) dt \quad (7.3)$$

$$= s_0 \exp\left(-4 \ln 2 \left[\frac{x}{\sigma}\right]^2\right) \quad (7.4)$$

where several constants have been absorbed into s_0 and

$$\sigma = \frac{c}{2} \sqrt{\tau_p^2 + \tau_t^2} \quad (7.5)$$

The resulting experimentally-accessible signal $s(x)$ is evidently a Gaussian with FWHM of σ . If the duration of the probe pulse is known, the above equation can be solved for τ_t to find the width of the pulse train pulses. In particular, if the pulse durations are the same ($\tau_t = \tau_p$), then

$$\tau_t = \frac{\sigma \sqrt{2}}{c} \quad (7.6)$$

For more complicated pulse shapes or trains in the counter-propagating beam, cross-correlation scans could be deconvolved using a Gaussian of the appropriate width (corresponding to the probe pulse duration).

An additional advantage of the cross-correlation system was that it allowed determination with better than 1 mm accuracy of the timing slide position required for the pulses to collide at

the target. This value was a useful point of reference later when looking at harmonic spectra.

Initially, to avoid the cost of a frequency-doubling crystal, photodiodes were used that were sensitive to 400 nm but not to 800 nm. Cross-correlation scans could indeed be taken with these photodiodes, but the scans suffered from a large offset signal. This offset was present because each pulse doubled with itself even when the probe pulse and train were widely separated in time. The offset was problematic because it was sensitive to shot-to-shot variation and drifts in laser energy. Doubling with a type-I crystal would have produced the same problem. The problem was resolved by moving to a type-II doubling crystal and rotating the polarisation of the pulse train by 90° (figure 7.1.c). All data reported here aside from figure 7.2.a were obtained using this last scheme.

Figure 7.3 shows measured cross-correlation scans in which all pulse train optics were in place, but the train was set to contain only one pulse. This was done by orienting all of the splitting crystals so their ordinary or extraordinary axes were aligned to the beam's polarisation. Figure 7.3.d is from the 2005 Astra experiment. There, the FWHMI of the probe pulse was measured to be 41 fs using a SPIDER. The train was expected to have a duration different from this value because the aggregate GVD of the probe beam arm differed significantly from that of the train beam arm. Averaging the FWHM of the fit to this scan with that from additional scans, the mean FWHM comes out at 0.0178 mm. When combined with equation 7.5, this yields an estimate of 111 fs for the FWHMI of each pulse train pulse. This value is reasonable given the expected GVD of the optical components.

During the Oxford experiment, the compressor grating separation and the amount of GVD in the optical system were adjusted on several occasions; these changes are discussed further in section 9.2.9. Figure 7.3.a shows the cross-correlation for the final setting of these parameters, which applies to most of the data from Oxford presented in chapter 9. In this configuration, the pulse compression was set using the following procedure. The compressor gratings were first adjusted – by optimising white light generation – to minimise the duration of the CPB pulses. Leaving the gratings at that position, white light generation from the driver pulse was maximised by rotating the GVD compensator in that arm. This procedure should have produced roughly equal pulse lengths in the two arms ($\tau_p = \tau_t$). Using a fit to the cross-correlation data and

equation 7.6, the FWHMI for each beam is calculated to be 280 fs. This result is extremely high compared to past measurements of the Oxford laser pulse duration, which have been typically 50-70 fs. Unfortunately there was not time to measure the pulse duration again with another method to confirm the ~ 280 fs value.

Figure 7.3.c was taken at Oxford for an earlier configuration of the optics, in which the compressor grating separation was different, and there was a different GVD in the driver arm. Using a single-shot autocorrelator, the FWHMI of the driver was estimated to be 90 fs, and the FWHMI of the pulse train was estimated to be 60 fs. Equation 7.5 suggests that the FWHM on the timing slide should be 0.016 mm. The measured FWHM is 0.027 mm. The reason for this discrepancy is unclear. It is also unknown why the FWHM was measured to be lower for this cruder optimisation than for the final optimisation.

The signal-to-noise is much better for the Astra data (figure 7.3.d) than for the data from Oxford. This is likely due to the much thicker SHG crystal used at Astra.

7.2 Satellite fringes

In the final configuration of the Oxford experiment, small secondary peaks of unknown origin were seen approximately 0.11 mm to either side of the main peak (7.3.a-b). This distance does not correspond to any of the splittings due to the calcite. The peaks are seen regardless of the number of pulses in the pulse train (e.g., figure 7.7). The side peaks did not appear in the earlier compressor grating configuration at Oxford (figure 7.3.c) or at Astra. Interestingly, the side peaks differ from the main peak in that they contain resolved fringes (possibly of wavelength scale, though it was not possible to scan at sufficient resolution to determine whether this is the case).

Another secondary signal was observed approximately 4.7 mm away from the main peak (figure 7.4). The existence of this signal was inferred by looking at the change in HHG signal during scans of the timing slide, as a minor extinction was observed 4.7 mm away from the principal extinction (visible in figure 9.22.) The extinction and cross-correlation signals appear on one side of the main signal but not on the other. The 4.7 mm distance is suggestively close

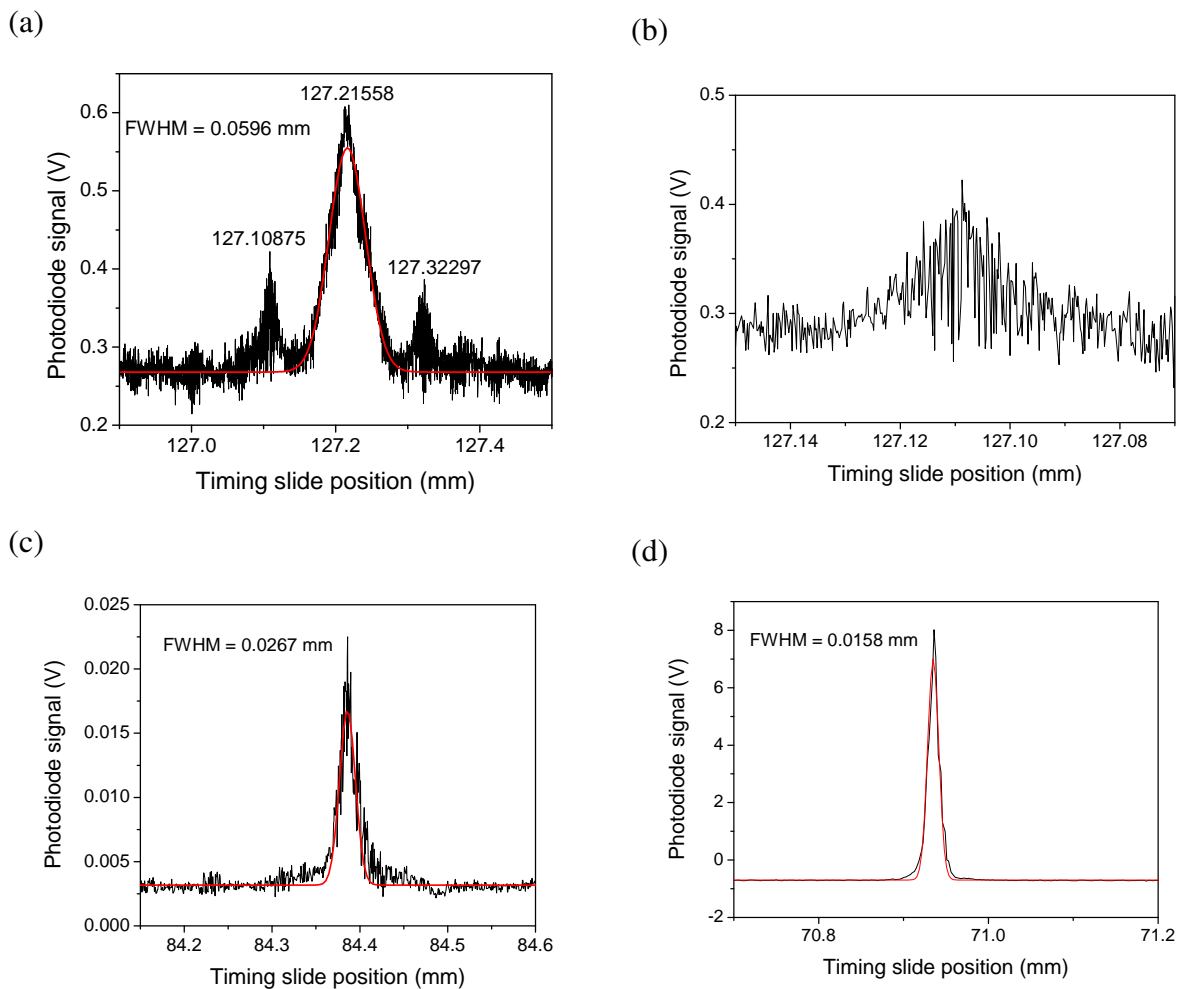


FIGURE 7.3: (a) Satellite peaks seen on cross-correlation at Oxford, 0.11 mm from the main peak. (Satellites are excluded from the region used for the Gaussian fit.) (b) Closeup of one of the sidebands. (c) A previous cross-correlation scan at Oxford in which such sidebands were not observed. (d) Cross-correlation scan from RAL.

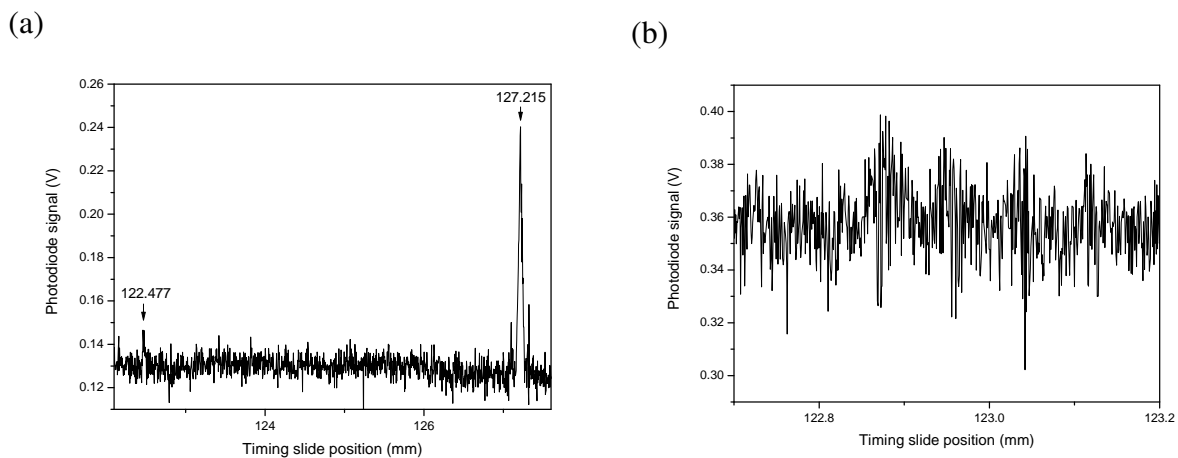


FIGURE 7.4: (a) A secondary cross-correlation peak was observed 4.7mm from the main peak. (b) Close-up of the region of the secondary peak. The absolute horizontal coordinates differ between (a) and (b) due to an error.

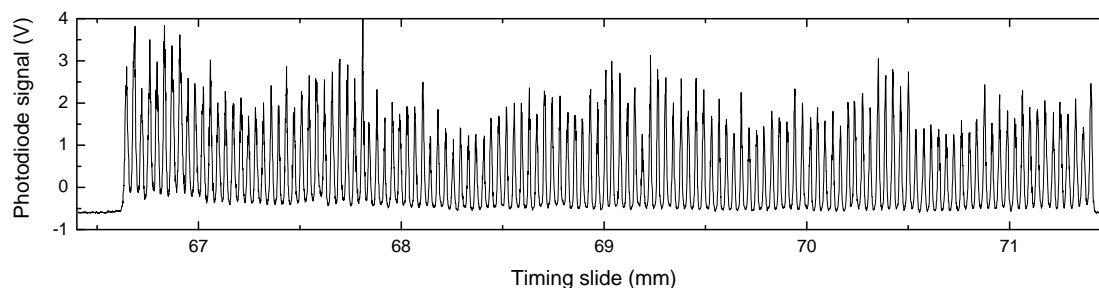


FIGURE 7.5: A train of 128 pulses measured at Astra.

to two times the splitting obtained by engaging the thickest calcite crystal; this was confirmed by intentionally engaging this crystal. A close examination of the satellite signal reveals the presence of multiple peaks. The spacing between these peaks – approximately 0.1 mm – is not consistent with any of the spacings due to the calcite crystals. It could however be consistent with the 0.11 mm spacing of the small side peaks described above. It is unknown whether or not the 4.7 mm peaks were present with the earlier Oxford grating configuration or at Astra, as the timing slide was not scanned a sufficient distance in those situations to look for the effect.

The sources of both sets of secondary peaks is unknown. One possibility is a reflection from two uncoated surfaces somewhere in the optics. However, the surfaces would have to be 0.065 mm or 2.3 mm apart; these distances are not thought to appear anywhere in the system. Pre-pulses from either the oscillator or regenerative amplifier cavities would occur with a separation equal to double the cavity lengths; these distances are too long to explain the signals.

7.3 Pulse train gallery

Several measurements of pulse trains are given in the figures 7.5, 7.6, and 7.7. The inter-pulse spacing in the train was found to agree with the value predicted from the tabulated birefringence of calcite to better than 4%. The scan from Astra has a notably better peak-to-valley contrast than Oxford scans of equivalent pulse spacing due to the shorter pulse duration of the Astra laser system.

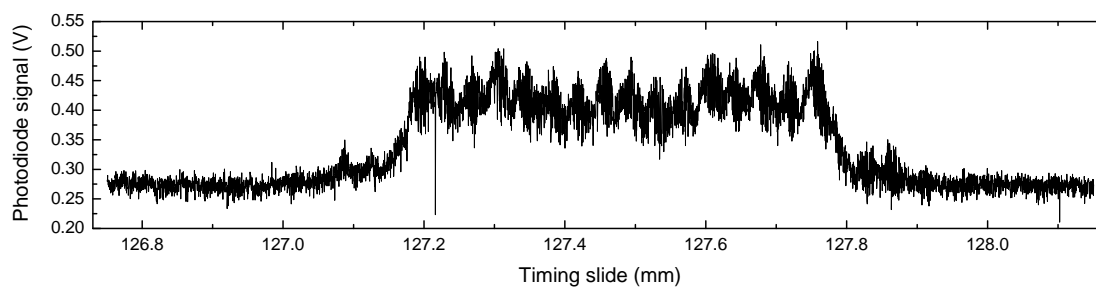


FIGURE 7.6: A burst of 16 pulses at minimum spacing, measured at Oxford.

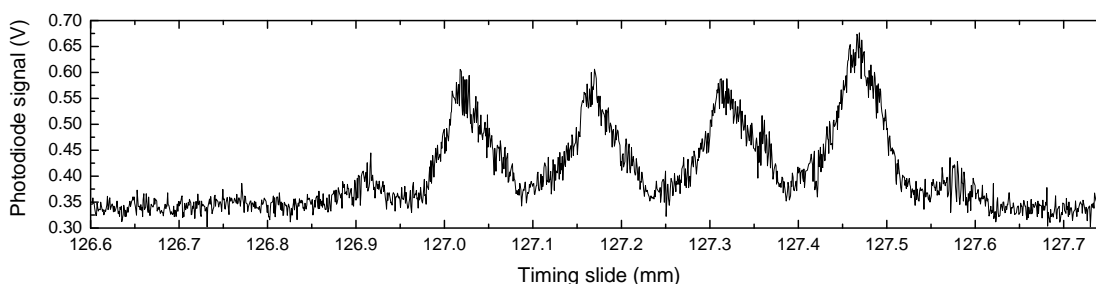


FIGURE 7.7: A train of four pulses at four times the minimum spacing, measured at Oxford. The small satellite peaks are also visible.

7.4 Sensitivity to crystal alignment

The intensity of pulses in the train can vary by 50% from one pulse to the next. This unevenness is likely due to imperfect alignment of the splitting crystal axes relative to the beam polarisation. If a crystal's axes are only imperfectly oriented 45° from the beam polarisation, one of the two sets of pulses exiting the crystal will get more than its 50% share of the energy. The crystal angles are thought to have been aligned to $\pm 1.4^\circ$ at Astra, and to $\pm 0.3^\circ$ at Oxford. By comparing two cross-correlation scans in which no optics were touched in between (figure 7.8.a-b), it can be seen that shot-to-shot variation is non-zero but smaller than to the overall variation within the pulse train. By randomising the crystal orientations and then returning them to nominally the same angles (figure 7.8.c), it is indeed apparent that much of the intensity variation can be explained by imperfect crystal alignment. Whether or not this level of variation is acceptable depends on how sensitive HHG extinction is to the intensity of the counter-propagating light in the relevant parameter regime.

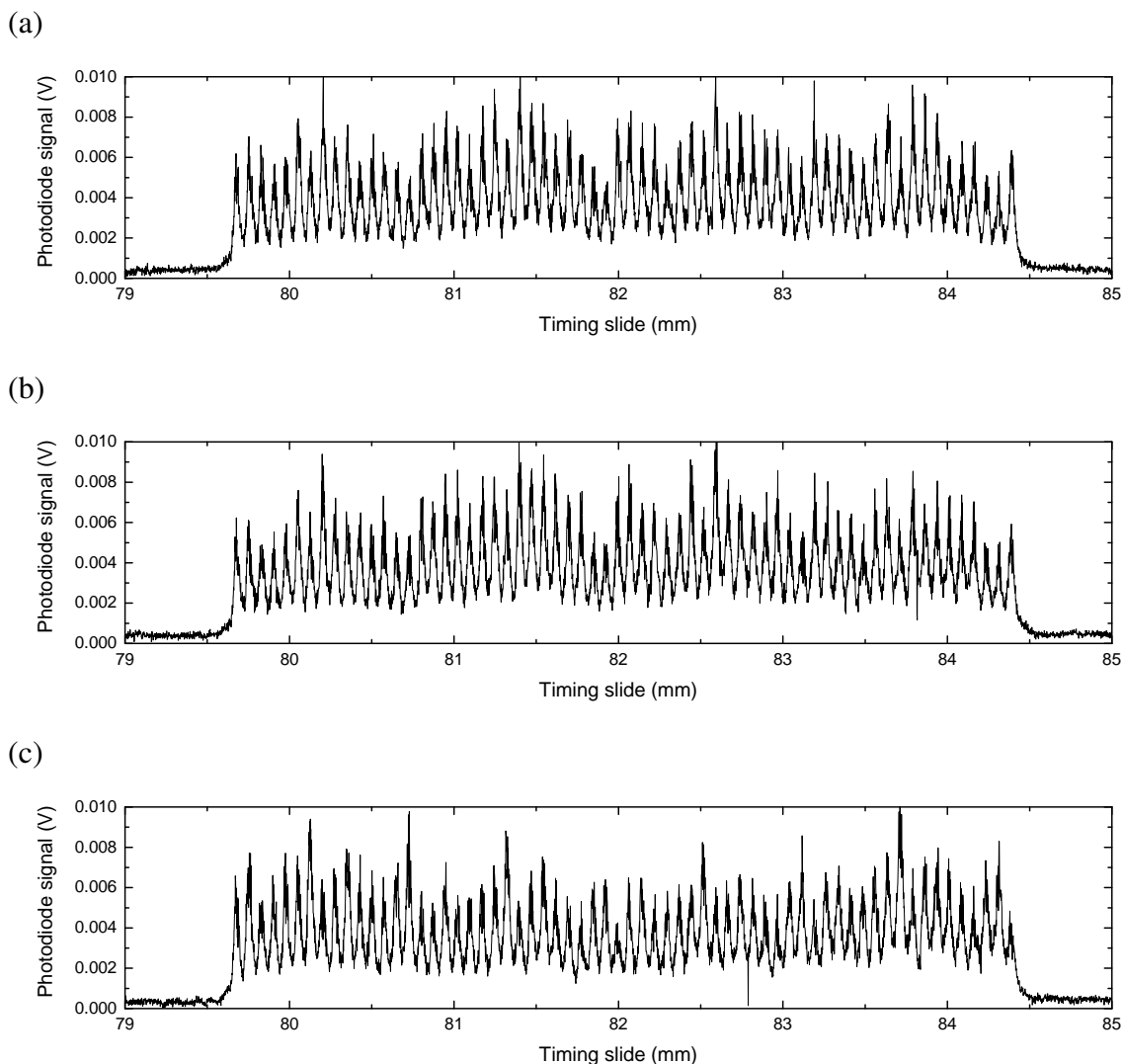


FIGURE 7.8: (a) Typical train of 64 pulses (at four times the minimum possible spacing), showing variations in peak height. (b) A second scan with no intermediate realignment, showing minor differences from (a). The crystals were rotated randomly and then realigned, yielding (c).

7.5 Summary of findings

- Cross-correlation measurements from Astra and Oxford confirm that the N -crystal method can reliably produce trains of pulses of a desired length. The inter-pulse spacing of the train is within 4% of the predicted value, though the intensity may vary by a factor of 2 from one pulse to the next when the crystal angles are set by eye.
- Preliminary measurements suggest that the 1-crystal method also produces a pulse train, but that the pulse spacing varies significantly from beginning to end of the train.

- There is uncertainty by a factor of 5 in the pulse duration for some data from Oxford.

CHAPTER 8

Astra experiments

Although the experiments at Astra confirmed that the pulse-splitting scheme worked well, many other questions were raised related to high harmonic generation. The counter-propagating beam (CPB) was never found to have a reproducible effect on the harmonic spectrum, and the cause of this failure is uncertain. Furthermore, several unusual spectra were taken. The data is now reviewed in detail.

8.1 Alignment sensitivity

The Astra experiment suffered from unstable laser pointing. The laser's pointing was found to drift on a ≈ 10 minute time scale, and such that the focus moved transversely by amounts comparable to a spot size. Movement of the focal spot by this distance dramatically reduces the coupling of the laser into the capillary. Additional pointing control was arranged from the Astra laser operators so the beam could be manually stabilised; this helped but did not eliminate the problem. Figure 8.1 shows the variation in high harmonic signal over a scan of timing slide position after the manual stabilisation was introduced. As the CPB is off, there should be no change in signal. Nonetheless, the variation is large compared to the signal. Since the timing slide is the driver arm, it is unclear whether this variation is caused by the slide motion or by the laser. Unfortunately, no long sequence of shots was taken with the timing slide fixed for comparison.

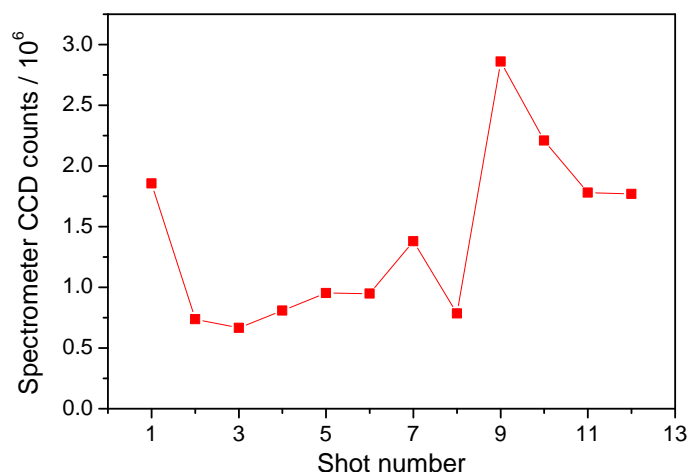


FIGURE 8.1: Variation in signal strength for the $q=25$ harmonic as the timing slide was moved over a total of 1 cm. No CPB was used, and all other parameters were fixed.

8.2 Energy scans

It is nearly impossible to be certain of the experimental parameters inside the capillary, especially as they vary dramatically with time and space. A particular level of ionisation is required for the dephasing length to match the pulse train period, and it is hard to precisely predict the driver energy needed to create this level of ionisation at the correct point in the pulse. Consequently, most data from the Astra campaign consisted of driver energy scans. It was hoped that a small number of harmonics would grow bright and then dim as the driver energy was scanned through the optimal value for QPM, a value which could only roughly be predicted in advance. However, this signature behaviour of QPM was never observed. Figure 8.2 shows the results of some typical scans. Data when both driver and CPB were active were essentially a sum of the driver-only and CPB-only data, with no conclusive sign of interaction.

As the figure shows, line emission was created from CPB energy that hit the capillary glass rather than the central channel. For 127 micron-diameter capillaries, this line emission was typically somewhat brighter than the harmonic emission. One other capillary diameter was used – 178 microns – and for this size the line emission was generally still present but less intense than the harmonics.

Scans were performed for several pulse train configurations, illustrated in figure 8.3. In

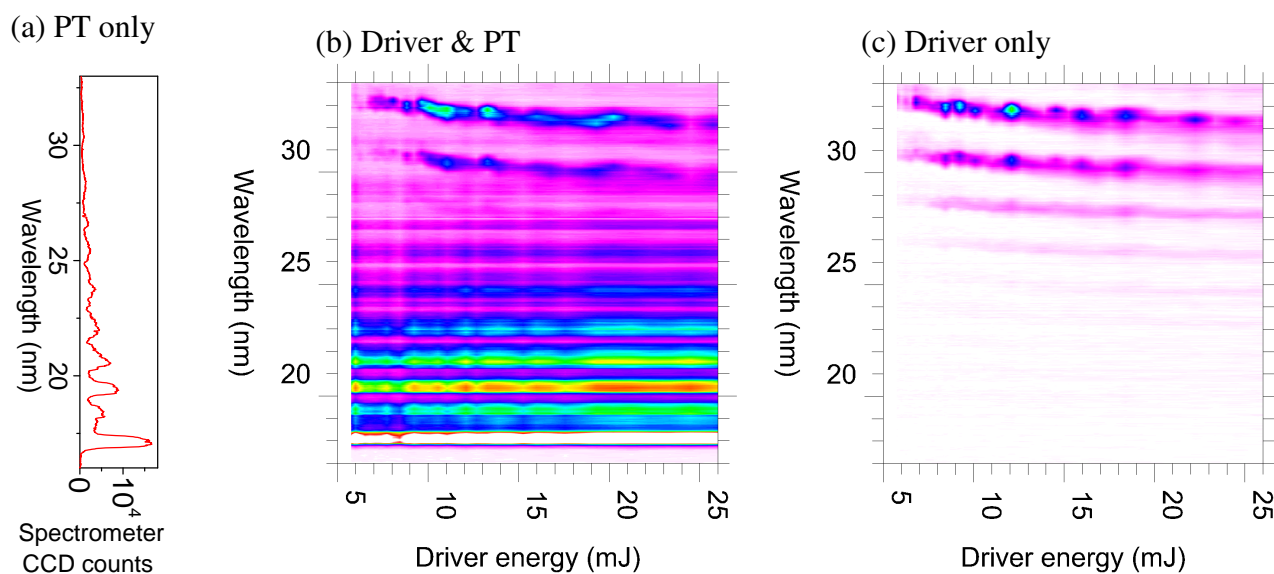


FIGURE 8.2: Typical attempt to find QPM conditions by scanning driver energy. When both driver and counter-propagating beams were active (b), the result was always the same as that which would obtain if the line emission from the CPB (a) were simply added to the driver-only case (c). Although some adjacent driver energies in (b) result in very different harmonic signals, this “enhancement” is unlikely to be due to the CPB, as variability of similar magnitude exists when the CPB is blocked (c). (b) and (c) are plotted with identical colourmaps. Data for a 127 micron-diameter capillary is shown here; a 178 micron-diameter capillary produced significantly less line emission and shot-to-shot variability.

the “fine” configuration, the full 128 pulse capability was used. In the “coarse” arrangements, the thinnest two crystals were disabled, reducing the number of pulses by four. For this latter configuration, the duty cycle was brought closer to 1:1 by adding an 80 mm block of BK7 glass to the CPB optics, stretching the pulses. The fine pulse train, containing more QPM zones, would have produced the larger rise in signal upon achieving QPM. There was worry however that excessive pressure would be required to match Δk to the short period of this train. The coarse trains, having a longer period, would have required less pressure. There was also concern that the pulse train intensity may have been insufficient. Consequently, a coarse train of half the number of pulses – and therefore with up to twice the intensity – was also used.

Scans were also taken for several timing slide positions, for different gas pressures, for both parallel and perpendicular polarisation configurations, for several pulse train energies, and for multiple capillary lengths and diameters. In no case did the pulse train have a reproducible effect on the harmonics. For a given harmonic order and driver energy, the signal strength did vary by a factor of ≈ 20 as these other parameters were varied. Much of this variability was likely due

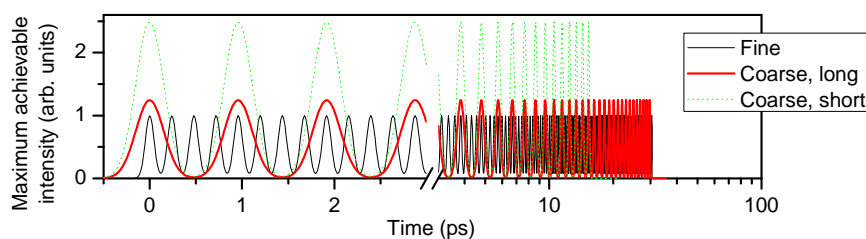


FIGURE 8.3: Three pulse trains used at Astra. Curves are computed based on the 111 fs full-width at half-maximum intensity (FWHMI) duration measured by cross-correlation.

to the finite lifetime of the capillary, as counts generally decreased from one scan to the next for a given target, and the capillaries showed visible wear upon removal. Other variability, such as that between consecutive shots within a scan, is best explained by fluctuations in laser energy or pointing.

8.3 Dependence on timing

Perhaps unfortunately, no high-resolution scans of the timing slide were carried out, as driver energy was always the variable scanned at a high resolution. However data from different energy scans, each carried out at a different timing slide position, can be combined. Results for several conditions are shown in figure 8.4. The data are very noisy, as one might have expected from the CPB-free timing scan of figure 8.1. The trend seems different for different conditions, and in all cases the variation is no greater than that when the CPB is off (so no timing dependence should exist at all). Based on the trend shown for perpendicular polarisations – smaller signal when the pulse train arrived at the capillary first – it was hypothesised that the CPB may leave the gas ionised and therefore less able to efficiently generate harmonics. However, this trend was not reproducible.

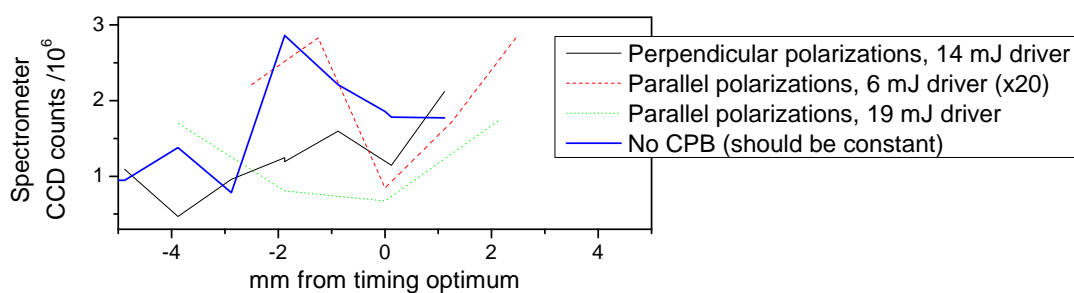


FIGURE 8.4: Scans of timing slide position. Zero on the horizontal axis corresponds to the driver meeting the centre of the pulse train in the centre of the capillary. Positive values correspond to the pulse train reaching the capillary first.

8.4 Discussion

Even given the noise in the data, it is unclear why the CPB did not have a dramatic effect on the data. This is especially true given the unambiguous and reproducible effects observed at Oxford and reported in the next chapter.

Was the energy in the CPB sufficient to have an effect? From the methods of chapter 5, and given the pulse lengths used for the driver and CPB, one can calculate the CPB-to-driver energy ratio needed to produce extinction. For $q=25$, parallel polarisation mode, and the short coarse pulse train, extinction should occur from the direct phase modulation mechanism when the CPB energy is at least half that of the driver. The intensity-dependent phase modulation requires many times less CPB energy. For perpendicular polarisation mode a factor of 12 times more energy is required in the CPB. For the long coarse pulse train or the fine train, another factor of 2.5 more CPB energy is needed. Though the CPB energy may have been insufficient in some scans, it would have greatly exceeded the predicted threshold in others. For example, in the scan shown in figure 8.2, the CPB was more than the predicted necessary energy for even the highest driver energies shown. For lower driver energies in the figure the energy ratio becomes still more favourable.

Although harmonic generation was not successfully manipulated with the CPB, there were several other features of interest in the data. Two such features are now discussed in detail.

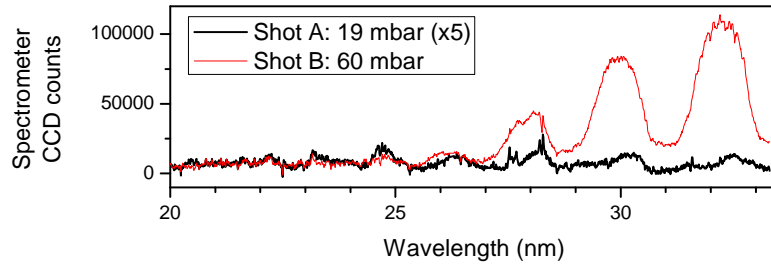


FIGURE 8.5: Consecutive shots showing a dramatic increase in signal. For both shots, argon is used, the CPB is off, and the driver beam is 19 mJ. It is uncertain from records whether the capillary alignment was manually adjusted between the shots. Note that shot A has been multiplied by 5.

8.5 Low- q enhancement

One surprising sequence of shots, illustrative of the dramatic variability in HHG signal observed at Astra, is shown in figure 8.5. Between the shots the pressure was increased by 3. Simultaneously, the signal for $q=25$ increases by more than 40. Unfortunately, these shots were not examined closely during the experiment, so the pressure was not reduced to the initial level to see if the signal would decline to its original value. As HHG is a coherent process, the harmonic intensity scales as the number of emitters squared (ignoring phase-matching effects), and hence as the pressure squared. This normal pressure scaling can therefore not account for the observed increase in signal.

Was the explanation that $\Delta k = 0$ phase matching had occurred at the high pressure but not at the low pressure? This possibility is supported by the fact that the ratio of signals between the two plotted shots depends strongly on the harmonic order q , the enhancement being much greater for $q = 25$ than for $q > 29$. From equation 4.34, it can be calculated that an ionisation fraction Z of 0.044 is required for phase matching of the $q=25$ harmonic at 60 mbar, and $Z=0.016$ to phase match at 19 mbar. Given the driver pulse energy, duration, and focusing geometry, and assuming a $1.5\times$ diffraction-limited Airy focus, the peak intensity of the shots is computed to be 1.2×10^{16} W/cm². This intensity is enough to multiply-ionise the gas, as shown in figure 8.6, so Δk will swing through 0 on the rising edge of the pulse for either pressure. From a simulation of the ADK rates for a 41 fs pulse with peak intensity 1.2×10^{16} W/cm², it can be concluded that the intensity at the time of $\Delta k = 0$ is 2.2×10^{14} W/cm² for the low pressure,

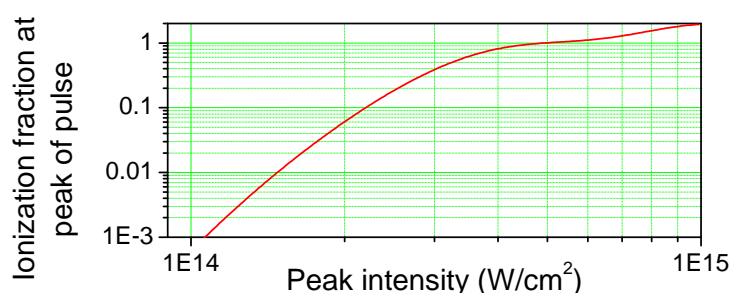


FIGURE 8.6: Ionisation fraction at the peak of a 41 fs FWHMI pulse in argon, as calculated from equation 2.7.

and 2.7×10^{14} W/cm² for the high pressure. In either case, the intensity is sufficient to produce the $q=25$ harmonic. Therefore, phase matching should occur for the harmonic at *both* pressures. Phase matching does not seem able to explain why the spectrum should differ so much from 19 to 60 mbar.

An attempt was made to reproduce the effect of figure 8.5 at the Oxford laser in the configuration of figure 6.5.a, before the laboratory was converted to the CPB configuration. A computer-controlled mass-flow controller was obtained for the Oxford laboratory, and this enabled high-resolution automated pressure scans, which were not possible at Astra. Figure 8.7.a shows a typical Oxford scan. At most, a factor of ~ 2 increase in signal was observed as the pressure rose from 19 to 60 mbar, never the factor of ~ 43 observed at Astra. An attempt was made to keep the spot size and capillary design as close as possible to those used for the Astra shots. Scans were also performed for other pulse energies and spot sizes, but these scans always closely resembled the one shown in figure 8.7. Interestingly, the Oxford scans never came close to the signal strength of the “enhanced” Astra shot. Integrating counts over both dimensions of the CCD, it was typical at Oxford to see 1/70 of the Astra signal per shot for a given harmonic order. It is possible that this difference is due to the fact that different spectrographs, filters, and CCDs were used for the two experiments. However, all were of almost identical design.

In the Oxford experiments, the pressure was scanned from zero to a maximum and then back down to zero. For some scans there was up to a factor of 3 difference in signal for a given pressure from the first to the second half of the scan, as shown in figure 8.7.b. For some scans the signal was higher on the rising phase; for others it was higher on the falling phase. In other scans,

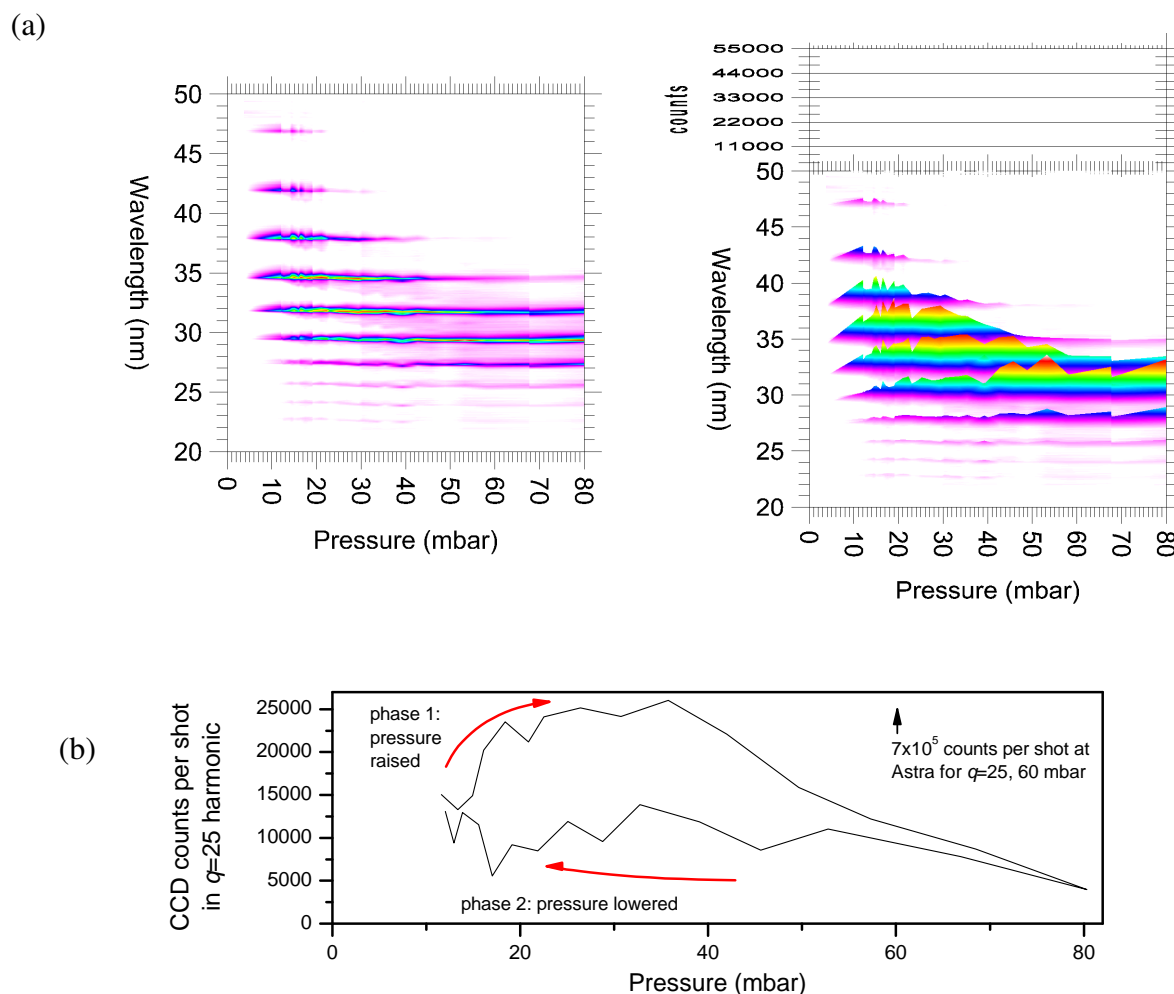


FIGURE 8.7: Failure at Oxford to reproduce the strong pressure-dependence seen at Astra. (a) Hysteresis-free scan, showing typical variation of harmonic signal with pressure. (b) Typical high-hysteresis Oxford scan.

such as that shown in figure 8.7.a, there was virtually no such hysteresis. The degree and sign of the hysteresis seemed unrelated to experimental parameters such as laser energy, as hysteresis was sometimes dramatically different for scans taken under apparently identical conditions. The best explanation seems to be that alignment of the laser, pointing optics, or capillary drifted over the 10-25 minutes required for the scan. This conclusion further reinforces the point of figure 8.1, that harmonic generation in capillaries is prohibitively sensitive to alignment.

It is unclear why the Oxford results differed from the Astra results to such a degree. An aperture was used to make the spot size of the Oxford experiment more closely match that of Astra, and aperturing the beam can have large effects on harmonic generation [105]. Also, the pulse length at Oxford was unavoidably somewhat longer than that of Astra (55 vs. 41 fs).

Perhaps another contributing factor to the jump in signal at Astra was that there was debris in the bore of the capillary for the low-signal shots. These shots were the first three taken after the capillary was inserted into the experiment. It may be that the clearing of such debris coincided with the change to higher pressure; perhaps the increased gas flow helped to flush the channel. Later experience with grazing-incidence guiding at Oxford supports the idea that machining of the gas holes leaves debris in the capillaries, and that transmission may abruptly rise several shots into use as the blockage is vaporised by the laser.

8.6 High- q enhancement

The most striking data taken at Astra were two consecutive spectra which seem to show intense SXR radiation at $\lambda < 5$ nm, shown in figure 8.8. This radiation is of far shorter wavelength than that recorded at other times during the experiment. Although only one other shot was taken with the spectrograph looking at $\lambda < 13$ nm, the signal in figure 8.8 is unlikely to be spurious scatter, for this third shot recorded 17.1 nm line emission from the CPB but no signal at 4 nm. The significance of the 4 nm shots was not appreciated until after the experiment, so it was not possible to experiment with the effect. The shots were taken with 4.3 mJ in the driver, with no CPB, and with 20 mbar argon in a 178 micron-diameter, 15 mm-long capillary. Due to a miscommunication with the target fabrication facility, an unusual 0.3 micron CH + 0.2 micron Al light-blocking filter was used. A confidence interval for the efficiency of conversion into each harmonic order near 4 nm is $[5 \times 10^{-7}, 3 \times 10^{-5}]$, values which are extremely high for harmonics of this order. For comparison, per-harmonic conversion efficiencies for previous reports of water window harmonic generation have been estimated at 10^{-11} or less [28, 106, 107].

Could $\Delta k = 0$ phase matching be responsible? For the cutoff to extend to sufficiently short wavelengths, the intensity must have been $\gtrsim 1.6 \times 10^{15}$ W/cm² at the time these high order harmonics were produced. From figure 8.6, it can be seen that the ionisation fraction will exceed 2 at the pulse peak for these intensities. Plugging numbers into equation 4.34 then, it can be seen that the dephasing length will be no more than 13 microns. Due to the large phase mismatch, harmonic generation should have been limited to this tiny length, which is too short

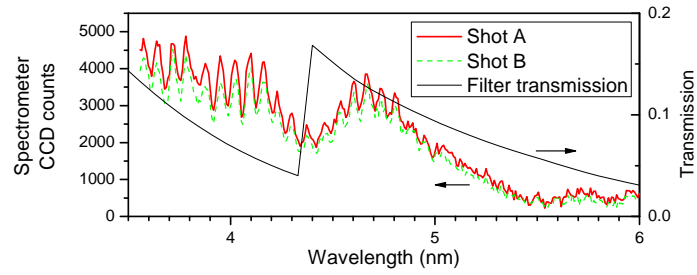


FIGURE 8.8: The two shots in which water-window radiation was observed. The filter transmission curve is based on tabulated opacities, and the transmission drop at 4.4 nm corresponds to the carbon K-edge. According to the calibration, the leftmost harmonic above corresponds to $q=207$.

to explain the magnitude of the observed signal.

8.6.1 Mode beating

The possibility was considered that beating between capillary modes (see section 3.3) could have caused a form of quasi phase matching, as follows. Most of the harmonic generation would occur at the locations where the beats resulted in constructive rather than destructive interference. The beating would modulate HHG, even without any counter-propagating beam. For the case where only two modes are excited, as shown by one of the traces in figure 8.10, intensity maxima occur at regular intervals. If the periodicity of these maxima is equal to two dephasing lengths, quasi phase matching would occur. The possibility of QPM by beating between capillary mode was suggested previously by Christov *et al.*[87].

To consider whether this scheme is at all reasonable for more realistic distributions of mode energies, the intensity beating pattern was calculated for several input pattern of light at the capillary entrance, each a reasonable model for the experimental conditions:

1. The Airy pattern formed from the Astra beam diameter and focusing lens, assuming a tophat near-field and diffraction-limited focusing,
2. an Airy spot with radius $1.5 \times$ that of (1),
3. a Gaussian with FWHMI equal to the FWHMI of (1) ($w_0/a=0.21$), and
4. a Gaussian with FWHMI equal to the FWHMI of (2) ($w_0/a=0.32$).

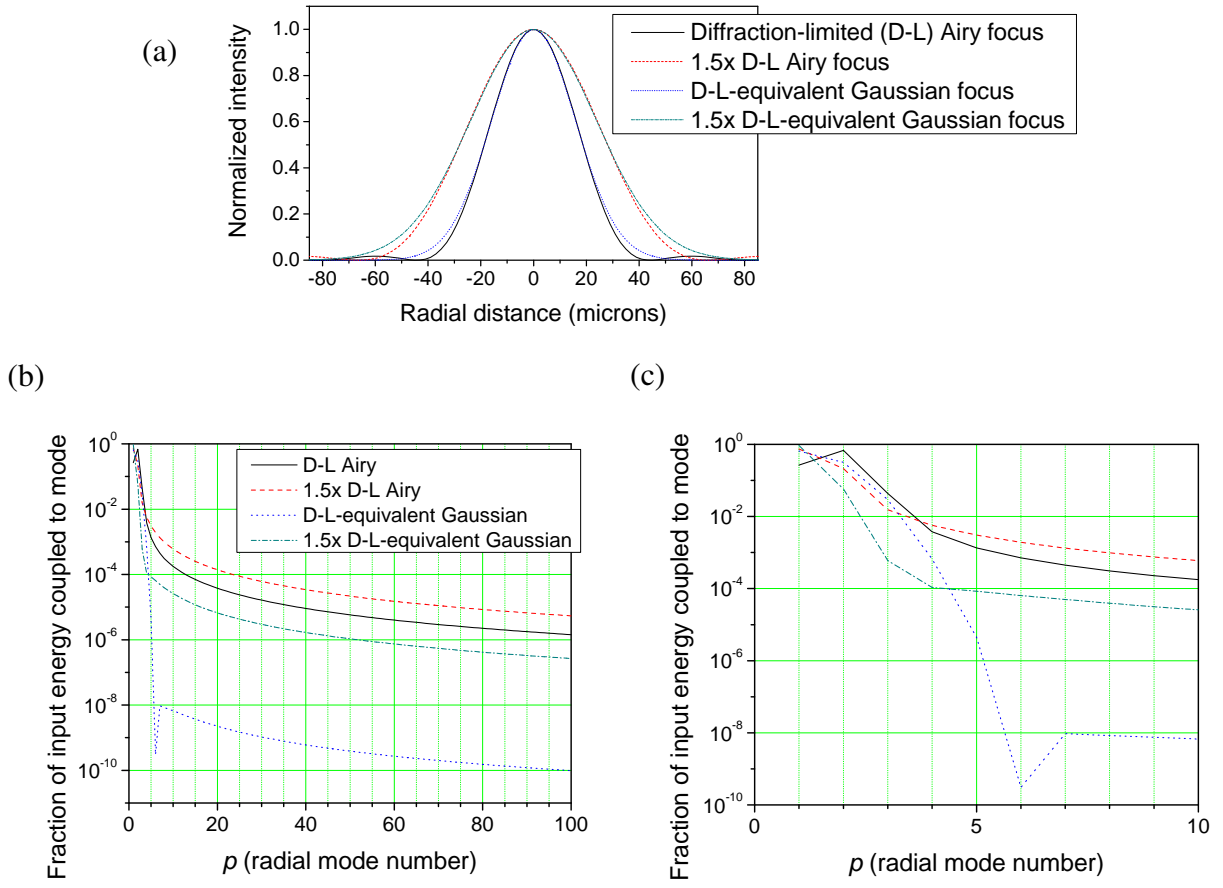


FIGURE 8.9: (a) Focal spots at the capillary entrance considered for the calculation of mode beating. (b)-(c) Fraction of incident energy coupled to each mode for these input spots.

These distributions are illustrated in figure 8.9, together with the C_p^2 mode couplings calculated from equation 3.5. The axial intensity patterns that result, calculated from equation 3.6, are shown in figure 8.10. The patterns are so irregular and sensitive to the input spot shape that robust QPM seems unlikely.

Several characteristics of these numerical results are worth noting. First, in figure 8.9.b-c, it can be seen that the Airy input spots deposit more energy in the high order modes compared to the Gaussian input spots. This is a result of the larger amount of energy in the wings of the Airy pattern. Secondly, figure 8.9 shows calculations for both the first 15 and the first 100 $PIP_{0,p}$ modes so the sensitivity of the calculation to the number of modes included. For the first few millimetres of propagation the calculation is indeed sensitive to this number, particularly for the $1.5\times$ diffraction-limited Airy result. However, the calculation beyond ~ 2 mm is more

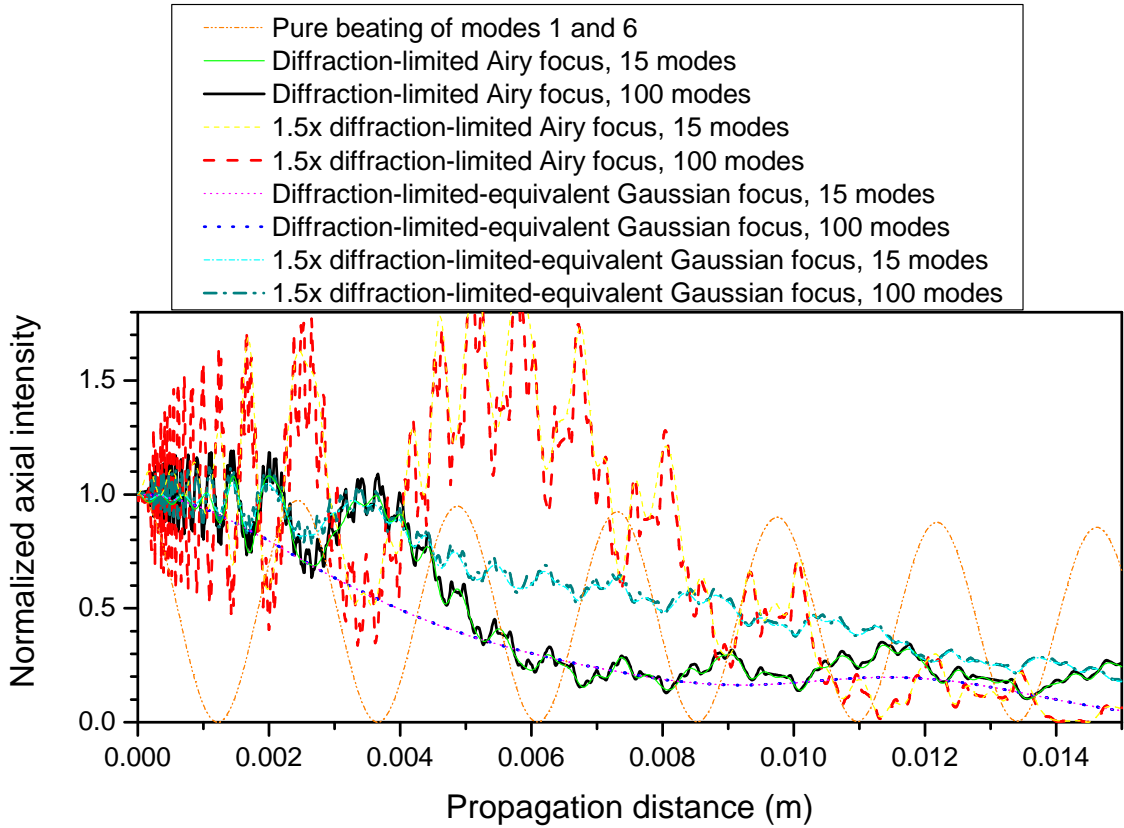


FIGURE 8.10: Beating between capillary modes, calculated for conditions in which the water window harmonics were seen.

trustworthy because the high order modes quickly decay. The modes $p > 39$, for example, have decayed to $1/e^2$ intensity after 2 mm.

Besides the irregularity of the intensity pattern, there are further problems with the theory that mode beating gave rise to QPM. One such problem relates to the intensity dependence of the single atom phase (section 2.1.1). Even if the beat maxima did occur at regular positions, if the maxima were not of identical intensity they would not lead to perfectly constructive interference. The maximum tolerable intensity variation among the beat maxima can be calculated from equation 2.4. If a variation of up to π in phase is allowed, the tolerable intensity variation is found to be $\Delta I = 1.3 \times 10^{13} \text{ W/cm}^2$, less than 1% of the $1.6 \times 10^{15} \text{ W/cm}^2$ threshold intensity for creating harmonics of this order. Thus, harmonics from different beat maxima will almost certainly add out of phase. This tolerance to the variability is tight indeed.

There is one more potential problem with the mode beating explanation. The position-

dependent intensity will give rise to a position-dependent ionisation, and therefore a position-dependent Δk . A 1D model for harmonic wave growth in this case of position-dependent dispersion was given in equation 4.21. From that expression it can be seen that for constructive addition of the harmonics from the various beat maxima, $\int \Delta k(z) dz$ between the maxima¹ must be a multiple of 2π . In other words, the growing harmonic wave must pick up a multiple of 2π in phase as it travels from one emission location to the next. However, the very irregular spatial pattern of Δk (following from the irregular pockets of ionisation) means that this integral will differ from one beat period to the next. If this variation is sufficient, emission from the various beat maxima would add out of phase.

Though it seems unlikely that harmonics were emitted in phase from regularly spaced locations, it may be possible that the total harmonic emission could still exceed that from a similar gas jet experiment (in which the intensity varied more smoothly). In a random walk, many small steps in random directions lead to sizeable net displacement. Similarly, the many out-of-phase harmonic emission locations may lead to a sizeable overall signal. Coherence of the resulting emission would likely be reduced relative to HHG in gas jets. However, this prediction is at odds with experimental measurements of coherence[67]. Further work is needed to explore whether this “random walk” harmonic generation should be significant and observable.

8.7 Summary of findings

- The CPB was never seen to have an effect on harmonic generation at Astra.
- Spectra taken at Astra showed much variability. This was likely the result of drift in laser pointing and energy, and of the finite capillary lifetime.
- Harmonics were seen in the water window ($\lambda < 4.4$ nm), produced with a very high efficiency ($> 5 \times 10^{-7}$.) Phase matching does not seem able to explain the observation.
- Capillary mode beating is surmised to affect this and the many other experiments with HHG in capillaries. Mode beating will likely result in spatially nonuniform intensity, with

¹This is the generalisation of quasi phase matching for position *independent* Δk where it is rather $\Delta k z$ that must be a multiple of 2π over the modulation period.

smaller-scale and larger-amplitude intensity variations than exist for HHG experiments which do not use waveguides. If the single-atom phase varies as strongly with intensity as theory suggests, these intensity variations will significantly affect phase matching and quasi phase matching of HHG. The spatial variations in Δk which result from the intensity variations may also be significant. None of these elements has been considered in the major recent papers regarding HHG in capillaries [8, 57, 65, 66, 85].

CHAPTER 9

Oxford experiments

The experiment was recreated at Oxford for a campaign in early 2006. Based on the results of the Astra experiments, it was expected that a long and narrow waveguide would be necessary. Such a design, it was hoped, would result in a uniform intensity throughout the region in which harmonics were generated. However, formidable problems were encountered while trying to guide in such capillaries. Eventually gas cell targets were explored as well. Though in this geometry there will only ever be a short (~ 1 mm) region in which the intensity is close to its peak value, it was hoped that there would be enough dephasing lengths in this distance to see quasi phase matching effects. Extinction of HHG in the gas cell was very reproducible, as was a very modest enhancement effect.

9.1 Harmonic generation in capillaries

9.1.1 Capillary design

There were two principal capillary dimensions to determine: the inner diameter and the length. In selecting values for these parameters there were many considerations.

First, the focal spot size was already constrained to be close to 27 microns ($1/e^2$ intensity radius). This value followed from the bounds on beam diameter and the focal length of the focusing optics. The beam diameter was constrained from below by the need to reduce fluence

Capillary diameter (microns):

102						76							
		radial mode number							radial mode number				
		1	2	3	4	5			1	2	3	4	5
azimuthal	mode	0	487	92	37	20	12	0	201	38	16	8	5
number	1	192	57	27	16	10	1	79	24	11	7	4	4
	2	107	40	21	13	9	2	44	16	9	5	4	4
	3	69	30	17	11	7	3	29	12	7	4	3	3

Fractional reduction in 1,1 mode relative to
0,1 mode after 90 mm of propagation:

0.752

0.503

TABLE 9.1: Lengths for a drop to $1/e$ of initial intensity for modes in two capillary diameters.

below damage thresholds. The diameter was also constrained from above by the apertures of the optics (which were in turn constrained by the increasing cost of larger optics). The beam diameter could have been changed using a lens pair in the vacuum chambers, but these chambers were already crowded with other optics. The focal length was constrained by the need to fit the lens into the vacuum chamber within a specified area, and also by the focal lengths stocked by manufacturers. A focused spot size of 27 microns would be matched to a capillary of inner diameter 84 microns.

At Astra it had been markedly more difficult to guide in 127 micron capillaries than in 178 micron capillaries. This experience was with pieces that were only 7 mm long. It was planned to use much longer capillaries for the Oxford experiment to maximise the damping of high-order modes. Consequently, it was feared (correctly, it turned out) that guiding in diameters smaller than 127 microns would prove a challenge.

The next consideration was that only certain inner diameters were available from the capillary manufacturer: 26, 52, 76, 102, 127, 152, and 178 microns. Thus, 76 and 102 microns were logical options for the capillary diameter.

Next, it was desired to have as much damping of high-order modes as possible. From equation 3.3, the mode loss lengths of a capillary of diameter a scale as a^3 . Thus, smaller capillary diameters are much better for such damping. Table 9.1 shows the $1/e$ intensity loss lengths for the first few modes in the capillaries suggested above. This table suggests that either capillaries of several tens of centimetres should be used, or else the capillary diameter and spot size should be further reduced. The reasons for not taking the latter option have already been discussed.

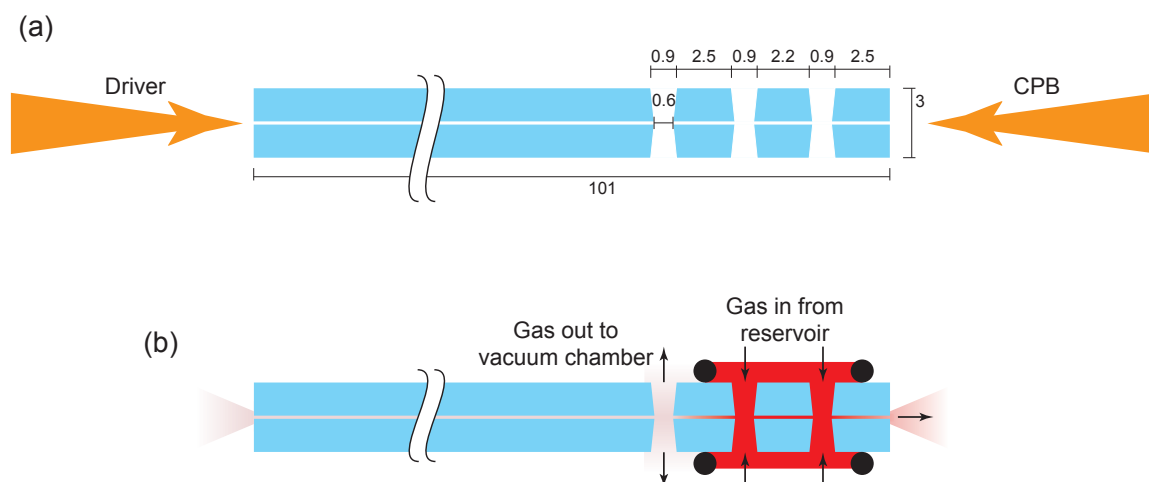


FIGURE 9.1: Capillary design used for results reported in this chapter. (a) Dimensions in mm. (b) O-ring system and pressure around capillary. Arrows indicate gas flow.

There was worry, however, about using capillaries much longer than 10 cm. There was already the challenge of guiding in capillaries of small diameter, diameters smaller than those with which our group had experience. A 10 cm waveguide length would be far longer than our group had used for wider (e.g. 200 micron diameter) capillaries. The longest reported capillary used for HHG was 10 cm [67], and that experiment used large 150 micron inner diameter channels. Channels of longer than 10 cm would also make it difficult to fit the required optics into the vacuum chambers. Due to these considerations, it was primarily 10 cm capillaries which were used (actually 101 mm, for an unimportant historical reason).

Figure 9.1 shows the placement of the gas entry and exit holes. The distances of 2.5 mm were made as small as possible, given the need for the o-ring seal between gas and vacuum zones. This minimisation ensured that the laser interacted to the greatest extent possible with either vacuum or the central constant density, and no intermediate values. Capillaries with a longer constant-pressure zone were used in addition to the design shown here, but all capillary data reported in this chapter happened to come from this design. The gas holes were placed near the exit of the driver beam since spatial filtering was expected to be more essential for the driver than for the pulse train.

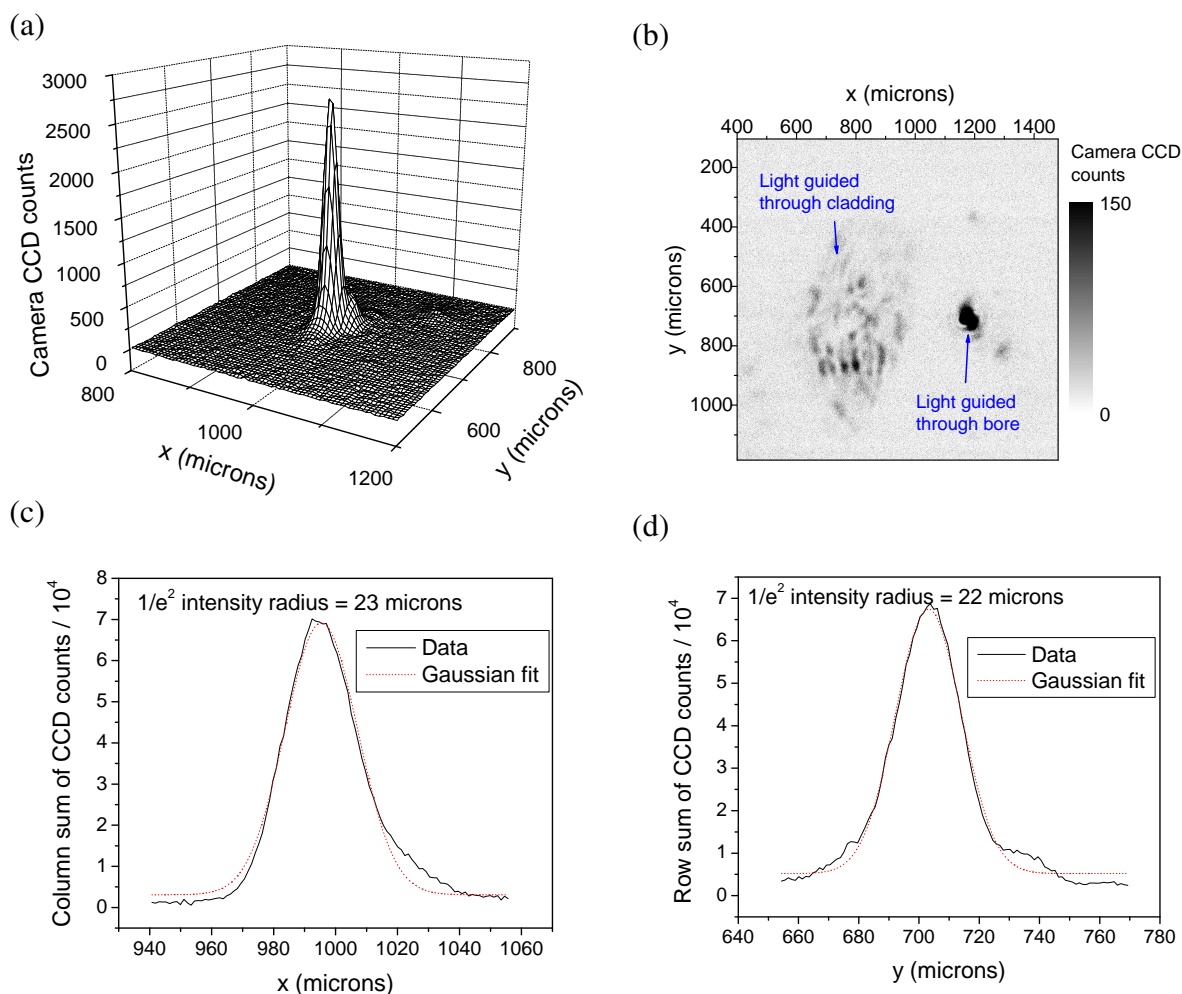


FIGURE 9.2: The capillary exit plane was relay imaged onto a CCD camera. The transmitted mode is shown in (a). In (b), light guided through the glass cladding can be seen. (c) and (d) graph the row- and column sums near the focus, showing an output mode in close agreement with theory.

9.1.2 Guiding

In the first attempts guiding in these 76 and 102 micron diameter, 101 mm long capillaries, no light was seen to come through the channel for either the driver or the counter-propagating beam (CPB). Guiding in both directions was observed in 178 micron capillaries, and also in 76 and 102 micron capillaries in which the radial gas holes had not been machined. This led us to conclude that a prohibitive amount of debris was blown into the channel during machining of the gas holes. Flushing of the channel with pressurised air was tried, but this did not seem to clear the blockage. Attempts to drill away the debris with the laser also failed: no guided light was observed even after drilling until the channel ends were destroyed.

The machining protocol was then modified so the gas holes were only bored just up to – and not through – the central capillary channel. The last ~ 100 microns of glass were punched out with a sewing needle. Using a microscope, it was apparent that this method produced much less debris in the capillary. Guiding was still not immediately possible, even after flushing out the channel with a pressurised air line for several minutes. However, with several seconds of firing by the driver and counter-propagating beams, guided light suddenly appeared as the last debris was vaporised.

Nonetheless, the transmission of these capillaries was never adequate. In one measurement using a 76 micron capillary, the fractional transmission of the driver beam was found to be 1%, though due to saturation of the output energy diode the actual value may have been somewhat higher. In another measurement of the same capillary, the driver transmission was found to be 3%, and that of the CPB was calculated at 7%. For all of these measurements, gas entry holes had been machined in the capillaries, but no gas was being supplied (so the capillary bore was at vacuum.) Many unresolved problems were experienced with the photodiodes used to calculate transmission, particularly the measurement of a significant voltage from the photodiode even when the associated laser path was blocked. Because of these problems, more plentiful measurements of capillary transmission do not exist. It is likely that each diode measured light from stray sources in addition to the intended light, so the values of 1%-7% transmission mentioned above should be interpreted with caution. However, it is reasonable at least to trust them within a factor of two. No satisfactory quantitative records were taken of transmission through non-machined capillaries.

The transmission values of 1%-7% for an evacuated capillary can be compared with the $>55\%$ reported by Dorchie *et al* for a smaller (70 μm diameter) capillary of almost the same length (83 mm) under similar laser conditions (800 nm, 120 fs pulse focused to 5×10^{14} - 5×10^{16} W/cm^2). One difference between the experiments which likely accounts for some of the discrepancy is that the Dorchie capillaries were unmachined. The machined Oxford capillaries surely had some remaining debris, and the gas holes themselves would cause additional loss. The near-field of the input beam looked highly non-Gaussian (recall the hot spot mentioned in section 6.4.2), so energy was possibly lost in the wings of the focus. Measurements of

transmission in unmachined capillaries and measurements of transmission through pinholes at the laser focus would have provided a more conclusive understanding of the poor guiding.

Figure 9.2 shows images of the transmitted driver beam in the exit plane of a 76 micron capillary. The driver beam, after being guided for 101 mm, emerged nearly Gaussian with a spot size of (according to the calibration) 22-23 microns. For comparison, the theoretical lowest-order mode output, though actually a Bessel function, is very nearly a Gaussian with spot size of 25 microns. It should be noted that the f-number for light collection from the capillary was essentially the same as for focusing, because the driver and CPB focusing lenses were identical, and each was used to collect the transmitted light from the opposite beam. Therefore, the system could not resolve structure much finer than the width of this lowest-order mode.

Images of the CPB after guiding look similar. No results are presented here because there was not time to perform a pixel-to-length calibration for the associated camera.

9.1.3 Harmonic spectra from capillaries

Figure 9.3.a shows the full spectrograph CCD image showing HHG in a 101 mm long capillary, with no CPB. For all exposures, a background exposure of the same duration was recorded and subtracted from the data. One background was used for many subsequent data exposures. In most of the spectra presented in this thesis, counts were binned in the y direction over a small range as shown, then median filtered in the x direction (width=5) to remove bad pixels.

Low laser transmission was only one of several problems experienced with the capillaries. Another was the strong line emission created when the CPB struck the capillary, shown in figure 9.4. Line emission was prohibitive for capillaries of 127 micron diameter and smaller; only above this diameter did the CPB miss the glass sufficiently for the high harmonics to stand out.

9.1.4 Estimation of dephasing length

Even were it not for the line emission, it is likely that the low energy transmission meant that the parameter regime was unsuitable for quasi phase matching. This conclusion is based on an

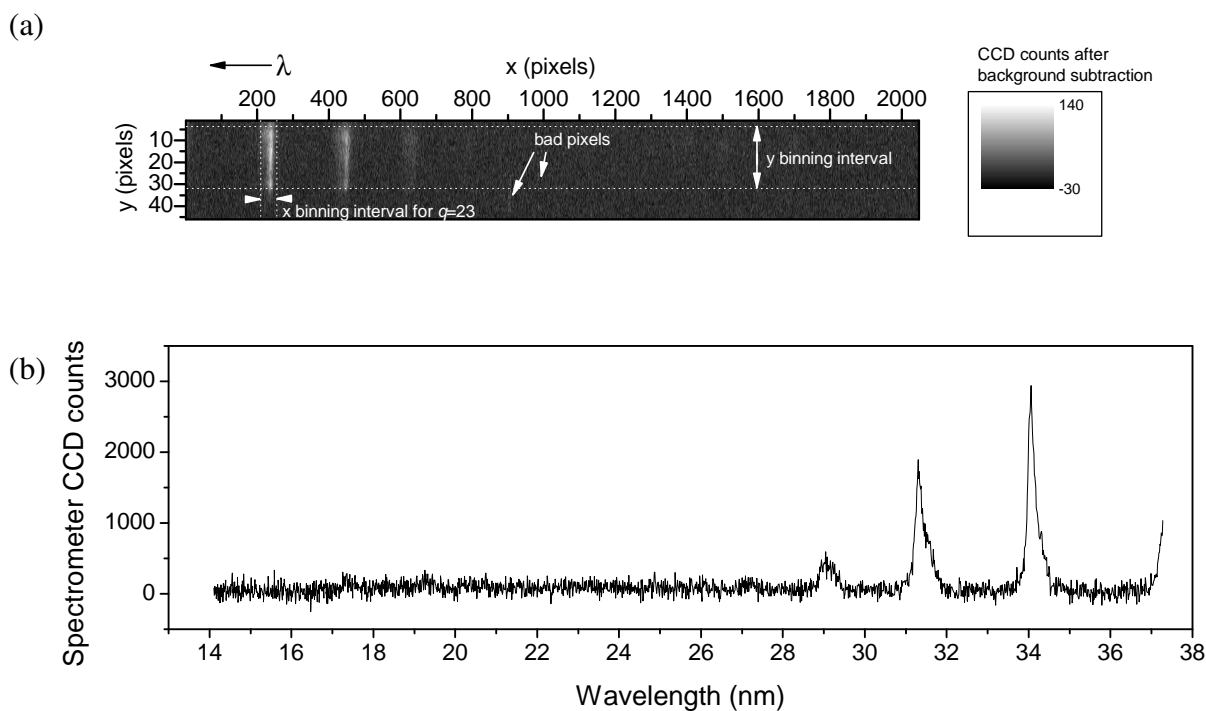


FIGURE 9.3: The most counts and highest-order harmonics observed in a 101 mm long capillary that was narrow enough (102 microns diameter) to significantly damp high-order modes. Data are for 41 mbar argon. No CPB was used. (a) original CCD image; most data presented in this thesis were binned in y but not in x , though in some places each harmonic was individually binned in x as well. The CCD extended for 512 pixels in the y direction, but data were only recorded for the subset shown to reduce CCD download time. (b) Data after binning in y , with the x -axis transformed to wavelength using the calibration of section 6.4.3.

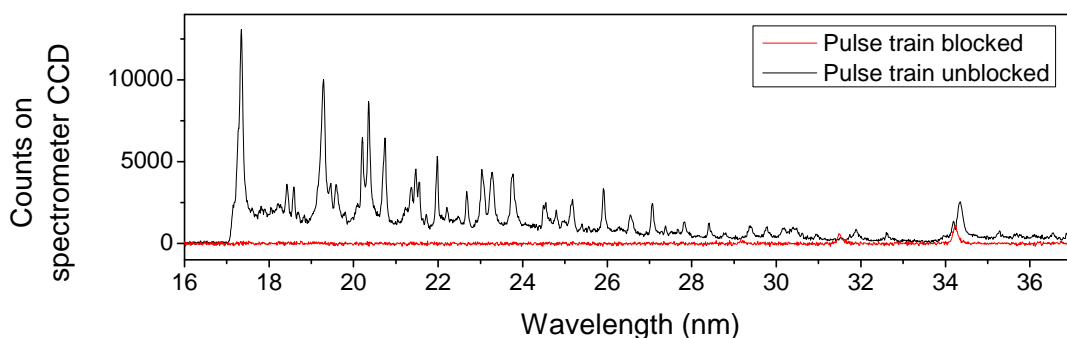


FIGURE 9.4: Harmonic spectra from a 101 mm long, 76 micron diameter capillary, with and without the pulse train. The peak near 34 nm is larger with the pulse train not because of harmonic enhancement, but due to ~ 17 nm line emission appearing in second order.

inference of the dephasing length using two estimates of the maximum intensity in the gas. One estimate is based on the pulse energy, duration, and diameter. For a pulse that is Gaussian in time and space, the peak intensity is given by

$$I = \frac{2U}{\pi w_0^2 \tau} \quad (9.1)$$

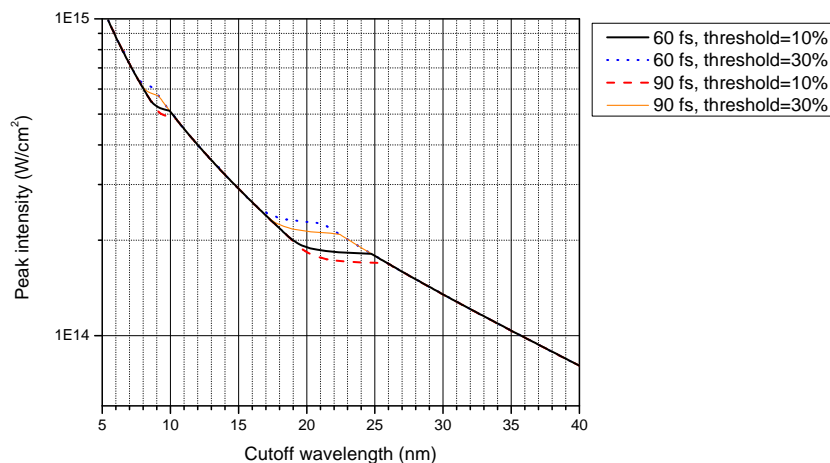
where U is the energy, w_0 is the $1/e^2$ intensity radius, and τ is the FWHMI duration. The exit mode of the capillary is approximately the matched Gaussian, so $w_0 = 0.645 \times$ capillary radius = 25 microns. Using $\tau = 90$ fs and $U = 17$ mJ \times 1-3% transmission yields $I = 2-4 \times 10^{14}$ W/cm².

The peak intensity in the capillary can also be estimated using the location of the harmonic cutoff, as follows. The ADK ionisation rates are integrated for pulses of the experimental pulse duration and of various peak intensity. The maximum order of harmonics produced for one such simulated pulse is then given by equation 2.2, where the ionisation energy and intensity used in this expression are taken to be the values at the pulse peak. From these simulations, the curves shown in figure 9.5 are produced, which allow a mapping from cutoff to peak intensity. The highest observed harmonics in a narrow capillary, as shown in figure 9.3.b, have a cutoff of 28-32 nm. Figure 9.5.b suggests that this cutoff implies an ionisation fraction at the peak of the pulse of 0.007-0.02. Thus, the first ionisation energy is to be used in equation 2.2, and so the peak intensity is likely $1-2 \times 10^{14}$ W/cm². This value is indeed consistent with the earlier estimate.

From the ionisation fraction calculated above, and using the dispersion equations of chapter 4, the period required for quasi-phase matching can be calculated. This distance is equivalently the distance required between collisions of the driver and pulse train, half the distance between CPB pulses, and twice the dephasing length. The results are shown in figure 9.6 for various realistic pressures. For the $q=23-27$ harmonics visible from the capillary, the QPM period would be at least 1.6 mm, possibly much longer. At most three such QPM periods could thus be obtained using the existing pulse train optics, a far smaller number than hoped for. To be sure, the ionisation and dephasing length vary rapidly with time and space, so these are only crude estimates.

Even if quasi-phase matching were obtained for these low-order harmonics, it would be

(a)



(b)

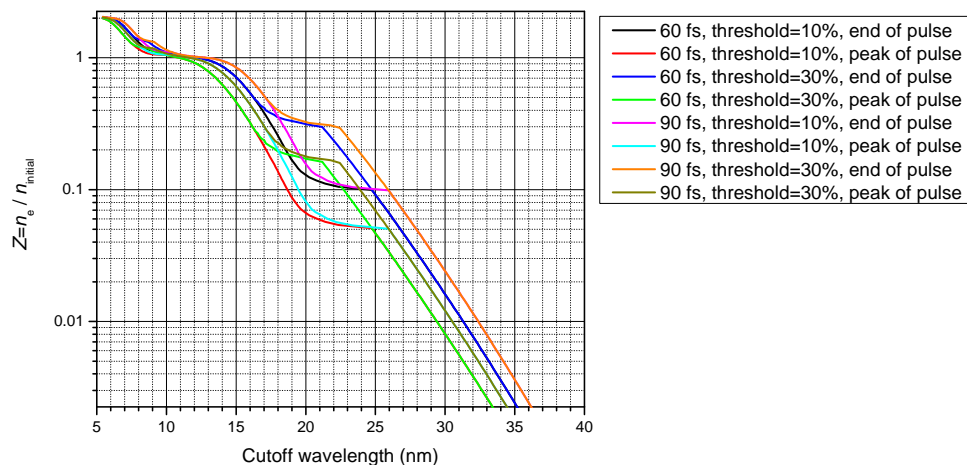


FIGURE 9.5: Results of simulations by the author of ADK ionisation rates for argon. In each graph, the horizontal dimension is the $\lambda_{\text{cutoff}} = hc / (U_i + 3.17U_p)$ cutoff wavelength. Given the experimental cutoff wavelength, these plots can be used to estimate (a) the peak intensity in the gas, and (b) the level of ionisation. In the calculation, the appropriate ionisation energy U_i switches from that of one ionisation state to the next when a threshold Z is crossed. Since it is not clear which value to use for this threshold, calculations for both $Z_{\text{threshold}}=10\%$ and $Z_{\text{threshold}}=30\%$ are given above for comparison. The separation of the curves at 20 nm marks the transition from $\text{Ar} \rightarrow \text{Ar}^+$. In (b), the ionisation fraction is given for both the time of peak intensity and for $t \rightarrow \infty$.

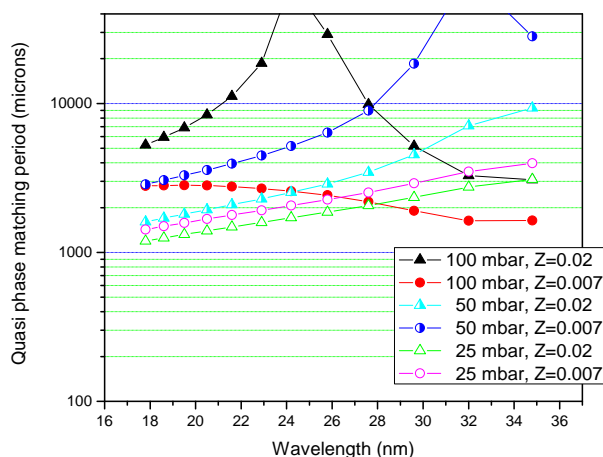


FIGURE 9.6: Quasi phase matching period, equivalent to twice the dephasing length, for the inferred conditions inside the 101 mm long, 102 micron diameter capillary. Since the ionisation fraction Z was uncertain, curves are given for a high (0.02) and low (0.007) value consistent with the observed harmonic cutoff. Points are plotted at the wavelengths of the harmonics.

beside the point. For these low order harmonics, *true* phase matching can already be achieved [62, 65], as indicated by the possibility of large quasi phase matching lengths in figure 9.6. QPM is useful because it can potentially be applied to higher-order harmonics, those made only when the ionisation fraction exceeds 5%, whereas Z was likely less than half this amount in the capillaries. Thus, the Oxford experiment was not quite in the ideal parameter regime.

Thus, use of capillaries for quasi-phase matching presented a host of problems. Manufacture and alignment were difficult. Laser energy transmission was poor. Line emission prevented any view of harmonic generation when a pulse train was used. If quasi-phase matching is to be taken to its full potential, a waveguide may eventually be necessary. But for a first proof-of-principle for quasi-phase matching, a less ambitious tack was perhaps appropriate. By making harmonics in a standard focusing geometry, rather than in a waveguide, all the above difficulties are removed.

9.2 Harmonic Generation in gas cells

It was not possible to obtain a gas jet in the time remaining for this experiment. Other existing hardware, however, could be quickly modified to make a gas cell. A length of 3 mm was used as

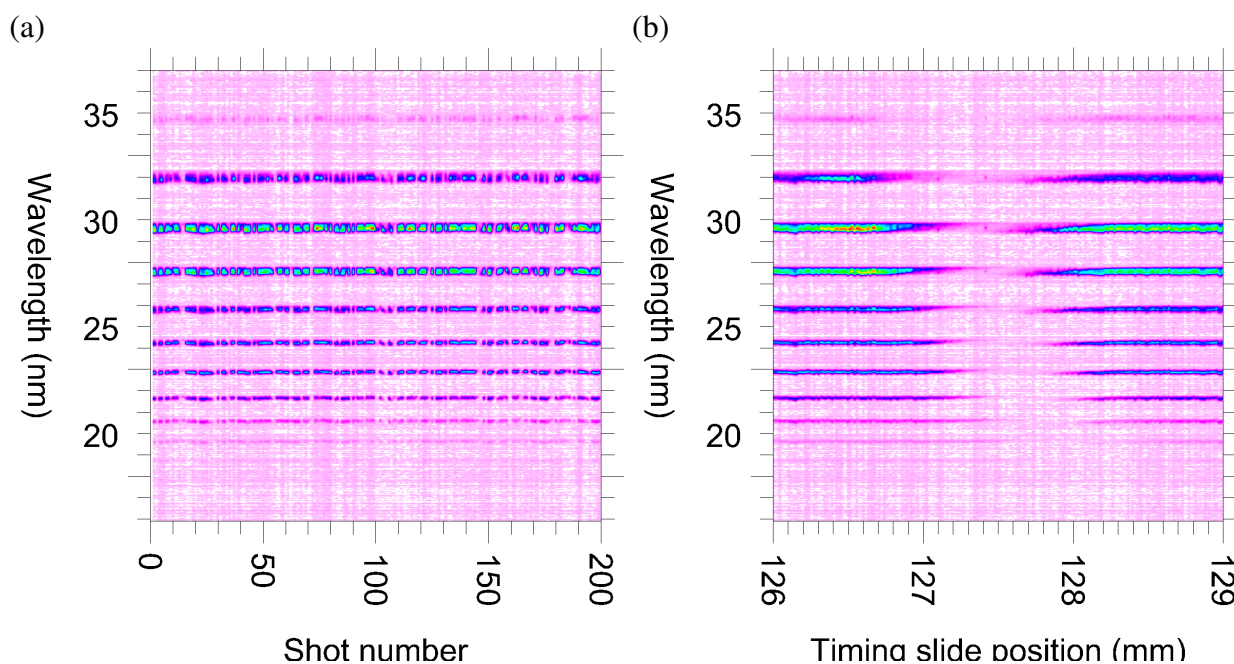


FIGURE 9.7: (a) Variation in high-harmonic spectrum as a function of shot number while the timing slide is moved to random locations. Counts are binned in the spatial dimension on the CCD. (b) The same spectra, now arranged in order of timing slide position, reveal the reproducible extinction of HHG near a location of 127.6 mm.

this was the only reasonable size which could be constructed without lengthy machining work. The gas cell was found to be useful for exploring the effects of the CPB.

Although line emission from the CPB was sometimes seen immediately after new gas cell walls were introduced, it was never visible after several tens of shots, when holes had been bored in the gas cell walls to a sufficient radius. Another advantage of the gas cell was that the XUV signal was much stronger. There were typically 50-500 times as many counts per shot on the spectrograph CCD as for the best shots in a 101 mm capillary.

9.2.1 Parameter scans

With it now possible to measure clear high harmonic spectra with the CPB active, scans were performed in which the driver delay timing slide was varied. To distinguish the effect of the timing slide position from other effects that may have produced variation with time, the scans were performed in a random order. After the data were sorted by slide position, as shown in figure 9.7.b, a region of HHG extinction would typically be apparent. A plot of the shots in chronological order, shown in part (a) of the figure, could confirm that signal variation with

time or laser shot number was not significant. In all scans reported in this thesis, including scans of pressure or laser energy, a similar random-order protocol was followed.

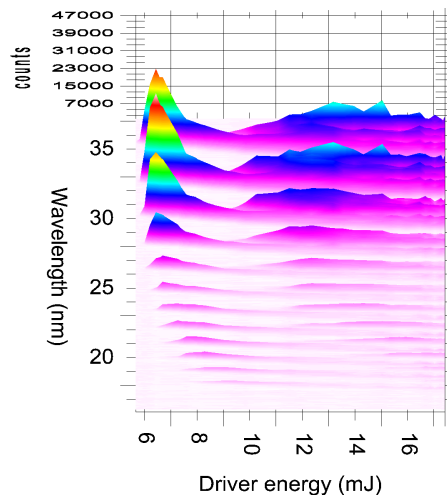
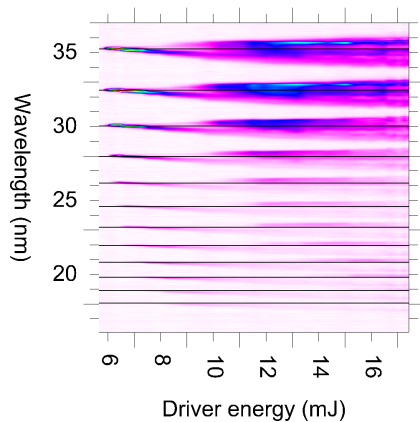
9.2.2 Selecting a QPM parameter regime

In order to observe enhancement of HHG, it was necessary to have several dephasing lengths in the high-harmonic-producing region. Because of the short Rayleigh range (1.5mm), and the additional defocusing effects of ionisation, this length L_g over which harmonics were generated was likely to be on the order of a millimetre or less. The available (*pressure, driver laser energy*) parameter space was explored in an effort to determine the dephasing length and ensure it was less than L_g . A large uncertainty remains for some parameters due to conflicting evidence regarding the driving intensity.

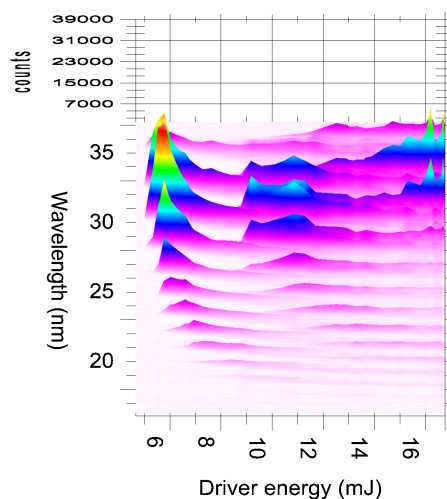
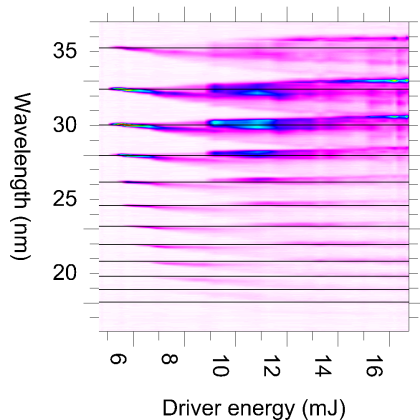
Scans of driver laser energy were conducted at several pressures, as shown in figure 9.8. The shortest cutoff wavelength observed appeared to be just beyond the 17 nm Al L-edge, as seen at 25 mbar pressure and high driver energies. The cutoff wavelength was slightly longer for higher pressures. Again using the ADK ionisation rate calculation, this cutoff energy can be used to infer the intensity and ionisation fraction, using figure 9.5. For a 60 fs pulse, the 16-17 nm cutoff observed for 25 mbar corresponds to an ionisation fraction Z of 0.2-0.4. For 50 mbar the likely range for Z is 0.1-0.4. For 100 mbar the likely range is 0.06-0.3. In all cases the inferred intensity is very close to 2×10^{14} W/cm².

For comparison, the expected peak intensity at focus can also be calculated from the beam energy, focusing geometry, and pulse duration. The beam energy measurements are likely to be accurate, as the energy on target was measured directly with a calorimeter, and the values corresponded to what was expected from measurements before the conversion to the CPB configuration. As discussed in section 7.1, the pulse duration for the laser system has been measured by several diagnostics and at many times, and the result has almost always been 50-70 fs. However, the only measurement taken for the exact grating separation and GVD configuration of these experiments was the cross-correlation signal analysed in section 7.1, which suggested the pulse duration may have been as long as 280 fs. At a typical driver energy (8 mJ), and assuming a diffraction-limited driver, a 60 fs pulse would have a peak intensity of 1×10^{16}

(a) 25 mbar



(b) 50 mbar



(c) 100 mbar

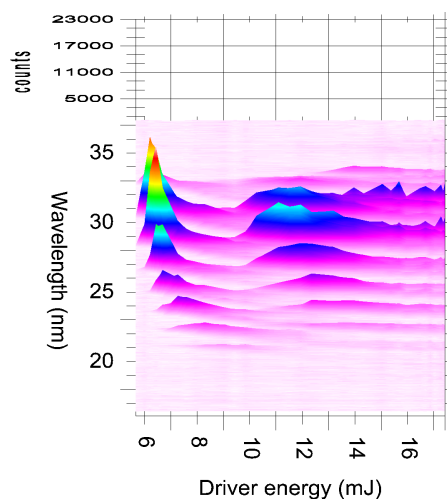
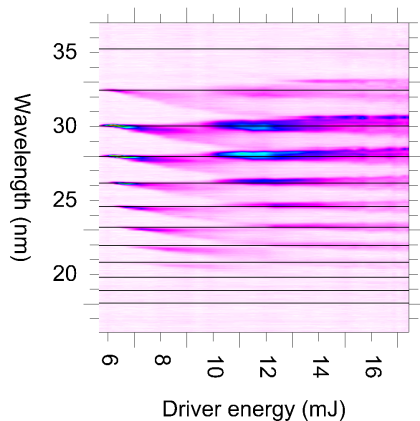


FIGURE 9.8: The $(\text{pressure}, \text{driver energy})$ parameter space available for the Oxford experiment.

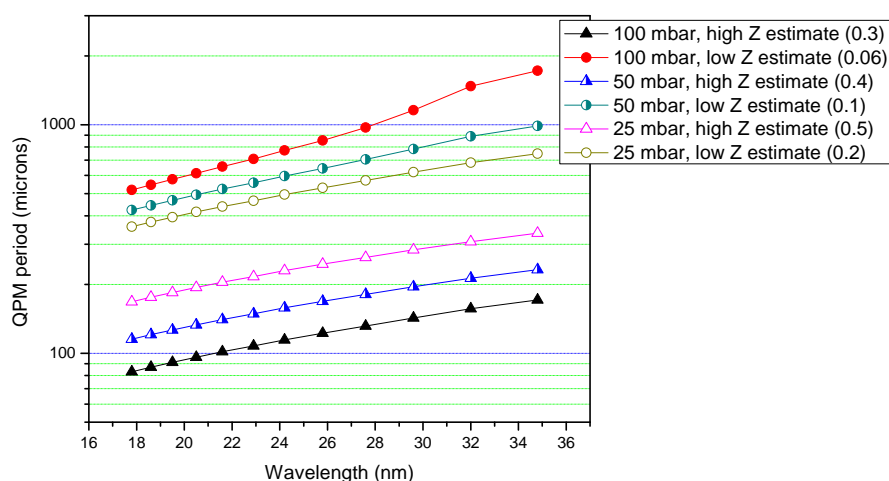


FIGURE 9.9: Estimation of the QPM period for various pressures, based on equation 4.35. Calculation assumes the focal spot radius to be $1.5\times$ diffraction limited.

W/cm^2 , ~ 50 times higher than the intensity predicted from the harmonic cutoff. Even if the longer 280 fs pulse duration measurement is taken to be correct, the $2 \times 10^{14} \text{ W}/\text{cm}^2$ intensity estimated from the cutoff could only arise if the focal spot radius were three times larger than the diffraction limit. A factor closer to ~ 1.5 would be expected for this quantity. Unfortunately, there was not time to measure the focal spot size directly.

The peak intensity may indeed be higher than the harmonic cutoff suggests. It is not uncommon for experimental harmonic spectra to show a cutoff at lower energy than equation 2.2 predicts [8], including spectra from argon for the harmonic orders examined in question [85]. The understood reason for the reduced apparent cutoff energy is that by the peak of the pulse, the high level of dispersion due to free electrons makes $|\Delta k|$ too large for significant accumulation of harmonics.

Thus, there remains uncertainty as to the intensity and pulse duration, and therefore as to the ionisation fraction and dephasing length. The most likely scenario to explain the intensity discrepancy is that several factors all contributed: a longer-than-expected pulse duration, poor spot quality, and a harmonic cutoff energy artificially lowered by phase mismatch. In the analysis that follows, the possibility of either low intensity ($2 \times 10^{14} \text{ W}/\text{cm}^2$) or high intensity ($3 \times 10^{15} \text{ W}/\text{cm}^2$) will be considered.

For the high-intensity scenario, the QPM period will vary between infinity and very small

lengths. For 100% ionisation, the QPM period would be ≤ 0.2 mm for 25 mbar argon, and ≤ 0.06 mm for 80 mbar argon. For these values, there will be times when there are many dephasing lengths within the HH-generating volume, as required. However, for the low-intensity scenario, it was uncertain that the QPM period would ever become short enough. If there were not multiple dephasing lengths within the HH-generating volume, no QPM could ever be observed. Consequently, efforts were made to estimate the minimum QPM period in case the low intensity scenario were the correct one.

In this scenario there is a large uncertainty in which QPM periods are accessible, principally due to the uncertainty in Z . The high estimates of Z yield sufficiently short values for the QPM period (0.1 mm-0.3 mm), while the low estimates of Z yield values which are longer than desired. Thus, care needed to be taken in selecting the pressure and driver laser energy to use. It seemed prudent to minimise the QPM period, which required that the magnitude of the free electron dispersion be maximised. This in turn required maximisation of the gas density and the ionisation fraction. The ionisation fraction is monotonically related to the high harmonic cutoff wavelength (assuming phase mismatches do not limit which harmonic orders are visible), so to maximise ionisation one can maximise the harmonic cutoff frequency. The ionisation fraction is not necessarily optimised by maximising laser energy; raising the driver energy may result in enough additional defocusing that the peak intensity actually decreases. For example, in figure 9.8.c the $q=39$ harmonic (the highest order present) was observed only for driver energies *below* 12 mJ. To maximise Z , then, most of the Oxford experiments were conducted at a moderate driver laser energy of 8 mJ rather than the maximum possible 17 mJ. However, for comparison, some scans were also taken at maximum driver energy (the “high driver regime.”) Because the gas cell holes widened over time, it was not possible to maintain 100 mbar for more than 1 or 2 scans. Consequently, a slightly lower pressure of 80 mbar was taken as the standard for the 8 mJ “low driver regime.”

It can be seen in figure 9.8.c that the $q=23$ harmonic vanishes at high pressures. It is quite likely that this disappearance is due to absorption by the argon rather than to phase matching because, as this figure shows, the presence or absence of the harmonic does not depend on the driver energy. The tabulated absorption of argon (figure 9.10) indeed suggests that absorption

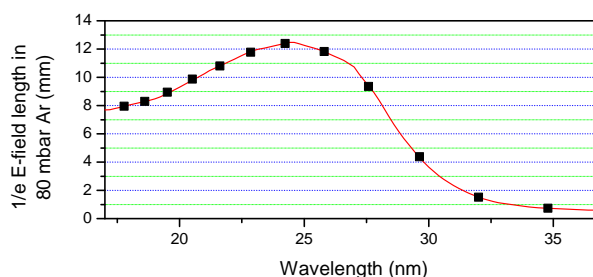


FIGURE 9.10: Absorption lengths for the 80 mbar Ar used in the low-driver regime scans. Points mark the locations of the high harmonics.

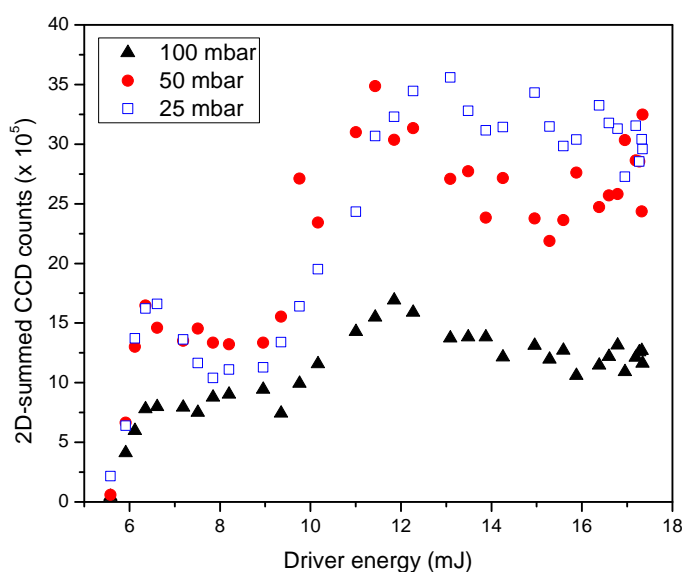


FIGURE 9.11: The same driver energy scans shown in figure 9.8, now integrating over wavelength.

should be significant for this harmonic – and only this harmonic – at the relevant pressure.

9.2.3 Energy dependence

Figure 9.8 shows that the spectral power for a given harmonic varies in a non-monotonic way as driver energy is increased. Each harmonic is only visible above a certain critical driver energy, and the harmonic's spectral power is maximised at an energy just above this critical value. For additional driver energy, the harmonic spectral power decreases markedly, only to increase again when the driver energy exceeds about 10 mJ. The three driver energy scans are plotted again in figure 9.11, this time summing the spectra over wavelength to look at the total number of

XUV counts between $17 \text{ nm} < \lambda < 36 \text{ nm}$. The *total* XUV signal is closer to being monotonic with driver energy (though it still is not completely so), indicating that much of the decrease in *spectral* XUV signal with driver energy is due to spectral broadening.

Figure 9.11 also highlights the jump in harmonic signal as the driver energy passes 10 mJ. This energy seems to be a pressure-independent threshold for some mechanism that dramatically boosts the XUV signal. One possible explanation is that intensity-dependent phase and Gouy phase are dominant in phase matching, and that two regions of space become phase matched for driver energies beyond 10 mJ, whereas only one region is phase-matched at lower energies. This scenario accords well with numerical results of Salières *et al.*, which show phase matching in two distinct spatial regions when the driving intensity is sufficiently high [26, 27, 29]. The intensity regime for the effects seen by Salières is $\sim 2 \times 10^{14} \text{ W/cm}^2$, consistent with the observed harmonic cutoff. One problem with this explanation, however, is that neutral and free electron dispersion were expected to dominate Gouy phase in the Oxford experiment, since high pressures and high f-number focusing was used. In this case, phase matching should have still showed pressure dependence, in contrast to the observed pressure-independence of the 10 mJ threshold.

9.2.4 Experimental comparison of extinction by parallel and perpendicular polarised light

A series of scans of CPB energy were run to compare the parallel and perpendicular polarisation methods. These scans were performed with 80 mbar argon in the gas cell, and using 8.2 mJ in the driver beam. In these experiments, a scan of the timing slide was first performed, as in figure 9.7.b, to determine the slide position for the subsequent CPB-energy scan. It can be seen in this figure that different harmonics were extinguished at different timing slide positions. This was likely due to the fact that the harmonics were generated in different locations in the gas volume, owing to, for example, the spatially varying intensity of the driver beam; this will be further discussed later in this chapter. For the extinction experiments discussed in this section, the timing slide was always set to a location for which all harmonics were largely extinguished.

As a consequence of this compromise, the timing slide position was not optimal for extinction of the lowest or highest orders. In future experiments, it might be better to use a different timing slide location for each harmonic, a location that optimally extinguishes that harmonic regardless of whether other harmonics are suboptimally damped.

The pulse trains used were bursts of 16 pulses at the minimum possible spacing, as in figure 7.6. As the duration of each pulse was large compared to the pulse spacing, the superposition resulted in a roughly square-wave pulse. This long CPB pulse was used so that a single timing slide location could largely extinguish all harmonic orders rather than just a few.

With the timing slide location fixed based on the results of this initial scan, harmonic spectra were then recorded as the pulse train waveplate (and consequently the pulse train energy) was varied. The effect of pulse train energy on several typical harmonics is plotted in figure 9.12. For the parallel polarisation scheme, the data are fit well by a decaying-exponential-plus-constant. The fact that the decay does not go fully to zero may be explained if the region in which harmonics are generated is larger than the region in which the driver and pulse train interact. In particular, some small transverse misalignment between driver and CPB is almost inevitable, in which case no CPB energy will be sufficient to fully extinguish the harmonics.

The variation of each harmonic with pulse train energy was fitted to a separate decaying exponential. The energies corresponding to half-extinction for these fits are plotted in figure 9.13. For the perpendicular polarisation scheme, the data accord well with the prediction from equation 5.14. For parallel polarisations, the required intensity for extinction agrees well with the prediction for the direct phase modulation effect (equation 5.5.) However, these intensities are much higher than the predicted values for extinction from intensity-dependent phase modulation (equation 5.7.) For the low-intensity scenario, the intensity-dependent phase model under-predicts the required counter-propagating intensity by at least 10. For the high-intensity scenario, the error is at least a factor of 1000. This discrepancy could indicate several things. First, the phase of harmonic emission may be less sensitive to intensity than predicted by theory (equation 2.4). If so, the problem caused by intensity-dependent phase for phase matching or QPM of harmonic generation in capillaries (discussed in section 8.6.1) may be reduced. Secondly, unless the actual $|d\phi/dI|$ is less than 1/1000 of the theoretical value of equation 2.4, the

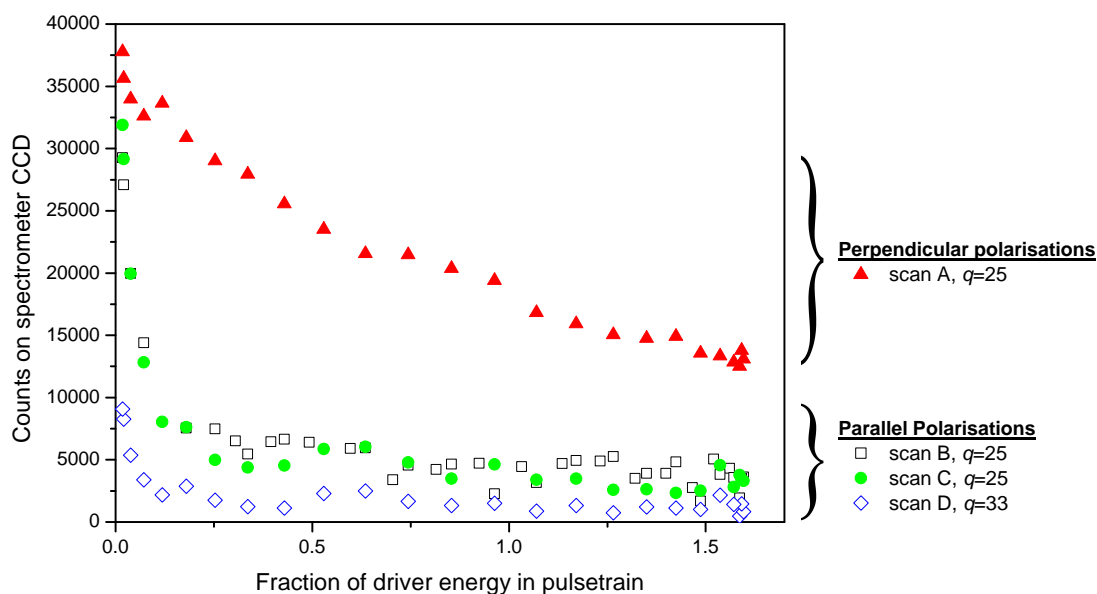


FIGURE 9.12: Dependence of harmonic signal on pulse train energy. To obtain these y-values, counts are binned in both dimensions on the CCD.

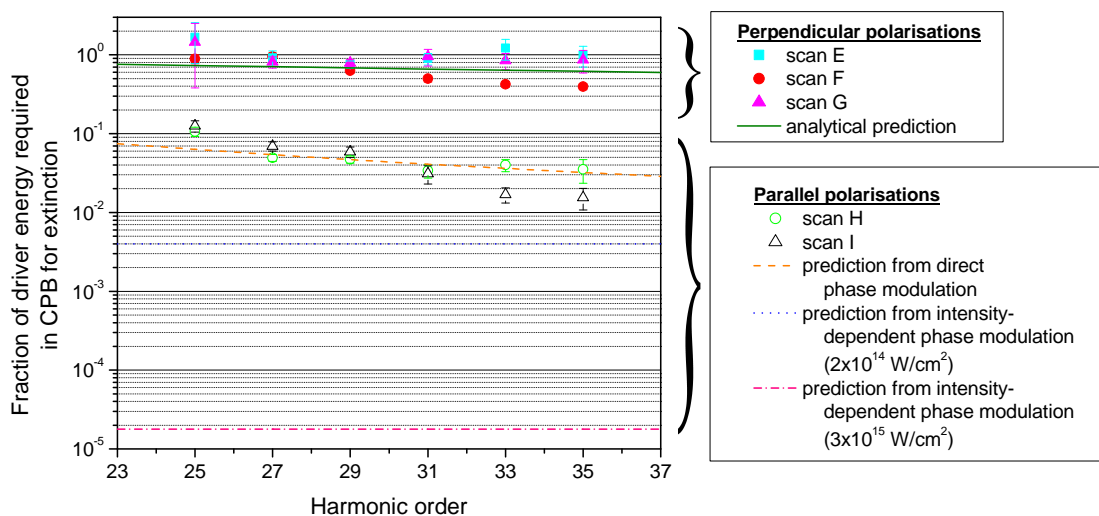


FIGURE 9.13: Energy required for half-extinction, normalised by driver energy. Measured values are compared with the predictions of chapter 5.

parallel polarisation data support the low-intensity scenario.

For all data presented in the remainder of this chapter, the parallel polarisation configuration was used.

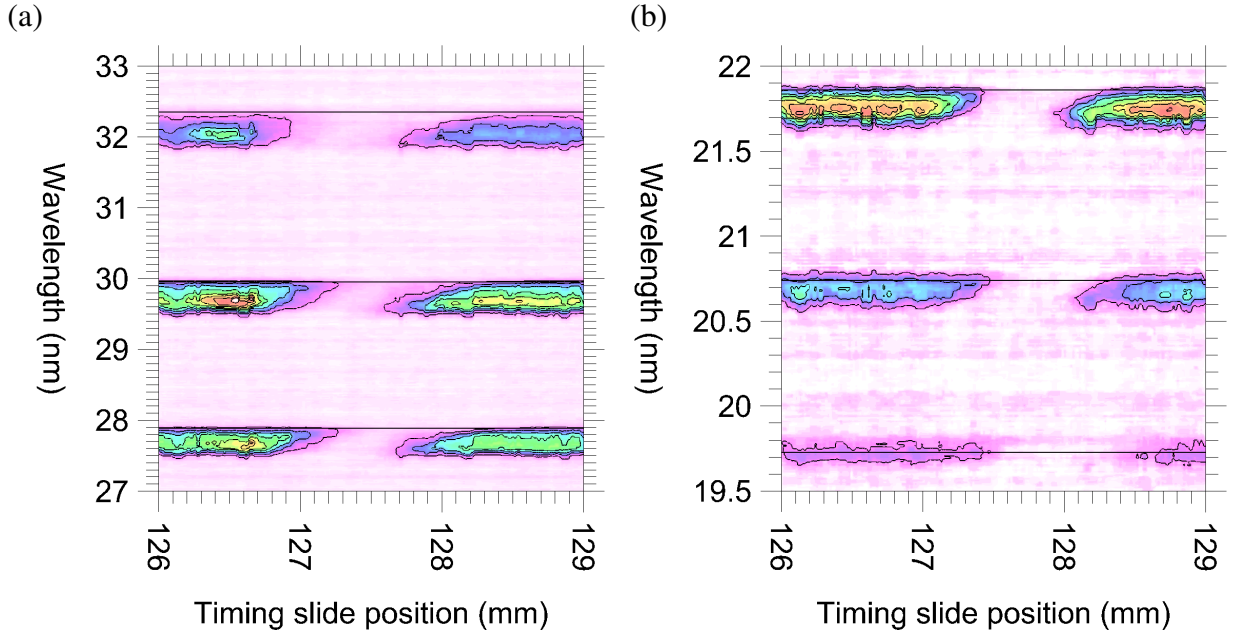


FIGURE 9.14: Closer view of the extinction region for the timing scan shown in figure 9.7. (a) $q=25, 27$, and 29 . (b) $q=37, 39$, and 41 .

9.2.5 Analysis of extinction and enhancement regions

Figure 9.14 shows the extinction regions for various harmonic orders in the low driver energy (8 mJ) regime. A CPB consisting of 16 closely-spaced pulses was used. Figure 9.15 shows how the extinction pattern varies with the burst length of the CPB. An exciting observation, visible in both of these datasets, is a small but very reproducible enhancement of the harmonic orders $23 \leq q \leq 29$. The enhancement occurred for timing slide positions slightly lower than those which result in extinction.

To better understand this enhancement feature, and to understand the patterns in the timing scans more generally, the scans can be analysed in an attempt to extract such parameters as the quasi phase matching period $L_{\text{qpm}} = 2\pi/\Delta k$ and the length over which the harmonics are generated L_g . In modeling the extinction regions mathematically, there are many varying parameters to consider. For example, intensity and Δk change with all four space-time coordinates. Because of the inevitable trade-off between completeness and complexity, here several models of increasing sophistication are presented. All exclude some potentially important physics.

It is instructive to first consider a reduced form of equations 4.13 and 4.14 for the accumu-

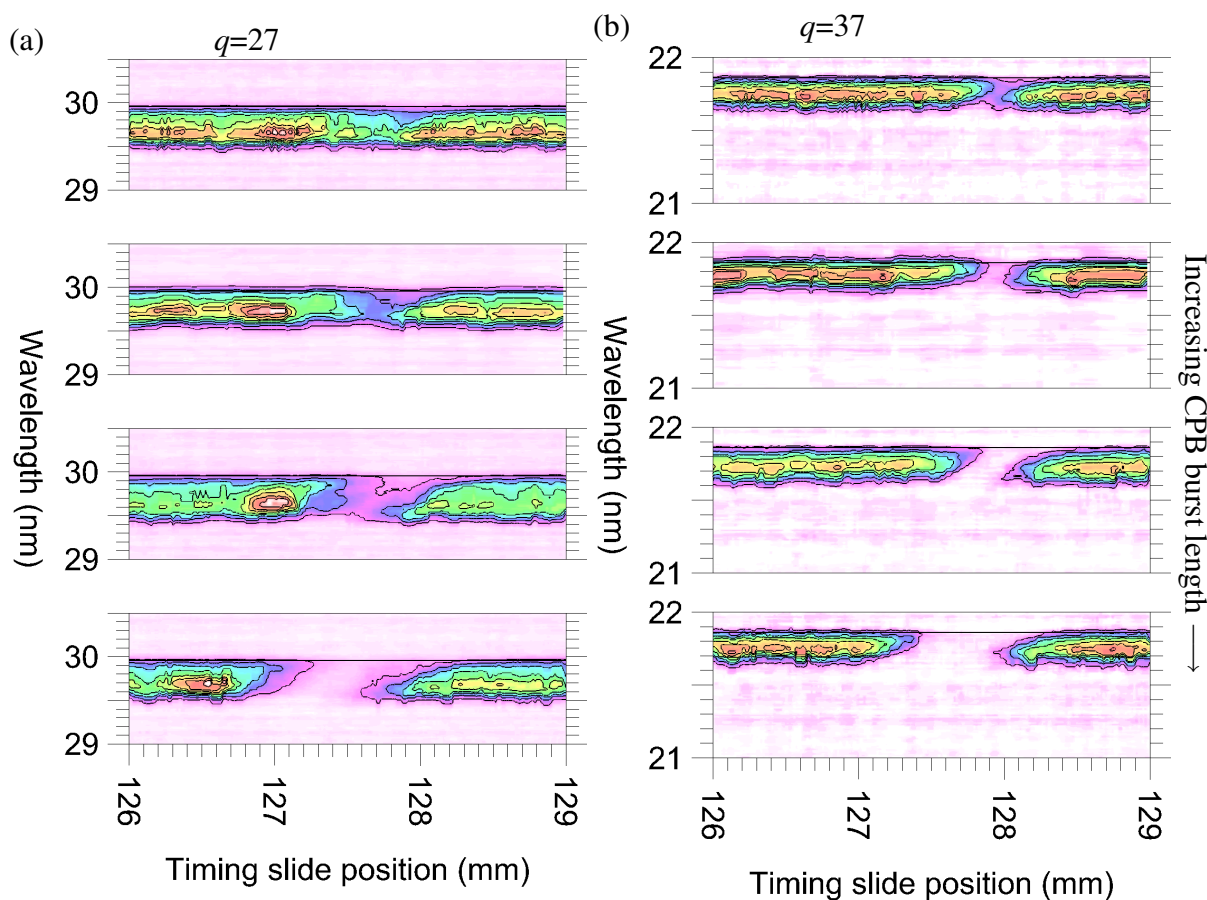


FIGURE 9.15: Variation in the extinction pattern as the length of the CPB burst is increased. From top to bottom, CPB burst length increases from 1 to 4, 8, and 16 pulses. Energy per pulse in the CPB is held fixed, so total energy increases proportional to the number of pulses. Colour scales for (a) and (b) are different.

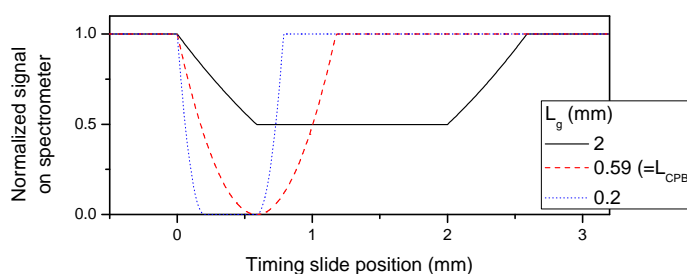


FIGURE 9.16: In the model of equation 9.2, the depth and width of an extinction region depend on the generation length L_g and the length of the CPB pulse L_{CPB} .

lation of the high harmonic signal:

$$I(s) = \left| \int_0^{L_g} h \chi(z-s) dz \right|^2 \quad (9.2)$$

Here, $I(s)$ is the spectrograph signal recorded for timing slide position s , h is an overall scale constant, and $(1 - \chi(z-s)) \in [0, 1]$ is the fractional extinction caused by the CPB. This model assumes $\Delta k = 0$, ignores blueshifting, presumes harmonics are generated uniformly over the interval $[0, L_g]$, and excludes all other spatial and temporal variation in the single-atom amplitude and phase. A square pulse in the CPB is assumed, and extinction is taken to be complete wherever the CPB and driver overlap:

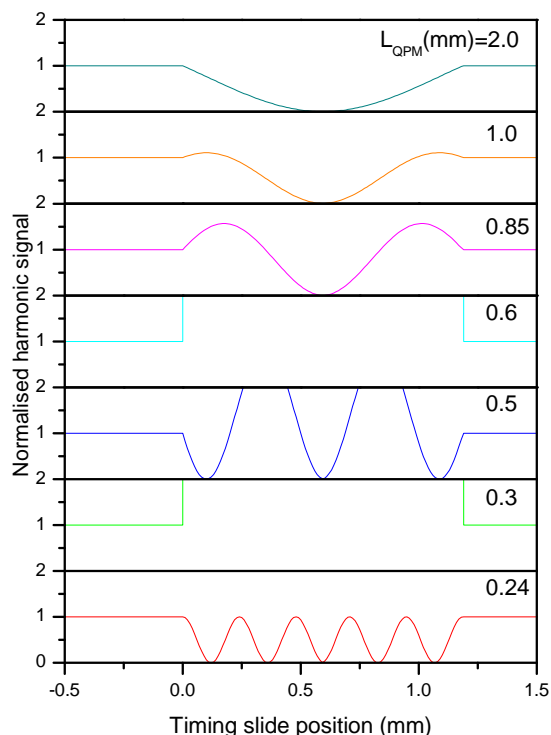
$$\chi(z-s) = \begin{cases} 0 & \text{if } -L_{\text{CPB}} < z-s < 0 \\ 1 & \text{otherwise} \end{cases} \quad (9.3)$$

Here and throughout this chapter, L_{CPB} will be taken to mean the length of interaction between driver and CPB, which is half the actual length in space of the CPB. Figure 9.16 shows simulated timing scans based on the above model for various values of the generating length L_g . The burst length of the CPB L_{CPB} is set to the value used in figure 9.14. As the figure shows, complete extinction occurs if and only if $L_{\text{CPB}} > L_g$. The timing slide distance between full signal and minimum signal is the lesser of L_g and L_{CPB} . From the minimum CPB duration required for complete extinction, figure 9.15 suggests that L_g is roughly 0.1-0.2 mm for $q=37$ and is perhaps 0.6 mm for $q=27$. It is reasonable that the generation length differs for different q , since the cutoff harmonics are made only at the highest intensities, while lower orders can be made at a range of intensities, and therefore at a range of locations. Also, from figure 9.14, it does indeed seem that the timing slide distance between full signal and complete extinction is roughly the predicted 0.6 mm (i.e., the length of the CPB).

To see any enhancement from a model, it must include a non-zero Δk . Thus, consider now the following more sophisticated model:

$$I(s) = \left| \int_0^{L_g} h \chi(z-s) e^{2\pi iz/L_{\text{QPM}}} e^{(z-L_g)/L_a} dz \right|^2 \quad (9.4)$$

(a) Absorption ignored



(b) Absorption included

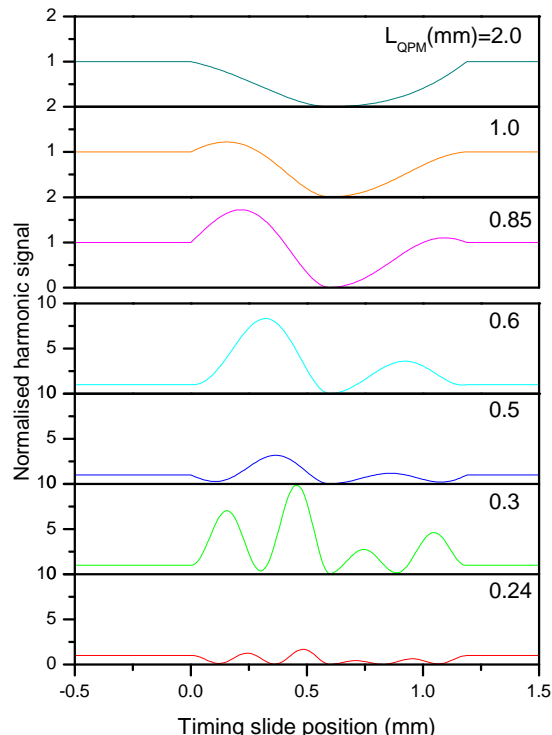


FIGURE 9.17: (a) Timing scans simulated using equation 9.4 with $L_a \rightarrow \infty$ and various values of L_{QPM} . (b) Results for the same conditions but now with $L_a = 0.7$ mm, a realistic value for the $q=23$ harmonic. Note that the lower four plots in (b) use a different vertical scale.

where $L_{\text{QPM}} = 2\pi/\Delta k$ is the period required for ideal QPM. A term for the absorption by the gas has also been introduced, causing the electric field contribution from a particular location to decay by a factor $1/e$ in a distance L_a . Figure 9.17.a shows simulated timing scans based on this equation for $L_a \rightarrow \infty$ (i.e., no absorption), $L_{\text{CPB}} = 0.59$ mm (the value used in figure 9.14), and $L_g = 0.6$ mm. The signal oscillates with a period of L_{QPM} . The magnitude of the oscillations goes to infinity when L_g is an integer multiple of L_{QPM} because of the normalisation: the traces are normalised to the value for when no CPB is present, which in this case is zero. It is this divergence in the enhancement factor that allows Peatross *et al* to see a factor of ~ 100 enhancement in their QPM experiment (figure 5.3.b).

Another noteworthy trait of equation 9.4 with $L_a \rightarrow \infty$ is that only symmetric timing scans can be produced. All enhancement observed in the Oxford experiment, however, appeared only to one side of the extinction. This asymmetry can be recovered in the model by introducing a

finite L_a . Figure 9.10 shows the values of L_a for the 80 mbar pressure used in the low-driver experiments. As this plot shows, absorption is insignificant for all but the lowest harmonic orders visible on the spectrograph. Figure 9.17.b shows results of equation 9.4 for $L_a = 0.7$ mm, the realistic absorption length of $q=23$. Now, for L_{QPM} of 1.0 mm or 0.85 mm, an asymmetric enhancement can be seen that resembles the one seen in the experiment. In both model and experiment, the enhancement appears for timing slide positions below that of the extinction. This can be understood by considering that harmonics produced far from the spectrograph “count less” for the final output because of absorption. Consequently, the change in final signal is greater when the spectrograph-side region is suppressed (small s) than when the opposite side is extinguished.

The model with absorption and $L_{\text{QPM}} \approx 0.85$ mm can also reproduce the asymmetric timing scans for $q=25$ and 27, but only if an unrealistically short L_a is used. Alternative causes of the asymmetry should therefore be considered. It is possible that the asymmetry observed in the experiment is a consequence of intensity-dependent phase, which can cause strong asymmetry between harmonics produced just before and just after a focus [26, 29].

Intensity-dependent phase is but one of many factors which could be considered in future analyses. Better values for L_{QPM} and L_g could probably be extracted from the data by considering spatial variations of Δk , together with the 1-D WKB model (equation 4.21) or a full wave equation solver.

Another noteworthy feature in the timing scans is that different harmonic orders are extinguished at different timing slide locations. Consequently, the different orders must be generated from different longitudinal locations in the gas. The effect can be seen in figures 9.14 and 9.7. Compared to lower harmonic orders, higher orders are extinguished at higher timing slide positions, so they must be produced further from the spectrograph. Ignoring phase matching, one might think that if $q_+ > q_-$, then the longitudinal interval over which order q_+ is made must be a subset of the interval over which order q_- is made. However, the figures show that this is not the case; in figure 9.14 for example, $q=37$ is produced at the location $s=128.3$ while $q=27$ is not. One possible explanation comes from Salières, l’Huillier, and Lewenstein [26, 29]: intensity-dependent phase acts to improve phase matching just past the focus, while it worsens

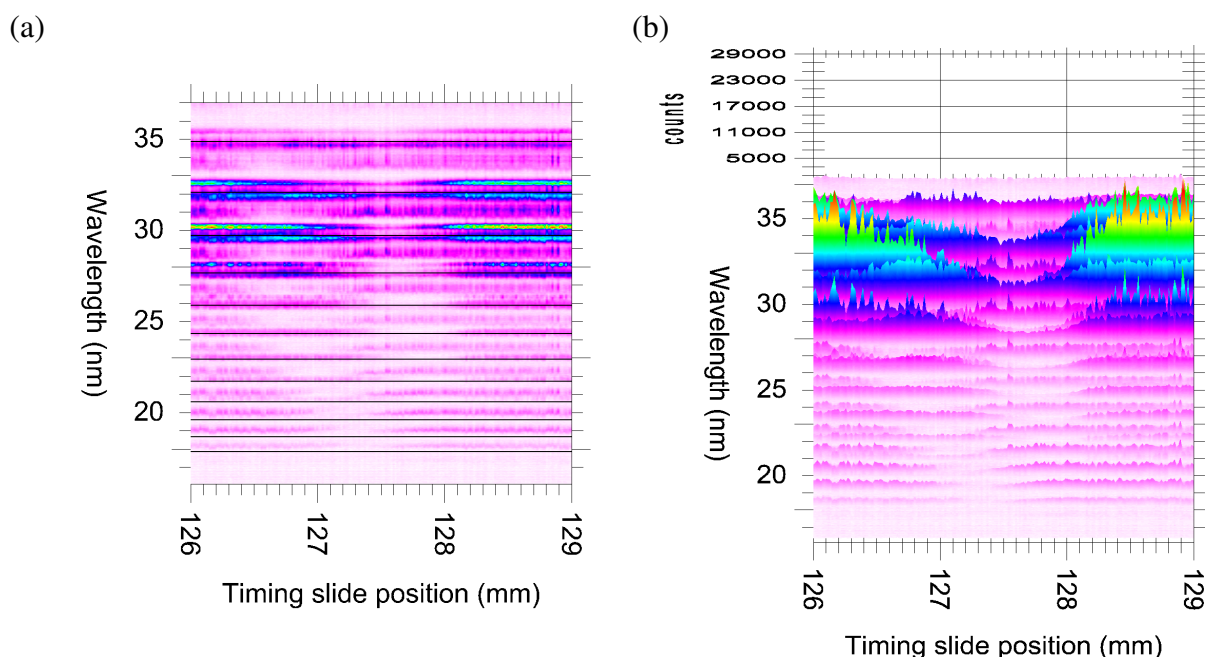


FIGURE 9.18: Timing scan for the high-driver regime. The CPB is a burst of eight pulses at the minimum possible spacing, and maximum available energy (19 mJ). The driver was also set to its maximum available energy (17 mJ), and the argon pressure was 50 mbar.

the phase mismatch just before the focus. Consequently, harmonics tend to originate from the region past the laser focus. However, the highest harmonic orders can only be produced very near to the focus where the intensity is highest.

Figure 9.18 shows a typical timing scan from the high-driver regime. Compared with the low-driver scans discussed above, L_g values seem slightly longer here – closer to 1 mm for many of the harmonic orders. The variation in extinction location between harmonic orders is very pronounced. In addition, each harmonic order is split into several components, and these various components of a given harmonic are extinguished in disparate locations. For the lower orders visible on the spectrograph, the red-most components are extinguished roughly 1 mm away from the blue-most components. This observation will be discussed further in section 9.2.10.

The patterns observed in timing scans may help to decide whether the low- or high-intensity scenario of section 9.2.2 is correct. If the high-intensity scenario were correct, the QPM period would at times be as short as 0.2 mm. Consequently, one would then expect to see multiple-period signal oscillations in the timing scans, as in the lower four plots of figure 9.17 where $L_{\text{qpm}} \leq 0.3$. The lack of such oscillations suggests that the levels of ionisation are more in line

with the low-intensity scenario.

9.2.6 Determination of intensity and ionisation from blueshift

In timing scans such as figures 9.14 and 9.15, one can see evidence of the blueshifting of the fundamental as it traverses the gas. In these figures, the extinction region takes the form of a parallelogram. At low timing slide positions (extinction near the spectrograph), the blue component of the harmonic line is extinguished. Conversely, at high timing slide positions (extinction on the far side of the focus from the spectrograph), it is the red component which is extinguished.

Using equation 2.12, this observed blueshift can be used to find the ionisation and intensity in the medium. The equation is first rearranged to isolate the factors which depend on ionisation:

$$Z \frac{dZ}{dt} = \frac{8\pi^2 c^3 \epsilon_0 m_e}{n e^2 \lambda^3} \frac{d\lambda}{dL} \quad (9.5)$$

where n is now the background gas density and $Z = n_e/n$ is the degree of ionisation. $d\lambda/dL$ is the slope of the sides of the extinction parallelogram in a timing scan. A typical value of $d\lambda/dL$ for an 8 mJ driver in 80 mbar is 8.8×10^{-7} (dimensionless) for $q=31$. From the above formula, this value indicates a $Z \frac{dZ}{dt}$ product of $5.8 \times 10^{11} \text{ s}^{-1}$. The next step in the analysis depends on whether the low-intensity or high-intensity scenario is correct. First, consider the low-intensity scenario, in which harmonics are made at the peak of the pulse. In figure 9.19 the ADK ionisation rates are used to calculate $Z \frac{dZ}{dt}$ for pulses of different peak intensities. The condition $Z \frac{dZ}{dt} = 5.8 \times 10^{11} \text{ s}^{-1}$ is obtained at the pulse peak for a peak intensity of $1.8 \times 10^{14} \text{ W/cm}^2$. A slightly higher intensity ($2.0 \times 10^{14} \text{ W/cm}^2$) results if the cycle-averaged dZ/dt is used in the calculation rather than the maximum instantaneous dZ/dt . At these intensities, the ionisation fraction Z is 0.04 or 0.09 respectively. Note that these values of Z tend to be on the very low end of the range predicted in section 9.2.2 from the observed harmonic cutoff.

For the high-intensity scenario, the peak intensity cannot be deduced from $Z \frac{dZ}{dt}$. In this picture the harmonics are generated at some point in the leading edge of the pulse, but the peak pulse intensity is unclear, as is the time of harmonic emission within this pulse. One possible

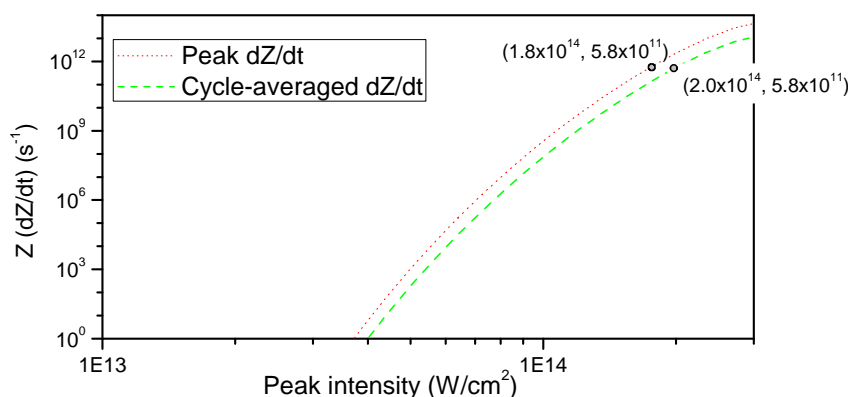


FIGURE 9.19: Values of $Z \frac{dZ}{dt}$ at the time of maximum intensity for 60 fs FWHMI pulses of different peak intensities. For reference, at the rightmost intensity shown (3×10^{14} W/cm², halfway through the pulse the medium is roughly 10% ionised.

avenue for analysis would be to calculate $Z \frac{dZ}{dt}$ for not only different intensities (as in figure 9.19) but also for different times during the pulse. A locus in a 2-D space (*peak intensity, time during pulse when harmonics are emitted*) could then be identified which corresponds to the measured $Z \frac{dZ}{dt}$.

9.2.7 Studies of enhancement phenomenon

Several checks confirmed that the harmonic enhancement effect was real. The enhancement could be turned off and on from one shot to the next by manually blocking and unblocking the CPB. Furthermore, timing scans with the CPB blocked showed a constant spectrum as the timing slide was moved.

Pressure scans were conducted with the timing slide fixed at the position that produced enhancement. As a control, the scan was repeated with the CPB blocked. Results are shown in figure 9.20. At all pressures below 70 mbar, the CPB had some deleterious effect. The effect at 80 mbar was a small enhancement of $q=27, 29$, and perhaps 31. Oddly, the enhancement was less than that observed in timing scans taken immediately before and after the pressure scan. In fact, no enhancement was observed in the pressure scan for $q=25$, while an unmistakable enhancement of ~ 2 was seen in both timing scans. The timing scan after the pressure scan looked identical to the timing scan before the pressure scan, confirming that no experimental

parameters had drifted. Perhaps this confusing behaviour was due to the inevitable difference between the actual pressure inside the gas cell and the pressure just outside it, at the location of the pressure diagnostic. This pressure difference may be different when the gas flow is fixed for several minutes – as in a timing scan – compared to when the gas flow is changed every 30 seconds – as in a pressure scan.

It is unfortunate that a pressure beyond 80 mbar could not be supplied using the available mass-flow controller. The effect of the CPB seems to switch from suppression to enhancement as the pressure rises above 70-80 mbar, and it would be interesting to see how the trend continues as the pressure rises further.

Pressure scans were also carried out in the high-driver regime. Again, no enhancement of harmonic generation was seen.

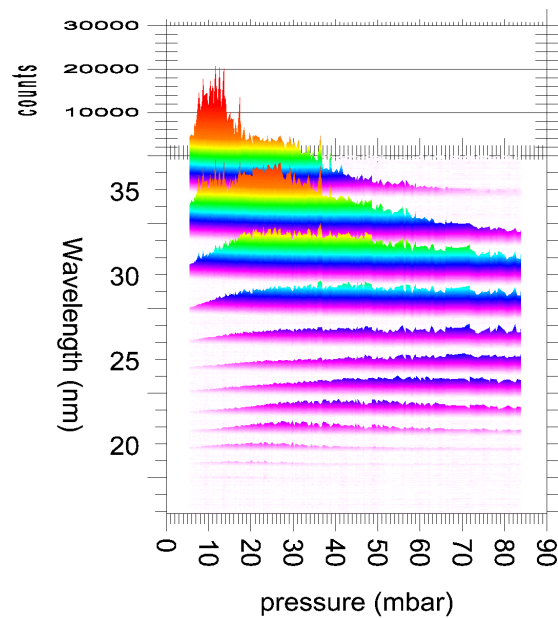
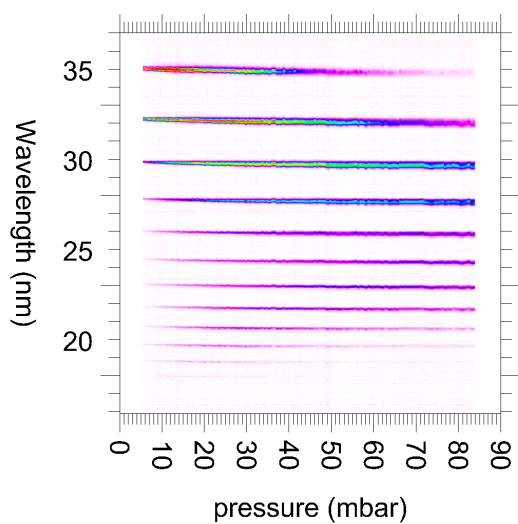
9.2.8 Dependence on focus position

Experiments were carried out with the driver focus both at the gas cell entrance and at the gas cell centre (a difference of 1.5 mm.) This distance was equal to the theoretical Rayleigh range assuming $M^2=1$. In all cases the CPB focus was at the same location as the driver focus.

Figure 9.21 shows scans of driver energy for the two focus positions. No CPB was used. The most noteworthy difference between the plots is greater breadth of the harmonic lines when the laser focus was in the gas cell centre. This evidence supports the earlier conclusion that harmonics are generated over a <1 mm length, for the following reason. The difference in line width suggests that the intensity varies significantly over the 3 mm length of the cell, for if the beam had no z -dependence over the cell, the shift in focus position would have no effect. If harmonics are generated over less than the 3 mm gas length, then the generation length will be shorter when the focus is at the gas cell entrance. Since the driver grows bluer as it traverses the gas, harmonics will be made over a smaller range of blueshifts, and the resulting harmonic line will be narrower.

Figure 9.22, a comparison of *timing* scans for the two focus positions, provides further evidence that the generation length shortens when the focus is moved to the front of the gas cell. Though identical pulse trains were used for the scans in the figure, the width of the extinction

(a) CPB blocked



(b) CPB = single burst

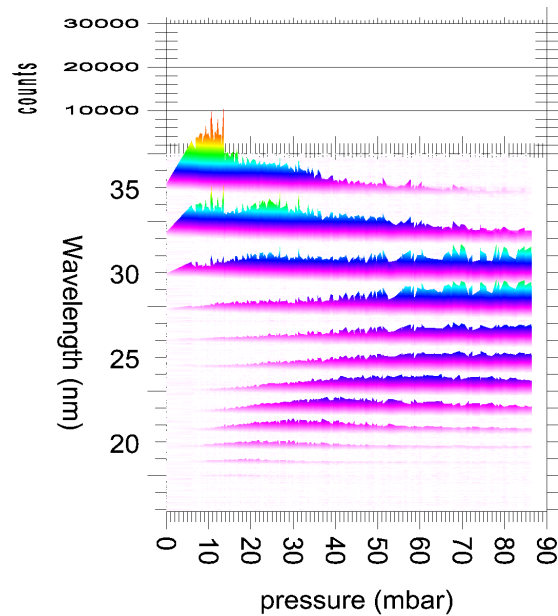
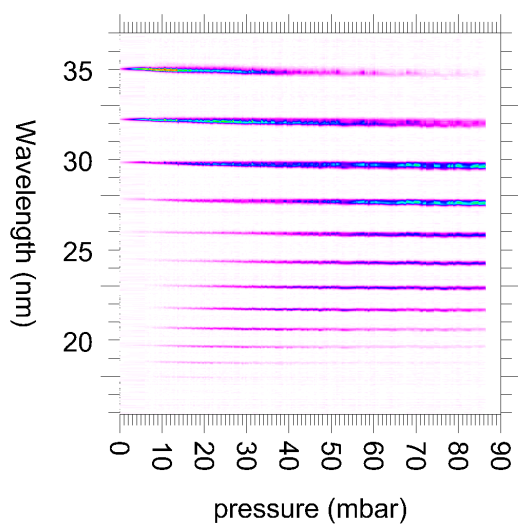
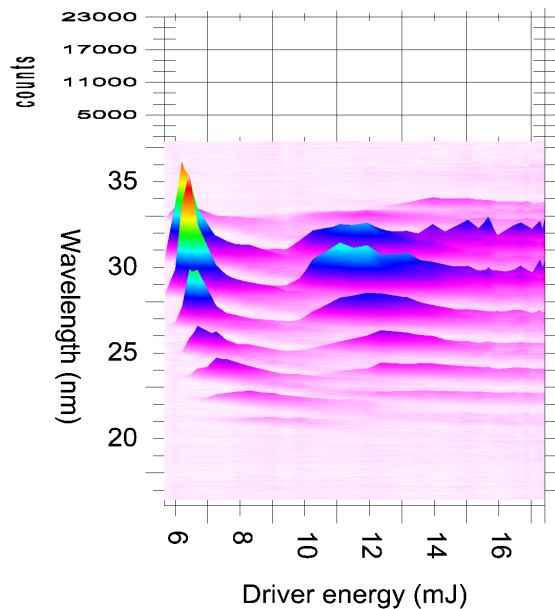
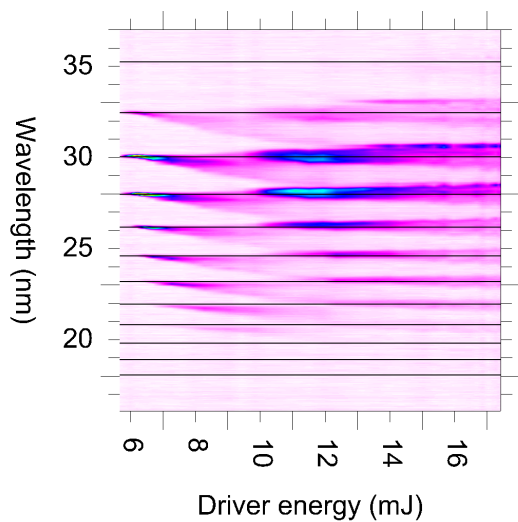


FIGURE 9.20: Pressure dependence of the modest enhancement effect in the weak driver regime. The colour scales of (a) and (b) are identical.

(a) Focus in centre



(b) Focus at entrance

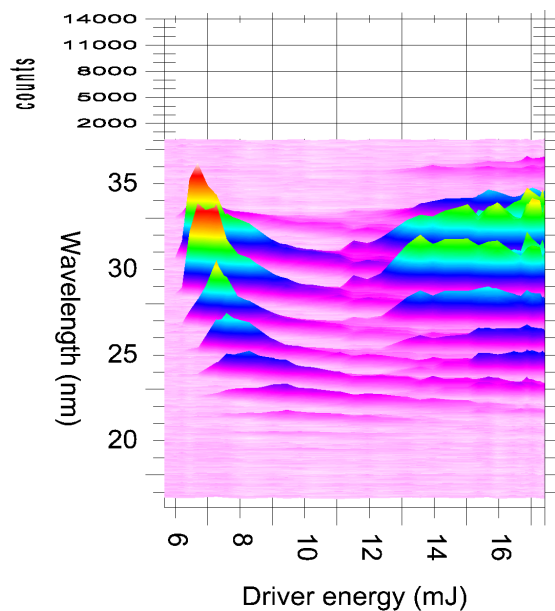
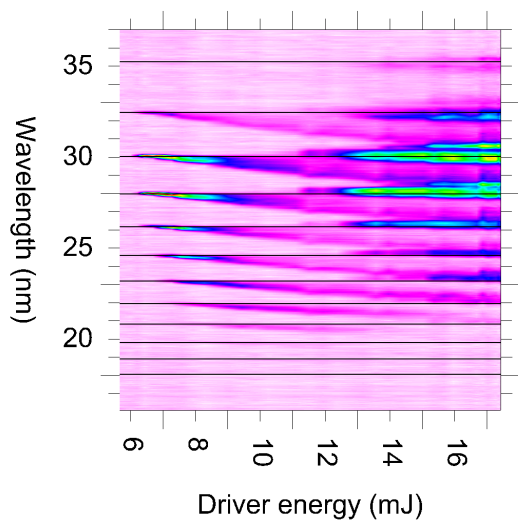
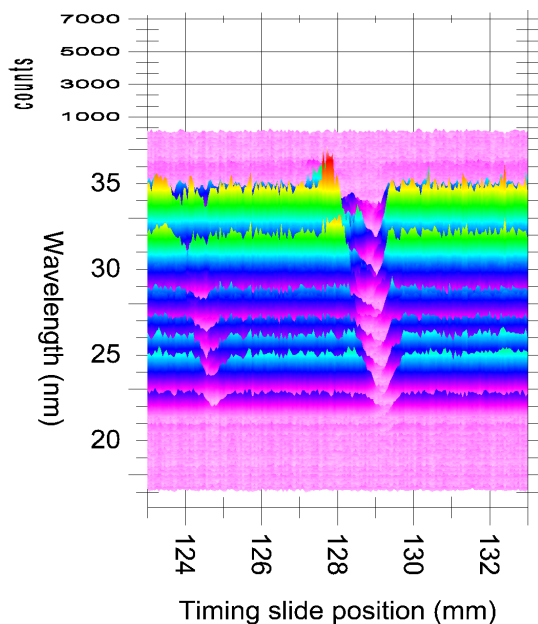
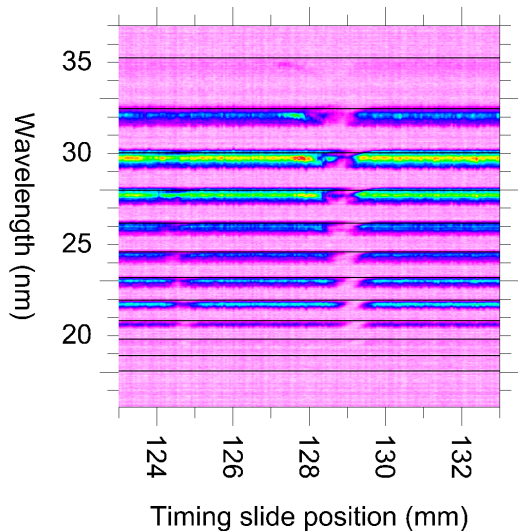


FIGURE 9.21: Dependence of the harmonic spectrum on focus position relative to gas cell, looking at scans of driver energy in 100 mbar Ar. The CPB was blocked for these scans.

(a) Focus in centre



(b) Focus at entrance

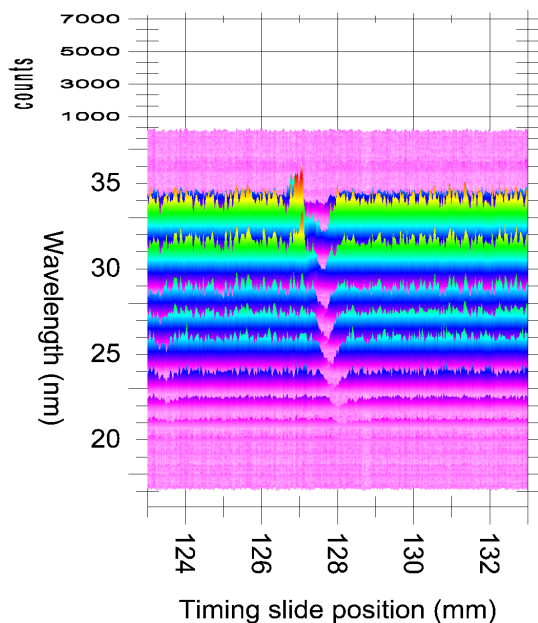
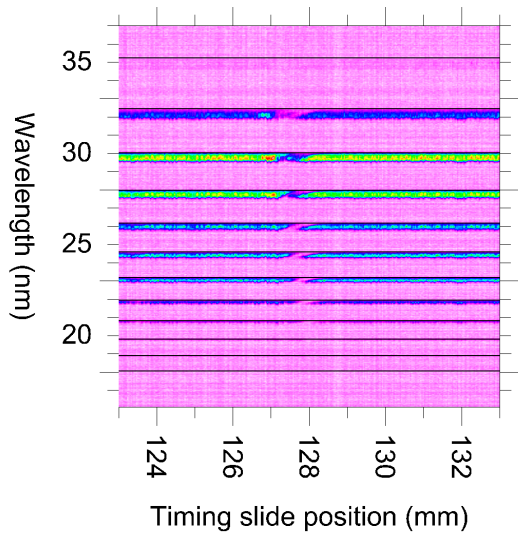


FIGURE 9.22: Dependence of the harmonic spectrum on focus position relative to gas cell, looking at scans of timing slide. The minor second extinction region near 124 mm in both figures is related to the satellite pulse observed in cross-correlation (section 7.2).

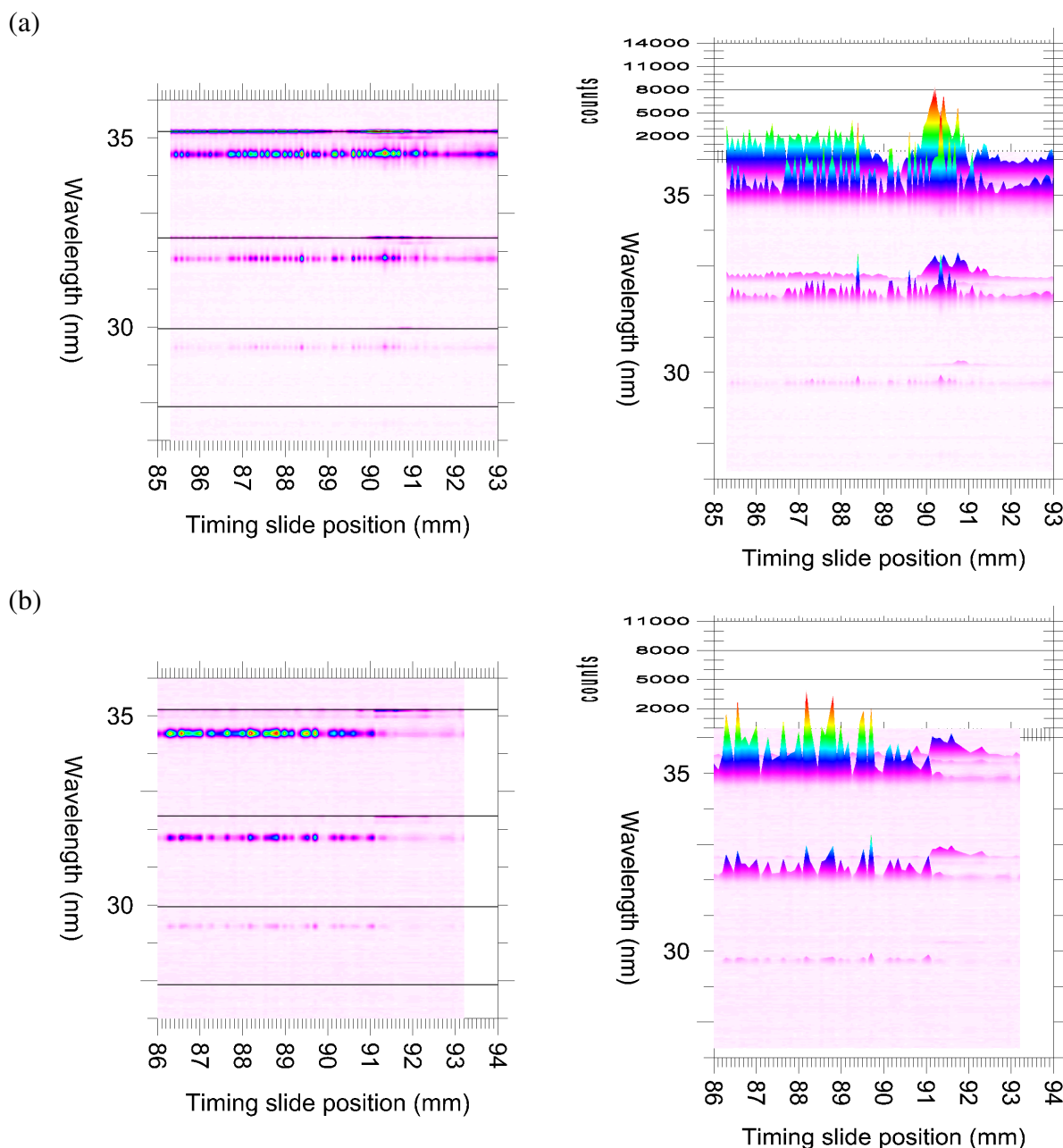


FIGURE 9.23: Two early timing scans when the driver was not optimally compressed. These were the two strongest signals seen before the driver was compressed to 60 fs – almost all other timing scans in this configuration showed no effect.

region is shorter in the scan with the focus at the gas cell entrance.

9.2.9 Dependence on pulse compression

The pulse lengths were varied at several point in the experiment by adding or removing glass from the beams and by adjusting the compressor grating separation. These adjustments were found to have dramatic effects on the extinction of harmonics.

In the initial configuration, the compressor grating spacing was set to minimise the CPB pulse duration. As discussed in chapter 6, it was found that this left the driver duration de-optimised. A single-shot autocorrelator measured the driver pulse length at 90 fs and the CPB pulse length at 60 fs. In this configuration, all observed harmonic spectral lines were seen to split into two components: a blueshifted line which varied significantly from shot to shot, and a more stable line at the expected $\lambda_{\text{driver}}/q$ wavelength. Some weak extinction and enhancement was observed, as shown in figure 9.23, but the strength of the effect varied significantly from one timing scan to the next. The extinction or enhancement tended to affect the red and blue components of each harmonic line inconsistently, sometimes enhancing one while extinguishing the other, sometimes enhancing both together. The CPB had no visible effect unless its energy was set to the maximum 19 mJ.

The compressor gratings were then moved to optimise the driver rather than the CPB, and the timing scans were seen to change significantly. The harmonic lines now remained un-split except at high driver energies. Very reproducible extinction was also observed, and even very low CPB energies could produce an unmistakable effect. No enhancement was ever seen in this configuration, however.

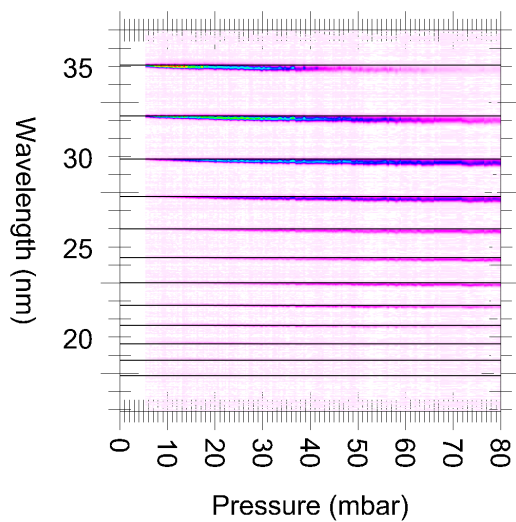
Finally, the original GVD compensator consisting of 160.1 mm of BK7 glass was replaced with a 40.5 mm piece of SF10, and the compressor re-optimised. This new GVD compensator allowed the driver and CPB pulse lengths to be minimised simultaneously. Following this change, the enhancement adjacent to the extinction was seen on every timing scan.

It is uncertain why the experiment was so sensitive to pulse compression, and more work needs to be done to explain the above observations. It is interesting that the CPB was much better able to suppress harmonic generation when its sub-pulse duration was lengthened from 60 to 90 fs; one might expect instead that the reduction in intensity would make it less effective at harmonic extinction.

9.2.10 Peak broadening and splitting

In order to improve the harmonic enhancement, it would be very useful to obtain better knowledge of the intensity and ionisation in the area of the focus. An examination of the broadening

(a) driver = 8 mJ



(b) driver = 17 mJ

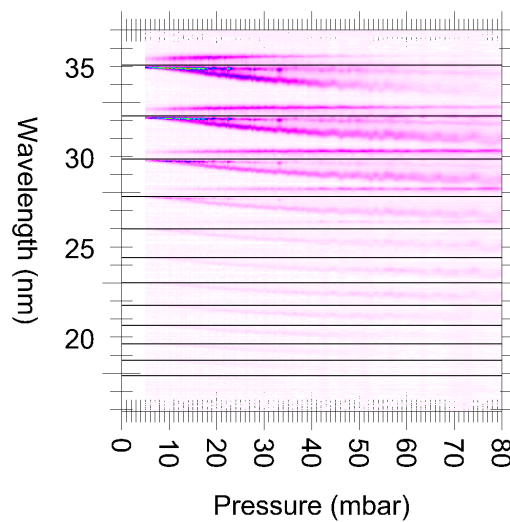


FIGURE 9.24: Pressure scans offer clues as to the conditions within the harmonic-generating region. No CPB is used in this scan.

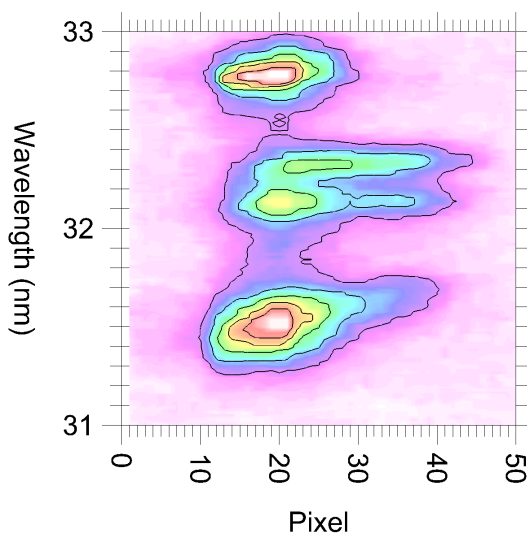


FIGURE 9.25: The spatial pattern on the spectrograph CCD differs for the components of the split harmonic peaks. The various components of $q=25$ are shown here.

and splitting of the harmonic lines may – with further analysis – provide some information to this end.

Scans of gas pressure provide insight into the mechanisms of line shifting and splitting, for ionisation blueshifting is proportional to pressure while nonadiabatic blueshifting is independent of it. Pressure scans at low and high driver energy (with no CPB) are shown in figure 9.24. At low driver energy, a small ionisation blueshifting is visible, while no nonadiabatic blueshift is apparent. At the maximum driver energy, each harmonic order is seen to split into roughly three spectral components:

1. a component with a large pressure-independent redshift and no ionisation blueshift,
2. a component with a small nonadiabatic blueshift and a moderate ionisation blueshift,
3. a component with a similar nonadiabatic blueshift to (2) but with a larger ionisation blueshift.

As stated in section 6.4.3, there is some uncertainty in the spectrograph calibration. “Redshift” and “blueshift” should therefore only be taken as relative terms, shifts from the harmonic’s wavelength in the low-driver-energy limit. Additional splitting may occur, especially within component (2) as shown in figure 9.25. Several factors strongly support the notion that each component is made at successive longitudinal positions, (3) being closest to the spectrograph and (1) being furthest away. First, the ionisation blueshift will increase roughly in proportion to the length of gas that has been traversed. Secondly, figure 9.18 shows component (3) being extinguished at lower timing slide positions than component (1), meaning that (3) is produced closer to the spectrograph. Finally, compare the harmonic orders $q=23$ and $q=29$ at various pressures. For the highest pressures, components (2) and (3) are stronger in $q=23$, while component (1) is much stronger in $q=29$. At low pressures, however, all three components of $q=23$ exceed those of $q=29$. This trend is consistent with the $q=23$ radiation being absorbed (recall figure 9.10), with the absorption appearing more significant for component (1) than for (2) or (3).

Note that it is component (1) that was discussed in section 9.2.3 as possibly arising from a second phase-matched region. No reports were found in the literature regarding significant

redshifting of harmonic lines, as displayed in this component, under similar conditions¹. An interaction capable of redshifting would be non-adiabatic shifting from the trailing edge of the driver pulse.

The spatial patterns of the components differ, as shown in figure 9.25. Because of the focusing mirror in the spectrograph, and because the light is dispersed along the “wavelength” axis, the pattern shown on the figure is modified greatly from the spatial pattern of light before the spectrograph. Nonetheless, it is apparent that component (1) is focused better than (2), so the divergences of the components must differ. Indeed, theories of harmonic peak splitting predict differences in spatial pattern for the different components [26].

One confusing observation regarding harmonic line splitting is the dependence on driver pulse compression. As noted earlier, line splitting was more pronounced with the de-optimised driver (chirped to 90 fs). Compared with the optimally compressed 60 fs pulse used in most of the Oxford experiments, this longer 90 fs pulse should have produced less ionisation and less nonadiabatic shifting (since the pulse energy was the same.) It may be that the driver’s chirp (and not just its duration) play a role the mechanism of line splitting, perhaps by affecting the phase matching conditions through the single-atom phase.

Though the patterns of harmonic line shifting and splitting thus provide some tantalising hints at the conditions of the focal region, many aspects are not well understood. Evidence is strong that at the highest driver energies, harmonics are generated in two or three separated locations. By understanding why these locations are separated, it may be possible to get a more reliable estimate of the ionisation fraction and intensity near the focus.

9.2.11 Trains of distinct pulses

Finally, CPBs of multiple distinct pulses were used in timing scans on several occasions, in the hope that some enhancement effect would be seen. Beyond the modest effect already described and examined in section 9.2.5, no additional enhancement was ever observed. Figure 9.26 shows a typical result. For this scan, the fourth of the seven crystals was deactivated, resulting

¹Brandi *et al* report redshifting in high harmonics of a 300 ps pulse[104]. However, the mechanism suggested – flow of electrons from the focal region – cannot account for redshifting of harmonics in the Oxford experiment where the pulse length is many times shorter.

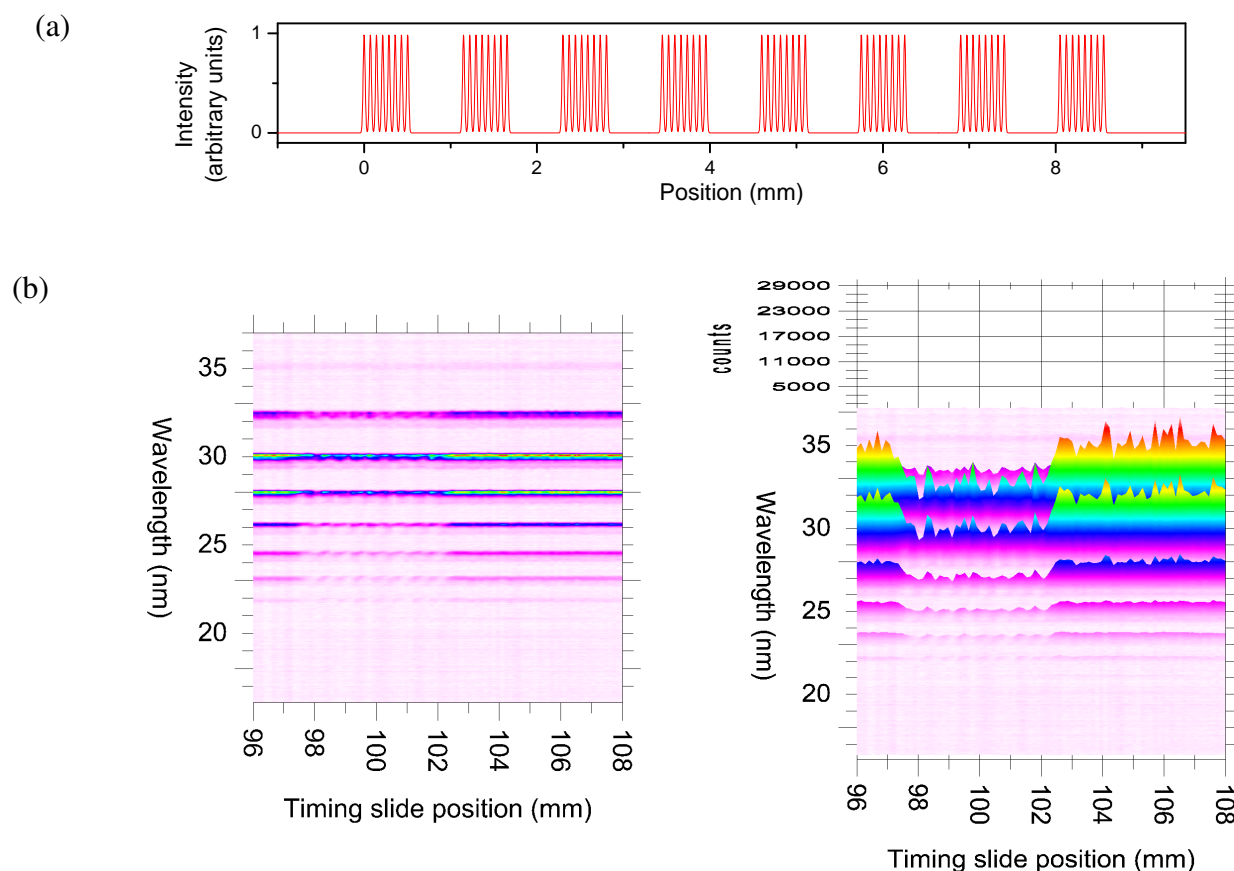


FIGURE 9.26: An attempt at QPM. (a) illustrates the train of pulses used in the CPB, as calculated assuming a 90 fs FWHMI for each sub-pulse. The results in (b) show no evidence of any enhancement.

in a CPB consisting of eight bursts of eight pulses. Nothing more than suppression of the signal was seen to occur.

9.2.12 Summary of findings

- In capillaries, line emission from the CPB striking the glass was very bright. Driver energy transmission through the capillaries was low, $\leq 3\%$, likely due to debris in the capillary bore left from machining of the gas entry holes.
- Extinction of harmonics was observed in a 3 mm gas cell. For some settings of the driver and CPB pulse compression, this extinction was extremely reproducible. For other very similar settings, it was only rarely observed.
- The required CPB energy for extinction in perpendicular polarisation scheme closely

matches the prediction of equation 5.14. For the parallel polarisation scheme, much more energy is needed than intensity-dependent phase would suggest (equation 5.7). The parallel polarisation data accord much better with the prediction for direct phase modulation (equation 5.5). The discrepancy may indicate that harmonic phase is less sensitive to driving intensity than previously thought.

- Reproducible enhancement of harmonics by up to a factor of 2 was observed. By analysing the dependence of harmonic enhancement and extinction with timing slide position, it is inferred that harmonics are generated over a length of ~ 0.6 mm, and at a time when the quasi phase matching period (double the dephasing length) is ~ 0.9 mm.
- The rate of ionisation-blueshifting of the driver can be measured from scans of the timing slide. If the low-intensity scenario is correct, the intensity deduced from this blueshifting is found to agree well with the intensity inferred from the harmonic cutoff law (equation 2.2.)
- With driver energies above ~ 9 mJ, harmonic peaks are seen to split into several frequency-shifted components, each produced in a different longitudinal interval. Notably, one component is redshifted (relative to the harmonic's wavelength in the limit that driver energy goes to 0.)

CHAPTER 10

Conclusions and Future Directions

Previous chapters have detailed the work performed at Astra and Oxford to produce trains of pulses and to use these trains to extinguish and enhance harmonic generation. The key experimental findings are now reviewed, and directions for future experimental work are discussed.

10.1 Summary of experiments

Cross-correlation measurements from both Astra and Oxford confirm that the N -crystal scheme for producing trains of pulses works very reliably. The most significant irregularity in the train is the varying intensity from pulse to pulse within the train. This variation could probably be significantly reduced with better angular positioning of the splitting crystals.

In both the Astra and Oxford experiments, the grazing-incidence waveguide presented several problems. High harmonic light was masked due to bright line radiation created by the CPB. Also, no effect of the CPB was ever seen with a waveguide target. Very long (~ 10 cm) capillaries were used at Oxford in an attempt to even out intensity fluctuations in the harmonic generating region. However, with these targets the fractional transmission was prohibitively low; it is likely that this is largely due to debris in the capillary bore left when gas entry holes were machined into the capillary.

No effect of the CPB was ever seen at Astra. However, several shots at Astra without the CPB are of interest. One series of consecutive shots show an increase in signal by > 40 as the

pressure was raised from 19 to 60 mbar. Another series of shots shows very high conversion efficiencies for the $q \approx 200$ harmonics in the water window. As these data were not appreciated until after the experiment was dismantled, it is not known whether the effects are robust. Standard phase matching seems unable to explain either effect. For the high- q shots, the possibility was considered that intensity modulations due to beating between capillary modes could have resulted in QPM. However, numerical results suggest otherwise. The intensity modulations in any realistic situation are seen to be too irregular for QPM, and they are highly sensitive to the pattern of light at the capillary entrance. Also, as discussed in section 8.6.1, intensity-dependent harmonic phase may adversely affect the intensity of the generated harmonics – unless $|d\phi/dI|$ is less than theory suggests. The spatial variation of Δk may also be problematic. These results have implications for the many reports of high harmonic generation in capillaries, for the extreme intensity fluctuations due to mode beating are likely to be present in any such experiment. Since many other groups have seen efficient harmonic generation in capillaries, perhaps $|d\phi/dI|$ is indeed smaller than expected.

In experiments with gas cell targets at Oxford, the CPB was found to have a robust ability to extinguish harmonic generation in precise locations. Extinction was found to be possible for a CPB polarised either parallel or perpendicular to the primary driving laser beam. Physical models developed in chapter 5 offer predictions for the energy required in the CPB for each scheme. Experiments show good agreement with these predictions, but only if intensity-dependent phase effects are ignored, further evidence that the phase of harmonic emission may be less sensitive to intensity than present theoretical models suggest. Less intensity is required in the CPB for the parallel polarisation method. Nonetheless, the perpendicular polarisation scheme may sometimes be preferable due to the ability to block light from re-entering the laser amplifier and thereby damage optics.

A factor of ~ 2 enhancement was observed at Oxford when the CPB was used. It is likely that greater enhancement was not seen because it was not possible to create multiple dephasing lengths within the region of harmonic generation. For unknown reasons, enhancement and extinction appeared to be extremely sensitive to temporal compression of the driver and CPB pulses.

The use of a CPB was also found to be a tool of potentially great diagnostic utility. By using a CPB while scanning the timing delay, beam energy, pressure, or gas cell location, information can be obtained about the conditions in the region of the laser focus. Several techniques were developed in chapter 9 for inferring quantities such as the ionisation fraction and dephasing length from the data.

It was found that for sufficient driver energy, the harmonics split into several distinct spectral peaks. By scanning the delay of the CPB, it was concluded that each component was generated in a different longitudinal interval near the focus.

10.2 Future directions

10.2.1 QPM by selective capillary mode excitation

In analysis of the Astra high- q enhancement (section 8.6.1), the intensity modulations produced by capillary mode beating would likely have been too irregular to produce QPM. However, the input light in that situation was not specifically tailored to selectively excite two modes. Would the intensity pattern be more regular if the focus were shaped to do so, perhaps by superimposing beams focused by two different f -numbers? Figure 10.1 shows the beat pattern for two superimposed Gaussians with sizes chosen to optimally excite the first and seventh radial modes. No regularity is apparent. As figure 3.2 shows, although the lowest-order mode can be excited with good selectivity by a Gaussian focus, it is very difficult to do the same for the higher order modes. If this scheme were to be attempted, then, adaptive optics would almost certainly be necessary to shape the focus with sufficient precision. Even if perfect coupling into two modes could be achieved, the scheme still has the two potential problems discussed earlier: intensity-dependent atomic phase, and spatially varying Δk .

Nevertheless, as discussed in chapter 8, the intensity beating patterns warrant further study. It may turn out that significant harmonic wave growth may still be possible despite the irregular phases and locations of the harmonic-emitting regions.

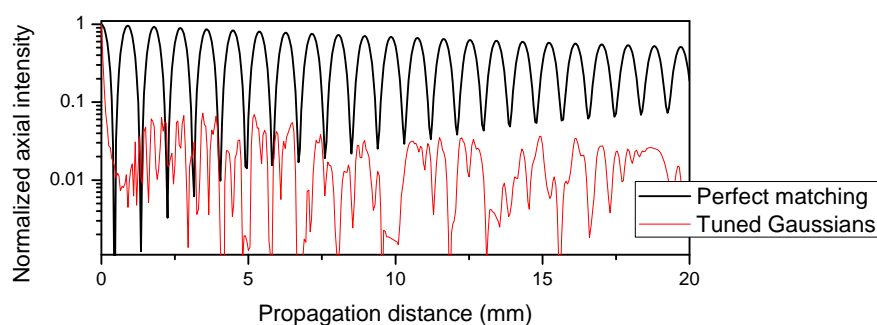


FIGURE 10.1: QPM by selective capillary mode excitation. Thick line: If modes $PIP_{0,1}$ and $PIP_{0,7}$ are excited in the ratio $J_1(u_{0,1}) : J_1(u_{0,7})$, clean beating results. The pattern decays because the modes are lossy. Thin line: Calculation for a more realistic focus consisting of two superimposed Gaussian spots. The radius of one is chosen to optimally excite $PIP_{0,1}$ ($w_0/a = 0.645$), and the radius of the other to optimally excite $PIP_{0,7}$ ($w_0/a = 0.0667$). The energy ratio (1.01:1) is also chosen so that $A_1 = A_7$, maximising beating between the two modes. Despite the optimisations, the axial intensity pattern is still too irregular for QPM.

10.2.2 Waveguide improvements

In order to extend QPM over more than a millimetre, the use of waveguide targets will be unavoidable. Therefore, solutions must be found to the problems described in this thesis: line emission from the CPB and low overall transmission. For grazing-incidence waveguides, it is likely that transmission would be improved if no gas holes are machined into the capillary. To supply gas to such an unmachined capillary, the capillary could be placed inside a differentially pumped gas cell that was just long enough to surround the waveguide.

Several techniques could be explored for reducing CPB line emission. Better quality calcite splitting crystals will almost certainly reduce the problem by improving the focus. A gated spectrograph CCD would be able to separate out the line emission (\gg picosecond duration) from the harmonic light (\ll 100 fs harmonic duration). A tapered capillary entrance may also reduce the problem. Finally, adaptive optics could be used to minimise CPB light falling outside the radius of the capillary bore.

Use of gradient-index plasma waveguides may also be considered. In such waveguides the CPB will not create line emission, because solid walls are further from the region of high intensity. However, XUV radiation will be emitted by the plasma which constitutes the waveguide. The high free electron density within plasma waveguides will result in very different phase

matching conditions. It is likely that the dephasing length will be $\ll 1$ mm, in which case there should be no problem to obtain $L_{\text{QPM}} \ll L_g$. Large enhancement factors may therefore be possible.

10.2.3 Other issues

In figure 9.13, the energy experimentally required in the CPB for extinction was found to closely match the analytical predictions of chapter 5. However, this comparison has only been attempted for one set of conditions (CPB burst length, gas pressure, driver pulse duration, etc.) It would be useful to repeat the experiments in other conditions to see if the theoretical match remains as good. From the experience at Oxford (section 9.2.9), the duration and possibly the chirp of the pulses may have strong effects on the effectiveness of harmonic extinction. An effort should be made to understand this sensitivity theoretically.

It may be interesting to record the spatial pattern of the XUV light on a CCD, without the focusing mirror and grating. By scanning the timing delay, the CPB could then be used to selectively extinguish the red or blue components of all split harmonics. Presumably the harmonics would be more divergent for one component than for the other, as surmised in section 9.2.10.

From figure 9.20 it appears that the enhancement effect observed at Oxford appeared only at the highest accessible pressures. It would be interesting to extend the observations to still higher pressures. It is plausible that QPM effects will grow stronger at higher pressures due to a decrease in the dephasing length. Higher pressures could be attainable by modifying the gas supply system. Alternatively, by improving the beam quality and using thicker gas cell wall materials, the gas cell hole size could be reduced.

Better theoretical methods could be developed to infer L_{QPM} and L_g from timing scans. The 1D models used in section 9.2.5 for this purpose left out details which are sure to be important, such as intensity-dependent phase and other spatial variation of Δk .

In general, further analysis could be done to build a more solid and consistent picture of the parameters near the laser focus. With such large uncertainty as to the intensity and ionisation fraction in this region, it is hard at present to know which are the critical parameters to vary to

increase the QPM enhancement.

In conclusion, several steps forward have been taken towards the goal of quasi phase matching for high-order harmonic generation. A counter-propagating beam seems capable of extinguishing harmonic generation in small controlled locations. Precisely controlled trains of pulses can be produced. With further work, it should be possible to exploit these techniques to achieve QPM, increasing the XUV brightness available from a table-top source.

Bibliography

- [1] Attwood, D. *Soft X-Rays and Extreme Ultraviolet Radiation: Principles and Applications*. Cambridge University Press, Cambridge, England (1999).
- [2] Elton, R. C. *X-Ray Lasers*. Academic Press, Inc, London (1990).
- [3] Reintjes, J. F. Coherent ultraviolet and vacuum ultraviolet sources. In M. Bass and M. L. Stitch, eds., *Laser Handbook*. North-Holland, New York (1985).
- [4] O'Shea, P. G. and H. P. Freund. Free-electron lasers: Status and applications. *Science*, **292**, 1853 (2001).
- [5] Plönjes, E. *et al.* Taking free-electron lasers into the x-ray regime. *Phys. World*, **16**, 7 (2003).
- [6] Daido, H. Review of soft x-ray laser researches and developments. *Rep. Prog. Phys.*, **65**, 1513 (2002).
- [7] Rocca, J. J. Table-top soft x-ray lasers. *Rev. Sci. Instr.*, **70**, 3799 (1999).
- [8] Gibson, E. A. *et al.* Coherent soft x-ray generation in the water window with quasi-phase matching. *Science*, **302**, 95 (2003).
- [9] L'Huillier, A. *et al.* Applications of high-order harmonics. *Europ. Phys. J. D*, **26**, 91 (2003).
- [10] Peatross, J. and D. D. Meyerhofer. Intensity-dependent atomic-phase effects in high-order harmonic-generation. *Phys. Rev. A*, **52**, 3976 (1995).
- [11] Corkum, P. B. Plasma perspective on strong-field multiphoton ionization. *Phys. Rev. Lett.*, **71**, 1994 (1993).
- [12] Kulander, K. C. *et al.* in super-intense laser-atom physics. *NATO Advanced Science Institutes Series*, **316**, 95 (1993).
- [13] Kapteyn, H. C. Coherent euv radiation: High-harmonic generation (Accessed 2006). <http://www.coe.berkeley.edu/AST/sxreuv/2004/HHG.pdf>.
- [14] Krause, J. L. *et al.* High-order harmonic generation from atoms and ions in the high intensity regime. *Phys. Rev. Lett.*, **68**, 3535 (1992).
- [15] M. Landreman. *Quasi phase matching techniques for high harmonic generation*. Master's thesis, Oxford University (2004). First year report.

- [16] Shin, H. J. *et al.* Nonadiabatic blueshift of high-order harmonics from Ar and Ne atoms in an intense femtosecond laser field. *Phys. Rev. A*, **63**, 053407 (2001).
- [17] Lappas, D. G. *et al.* Two-electron effects in harmonic generation and ionization from a model He atom. *J. Phys. B: At. Mol. Opt. Phys.*, **29**, L619 (1996).
- [18] Watson, J. B. *The Theory of Atoms Interacting with Intense Laser Fields*. Ph.D. thesis, Oxford University (1996).
- [19] Burnett, K. *et al.* Calculation of the background emitted during high-harmonic generation. *Phys. Rev. A*, **45**, 3347 (1992).
- [20] Prager, J. *et al.* High-order regime of harmonic generation with two active electrons. *Phys. Rev. A*, **64**, 045402 (2001).
- [21] Parker, J. *et al.* Intense-field multiphoton ionization of a two-electron atom. *J. Phys. B: At. Mol. Opt. Phys.*, **29**, L33 (1996).
- [22] L'Huillier, A. *et al.* Calculations of high-order harmonic-generation processes in xenon at 1064 nm. *Phys. Rev. A*, **46**, 2778 (1992).
- [23] Lewenstein, M. *et al.* Theory of high-harmonic generation by low-frequency laser fields. *Phys. Rev. A*, **49**, 2117 (1994).
- [24] Becker, W. *et al.* Modelling harmonic generation by a zero-range potential. *Phys. Rev. A*, **50**, 1540 (1994).
- [25] Peatross, J. *et al.* Intensity-dependent phase-matching effects in harmonic-generation. *J. Opt. Soc. Am. B*, **12**, 863 (1995).
- [26] Salieres, P. Coherence control of high-order harmonics. *Phys. Rev. Lett.*, **74**, 3776 (1995).
- [27] Balcou, P. Generalized phase-matching conditions for high harmonics: The role of field-gradient forces. *Phys. Rev. A*, **55**, 3204 (1997).
- [28] Gibson, E. A. *Quasi-phase matching of soft x-ray light from high-order harmonic generation using waveguide structures*. Ph.D. thesis, The University of Colorado (2004).
- [29] Lewenstein, M. *et al.* Phase of the atomic polarization in high-order harmonic generation. *Phys. Rev. A*, **52**, 4747 (1995).
- [30] Macklin, J. J. *et al.* High-order harmonic generation using intense femtosecond pulses. *Phys. Rev. Lett.*, **70**, 766 (1993).
- [31] Ammosov, M. V. *et al.* Tunnel ionization of complex atoms and of atomic ions in an alternative electromagnetic field. *Soviet Phys. JETP*, **64**, 1191 (1986).
- [32] Butler, A. *Short-wavelength lasers driven in capillary-discharge plasma waveguides*. Ph.D. thesis, Oxford University (2003).
- [33] Rae, S. C. *Short-Pulse Laser-Plasma Interactions*. Ph.D. thesis, Oxford University (1991).
- [34] Spence, D. J. *Plasma waveguides for high-intensity laser pulses*. Ph.D. thesis, Oxford University (2001).

- [35] Rae, S. C. Ionization-induced defocusing of intense laser pulses in high-pressure gases. *Opt. Comm.*, **97**, 25 (1993).
- [36] Altucci, C. *et al.* Tunable soft-x-ray radiation by high-order harmonic generation. *Phys. Rev. A*, **61**, 021801 (1999).
- [37] Rae, S. C. *et al.* Generation and propagation of high-order harmonics in a rapidly ionizing medium. *Phys. Rev. A*, **51**, 3438 (1994).
- [38] Watson, J. B. *et al.* Pulse shape effects and blueshifting in the single-atom harmonic generation from neutral species and ions. *Phys. Rev. A*, **51**, 1458 (1995).
- [39] Kan, C. *et al.* Spectral and temporal structure in high harmonic emission from ionizing atomic gasses. *Phys. Rev. A*, **52**, R4336 (1995).
- [40] Shin, H. J. *et al.* Generation of nonadiabatic blueshift of high harmonics in an intense femtosecond laser field. *Phys. Rev. Lett.*, **83**, 2544 (1999).
- [41] Kim, J.-H. *et al.* Wigner time-frequency distribution of high-order harmonics. *Phys. Rev. A*, **63**, 063403 (2001).
- [42] Kim, J.-H. and C. H. Nam. Plasma-induced frequency chirp of intense femtosecond lasers and its role in shaping high-order harmonic spectral lines. *Phys. Rev. A*, **65**, 033801 (2002).
- [43] Zhong, F. *et al.* Spectral splitting of high-order harmonic emissions from ionizing gases. *Phys. Rev. A*, **65**, 033808 (2002).
- [44] Froud, C. A. *et al.* Soft x-ray wavelength shift induced by ionization effects in a capillary. *Opt. Lett.*, **31**, 374 (2006).
- [45] Priori, E. *et al.* Nonadiabatic three-dimensional model of high-order harmonic generation in the few-optical-cycle regime. *Phys. Rev. A*, **61**, 063801 (2000).
- [46] Butler, A. *et al.* Guiding of high-intensity laser pulses with a hydrogen-filled capillary discharge waveguide. *Phys. Rev. Lett.*, **89**, 185003 (2002).
- [47] Gaudiosi, D. M. *et al.* High-order harmonic generation from ions in a capillary discharge. *Phys. Rev. Lett.*, **96**, 203001 (2006).
- [48] Okamoto, K. *Fundamentals of Optical Waveguides*. Academic Press, San Diego (2000).
- [49] Marcatili, E. A. J. and R. A. Schmelzter. Hollow metallic and dielectric waveguides for long distance optical transmission and lasers. *Bell Syst. Tech. J.*, **43**, 1783 (1964).
- [50] Cros, B. *et al.* Eigenmodes for capillary tubes with dielectric walls and ultraintense laser pulse guiding. *Phys. Rev. E*, **65**, 026405 (2002).
- [51] Jackel, S. *et al.* Channeling of terawatt laser pulses by use of hollow waveguides. *Opt. Lett.*, **20**, 1086 (1995).
- [52] Borghesi, M. *et al.* Guiding of a 10-TW picosecond laser pulse through hollow capillary tubes. *Phys. Rev. E*, **57**, R4899 (1998).

- [53] Dorchies, F. *et al.* Monomode guiding of 10^{16} W/cm² laser pulses over 100 Rayleigh lengths in hollow capillary dielectric tubes. *Phys. Rev. Lett.*, **82**, 4655 (1999).
- [54] Courtois, C. *et al.* Propagation of intense ultrashort laser pulses in a plasma filled capillary tube: simulations and experiments. *Phys. Plasmas*, **8**, 3445 (2001).
- [55] Leonard, P. J. Refractive indices, Verdet constants, and polarizabilities of the inert gases. *Atom. Data. Nucl. Data. Tables*, **14**, 21 (1974).
- [56] Center for x-ray optics: X-ray interactions with matter. (Accessed 2005). http://www-cxro.lbl.gov/optical_constants/.
- [57] Durfee III, C. G. *et al.* Phase matching of high-order harmonics in hollow waveguides. *Phys. Rev. Lett.*, **83**, 2187 (1999).
- [58] Balcou, P. and A. L'Huillier. Phase-matching effects in strong-field harmonic generation. *Phys. Rev. A*, **47**, 1447 (1993).
- [59] Gavrilla, M., ed. *Atoms in Intense Laser Fields*. Academic Press Limited, London (1992).
- [60] L'Huillier, A. and P. Balcou. High-order harmonic generation in rare gases with a 1-ps 1053-nm laser. *Phys. Rev. Lett.*, **70**, 774 (1993).
- [61] Ditmire, T. *et al.* Energy-yield and conversion-efficiency measurements of high-order harmonic radiation. *Phys. Rev. A*, **51**, R902 (1995).
- [62] Schnürer, M. *et al.* Absorption-limited generation of coherent ultrashort soft-x-ray pulses. *Phys. Rev. Lett.*, **83**, 722 (1999).
- [63] Mahon, R. *et al.* Third-harmonic generation in argon, krypton, and xenon: Bandwidth limitations in the vicinity of Lyman- α . *IEEE J. Quant. Electron.*, **14**, 444 (1979).
- [64] Kung, A. J. *et al.* Generation of 1182-Å Radiation in Phase-Matched Mixtures of Inert Gases. *Appl. Phys. Lett.*, **22**, 301 (1973).
- [65] Rundquist, A. *et al.* Phase-matched generation of coherent soft x-rays. *Science*, **280**, 1412 (1998).
- [66] Bartels, R. A. *et al.* Generation of spatially coherent light at extreme ultraviolet wavelengths. *Science*, **297**, 376 (2002).
- [67] Libertun, A. R. *et al.* Design of fully spatially coherent extreme-ultraviolet light sources. *Appl. Phys. Lett.*, **84**, 3903 (2004).
- [68] Milchberg, H. M. *et al.* High-order frequency conversion in the plasma waveguide. *Phys. Rev. Lett.*, **75**, 2494 (1995).
- [69] Wang, Y. *et al.* Spectral splitting in high-order harmonic generation. *Phys. Rev. A*, **62**, 063806 (2000).
- [70] Zhong, F. *et al.* The effect of ionization of gases on the high harmonic splitting. *Phys. Lett. A*, **278**, 35 (2000).
- [71] Sekikawa, T. *et al.* Femtosecond extreme-ultraviolet quasi-continuum generation by an intense femtosecond Ti:sapphire laser. *J. Opt. Soc. Am. B*, **15**, 1406 (1998).

- [72] Armstrong, J. A. *et al.* Interactions between light waves in a nonlinear dielectric. *Phys. Rev.*, **127**, 1918 (1962).
- [73] Franken, P. A. *et al.* Generation of optical harmonics. *Phys. Rev. Lett.*, **7**, 118 (1961).
- [74] Franken, P. A. and J. F. Ward. Optical harmonics and nonlinear phenomena. *Rev. Mod. Phys.*, **35**, 23 (1963).
- [75] Feisst, A. and P. Koidl. Current induced periodic ferroelectric domain structures in LiNbO₃ applied for efficient nonlinear optical frequency mixing. *Appl. Phys. Lett.*, **47**, 1125 (1985).
- [76] Zhu, Y. Y. *et al.* Second harmonic generation in periodically domain-inverted Sr_{0.6}Ba_{0.4}Nb₂O₆ crystal plate. *Appl. Phys. Lett.*, **70**, 1793 (1997).
- [77] Jundt, D. H. *et al.* Periodically poled LiNbO₃ for high-efficiency second-harmonic generation. *Appl. Phys. Lett.*, **59**, 2659 (1991).
- [78] Miller, G. D. *et al.* 42%-efficient single-pass cw second-harmonic generation in periodically poled lithium niobate. *Opt. Lett.*, **22**, 1834 (1997).
- [79] Serkland, D. K. *et al.* Amplitude squeezing by means of quasi-phase-matched second-harmonic generation in a lithium niobate waveguide. *Opt. Lett.*, **22**, 1497 (1997).
- [80] Chou, M. H. *et al.* Multiple-channel wavelength conversion by use of engineered quasi-phase-matching structures in LiNbO₃ waveguides. *Opt. Lett.*, **24**, 1157 (1999).
- [81] Zhu, S. *et al.* Quasi-phase-matched third-harmonic generation in a quasi-periodic optical superlattice. *Science*, **278**, 843 (1997).
- [82] Kazansky, P. G. *et al.* Blue-light generation by quasi-phase-matched frequency doubling in thermally poled optical fibers. *Opt. Lett.*, **20**, 843 (1995).
- [83] Lange, H. R. *et al.* High-order harmonic generation and quasiphase matching in xenon using self-guided femtosecond pulses. *Phys. Rev. Lett.*, **81**, 1611 (1998).
- [84] van der Poel, C. J. *et al.* Efficient type I second-harmonic generation in periodically segmented KTiOPO₄ waveguides. *Appl. Phys. Lett.*, **57**, 2074 (1990).
- [85] Paul, A. *et al.* Quasi-phase-matched generation of coherent extreme-ultraviolet light. *Nature*, **421**, 51 (2003).
- [86] Shkolnikov, P. L. *et al.* Optimal quasi-phase matching for high-order harmonic generation in gases and plasmas. *Phys. Rev. A*, **50**, R4461 (1994).
- [87] Christov, I. P. *et al.* Quasi-phase matching of high-harmonics and attosecond pulses in modulated waveguides. *Opt. Expr.*, **7**, 362 (2000).
- [88] Voronov, S. L. *et al.* Control of laser high-harmonic generation with counterpropagating light. *Phys. Rev. Lett.*, **87**, 133902 (2001).
- [89] Peatross, J. *et al.* Selective zoning of high-harmonic generation using counter-propagating light. *Opt. Expr.*, **1**, 114 (1997).

- [90] Prokopovich, I. P. *et al.* Increasing the efficiency of high-harmonic generation using counterpropagating laser pulses. *Phys. Rev. A*, **65**, 053823 (2002).
- [91] Madsen, J. B. *et al.* High-order harmonic generation in crossed laser beams. *J. Opt. Soc. Am. B*, **20**, 166 (2003).
- [92] Peatross, J. *et al.* Phase matching of high-order harmonic generation in helium- and neon-filled gas cells. *J. Mod. Opt.*, **51**, 2675 (2004).
- [93] Sutherland, J. R. *et al.* High harmonic generation in a semi-infinite gas cell. *Opt. Expr.*, **12**, 4430 (2004).
- [94] Dietrich, P. *et al.* High-harmonic generation and correlated two-electron multiphoton ionization with elliptically polarized light. *Phys. Rev. A*, **50** (1994).
- [95] Milosevic, D. P. Cut-off law for high-harmonic generation by an elliptically polarized laser field. *J. Phys. B*, **33**, 2479 (2000).
- [96] Budil, K. S. *et al.* Influence of ellipticity on harmonic generation. *Phys. Rev. A*, **48**, R3437 (1993).
- [97] Liang, Y. *et al.* High-order harmonic generation in argon by elliptically polarized picosecond dye laser pulses. *J. Phys. B*, **27**, 269 (1994).
- [98] Burnett, N. H. *et al.* Ellipticity and polarization effects in harmonic generation in ionizing neon. *Phys. Rev. A*, **51** (1995).
- [99] Miyazaki, K. and H. Takada. High-order harmonic generation in the tunneling regime. *Phys. Rev. A*, **52**, 3007 (1995).
- [100] Kakehata, M. *et al.* Anomalous ellipticity dependence of high-order harmonic generation. *Phys. Rev. A*, **55** (1997).
- [101] Flettner, A. *et al.* Atomic and molecular high-harmonic generation: a comparison of ellipticity dependence based on the three-step model. *J. Mod. Opt.*, **50**, 529 (2003).
- [102] Lopez-Martens, R. *et al.* Time-resolved ellipticity gating of high-order harmonic emission. *Phys. Rev. A*, **69**, 053811 (2004).
- [103] Lee, K. C. *Generation of Optical Pulse Trains for Quasi Phase-Matching of High Harmonic Generation*. Master's thesis, Oxford University (2006). M. Phys. project report.
- [104] Brandi, F. *et al.* Spectral redshift in harmonics generation from plasma dynamics in the laser focus. *Phys. Rev. Lett.*, **96**, 123904 (2006).
- [105] Kazamiasa, S. *et al.* High order harmonic generation optimization with an apertured laser beam. *Europ. Phys. J. D*, **21**, 353 (2002).
- [106] Dromey, B. *et al.* High harmonic generation in the relativistic limit. *Nature Phys.*, **2**, 456 (2006).
- [107] Spielmann, C. *et al.* Generation of coherent x-rays in the water window using 5-femtosecond laser pulses. *Science*, **278**, 661 (1997).